OffshoreDC DC grids for integration of large scale wind power

Cutululis, Nicolaos Antonio; Zeni, Lorenzo; Endegnanew, Atsede Gualu ; Stamatiou, Georgios; El-Khatib, Walid Ziad; Helistö, Niina

Publication date:
2016

Document Version
Publisher's PDF, also known as Version of record

norden
Nordic Energy Research

DTU

OffshoreDC
DC grids for integration of large scale wind power

Department of Wind Energy
E Report 2016

CHALMERS

DTU Electrical Engineering
Department of Electrical Engineering

DONG energy

NTNU

VTT

DTU Wind Energy
Department of Wind Energy

Editor: Nicolaos A. Cutululis

Authors: Lorenzo Zeni, DONG Energy, Atsede Gualu Endegnanew, NTNU, Georgios Stamatiou, Chalmers, Walid Ziad El-Khatib, DTU, Niina Helistö, VTT

Project participants:

Project owner: Peter Hauge Madsen

Company/organisation: DTU Wind Energy

Contact person: Nicolaos A. Cutululis, niac@dtu.dk

R&D-partners:

1. *DTU Wind Energy* (Denmark). Principal participants: Nicolaos A. Cutululis, Poul Sørensen, Anca D. Hansen
2. *DTU Electrical Engineering* (Denmark), Principal participants: Walid Ziad El-Khatib, Joachim Holbøll
3. *NTNU* (Norway). Principal participants: Atsede Gualu Endegnanew, Vin Cent Tai
4. *Chalmers* (Sweden). Principal participants: Georgios Stamatiou, Massimo Bongiorno, Ola Carlson
5. *VTT* (Finland). Principal participants: Niina Helistö, Sanna Uski, Juha Kiviluoma
6. *Aalborg University* (Denmark). Principal participants: Remus Teodorescu

Industry partners:

1. DONG Energy (Denmark). Principal participants: Lorenzo Zeni and Bo Hesselbæk
2. ABB (Sweden). Principal participants: Liliana Arevalo, Lennart Harnefors
3. Energinet.dk, (Denmark). Principal participants: Torsten Lund
4. Vestas (Denmark). Principal participants: Philip Carne Kjær
5. Statnett (Norway) – associate partner, Principal participants: Tarjei Midtsund

June 2016.

Project no.:

TFI PK-int 02

Sponsorship:

Nordic Energy Research

DTU Wind Energy E-0124

Pages: 97

Tables: 22

References: 36

ISBN: 978-87-93278-86-8

Technical University of Denmark
Department of Wind Energy
Frederiksborgvej 399
Building 118
4000 Roskilde
Denmark

niac@dtu.dk
www.vindenergi.dtu.dk

Preface

The present report summarizes the main findings of the Nordic Energy Research project “DC grids for large scale integration of offshore wind power – OffshoreDC”. The project is been funded by Nordic Energy Research through the TFI programme and was active between 2011 and 2016.

The overall objective of the project was to drive the development of the VSC based HVDC technology for future large scale offshore grids, supporting a standardised and commercial development of the technology, and improving the opportunities for the technology to support power system integration of large scale offshore wind power. This was done by bringing together the key industry stakeholders and competent research organisations in the project.

The partners of the OffsoreDC project are:

ABB

Aalborg University

Chalmers University

DONG Energy

DTU Electrical Engineering

DTU Wind Energy (coordinator)

Energinet.dk

NTNU (Sintef)

Statnett

VTT

Roskilde, June 2016
Nicolaos A. Cutululis
Senior Researcher

Contents

Glossary

Symbol	Definition
AVR	Automatic voltage regulator
CPL	Constant power load
D-DVC	Direct voltage controller
EMC	Electromagnetic compatibility
EMT	Electromagnetic transients
ES	Excitation system
ESL	Equivalent series inductances
ESR	Equivalent series resistances
FD	Frequency dependent
HVDC	High voltage direct current
IGBT	Insulated-gate bipolar transistor
LCC	Line commutated converter
LR	Left right
MMC	Multi module converter
MTDC	Multi-terminal direct current
OWPP	Offshore wind power plant
PCC	Point of common coupling
PD-DVC	Power dependent direct voltage controller
PI	Proportional Integral
PLL	Phase locked loop
PWM	Pulse width modulation
RHP	Right half plane
RLC	Resistor Inductor Capacitor
SCR	Short circuit ratio
SISO	Single input single output
SMT	Similarity matrix transformation
SRF	Synchronous reference frame
TSO	Transmission system operator
VSC	Voltage source converter
WPP	Wind power plant
WT	Wind turbine

Summary

The OffshoreDC project is addressing several of the most important challenges regarding VSC-HVDC offshore transmission technology:

- Transients and interactions in VSC-HVDC systems
- Control and stability analysis of offshore wind power plants and HVDC grids
- Feasibility study of offshore grids in the Baltic Sea

The main results are briefly presented in this report. For the detailed results, the reader is advised to consult the extensive OffshoreDC publications listed in the Annex.

Transients and interactions in VSC-based HVDC systems

The dc-network dynamics of VSC-HVDC systems were thoroughly investigated in two-terminal connections and new perspectives were introduced to the control of VSC-MTDC grids.

Regarding the stability investigation, two-terminal VSC-HVDC system was modelled as a SISO feedback system, where the VSC-transfer function $F(s)$ and the dc-grid transfer function $G(s)$ were defined and derived. Two different methods were then utilized to assess the closed-loop stability of the complete system by observing the separate frequency domain behaviour of the $F(s)$ and $G(s)$. The *Passivity* analysis focused on the related passivity properties of the two transfer functions at critical frequencies. This tool showed satisfactory results as long as both transfer functions were stable. However, once the latter was not valid, the passivity approach could no longer be used. The *Net-damping criterion* approach did not have this complication and proved to be a superior tool in analyzing the stability of the system and deriving useful results, based on the individual net-damping of $F(s)$ and $G(s)$. It was also found that the absolute amount of net-damping in the system measured at the frequency where the Nyquist plot crosses the real axis closest to -1, is directly related to the existence of poorly-damped dominant poles and their damping factor. A net-damping approaching zero at that frequency indicates the existence of poorly-damped poles with constantly decreasing damping factor.

The analysis of the previous systems was also observed from an analytical-pole description. The *SMT* analytical method was developed and presented in conjunction with the already known *LR* method, which had nevertheless never been implemented in the analysis of power systems or control related processes. A benefit of the *SMT* focused on the fact that is not iterative, meaning that the form and complexity of the final analytical eigenvalue expressions is known from the beginning, in contrast to the iterative *LR* where each additional iteration theoretically improves the accuracy but dramatically worsens the compactness of the expressions. Both methods showed impressive results in approximating the actual values of the VSC-HVDC model, but the *SMT* showed a consistent increase in accuracy compared to the *LR*.

In the area of Multiterminal HVDC, focus was given on the development of droop-based controllers. In the beginning, a controller was proposed for use in cases where a VSC station required to maintain its designated power flow after unexpected contingencies in the grid, such as the loss of a station following a dc-side fault, while maintaining voltage-droop characteristics during transients in the grid. The concept was tested in a five-terminal MTDC, where the performance of the controller was favourably compared to that of a conventional PI-based power controller. A second droop-controller variation was proposed for use in MTDC grids where a droop-controlled station requires a very high droop constant, meaning that it should maintain its power flow almost constant under all grid conditions, but still provide direct-voltage support as a conventional droop-controlled station would during grid contingencies. The proposed controller was tested in a four-terminal MTDC and compared to the performance of conventional droop-controllers, with the same droop constants being used for the same stations in both scenarios. It was shown that following a rapid change of power and voltage setpoints, the two controllers had no difference in steady-state performance (as desired), but the proposed control provided a smooth power and direct-

voltage reaction from the stations that used it, compared to the conventional control that even exhibited poorly-damped oscillations.

Many properties of the MMC have been illustrated and explained. Theoretical evaluations and simulation results have been related to examine the similarity. It is desired that the simulation model mirrors the properties of a real life converter, to make the analysis valid also in that context. In order to study various dynamic behaviours of HVDC transmission systems, a dynamic simulation model is developed. Furthermore, since the transient behaviour was very important in this work, a high frequent model had to be developed for the main components. This includes wind turbine, collector network, transformers, VSCs, cables and other major components of the system. Nevertheless the main two components affecting the simulation time negatively (cables and converter) where modelled in a simplified manner which preserved their functionality and dynamic performance. The converter model was verified against a 5-level VSC-MMC laboratory construction. The MMC converter, together with its control and protection, was designed and constructed during this project.

The performance of HVDC transmission was analysed for multiple types of connections. The system was analysed for point-2-point MMC interconnector power transmission. Simulation showed how even with a low number of submodules the converter was able to continue operating with the loss of submodules.

Transients in HVDC connected WPPs was analysed and compared with HVAC. A method was proposed to minimize the inrush currents and damping resonances using the offshore converter. The importance of reactive power support in weak offshore grids was pointed out and a chopper was proposed to further protect the system. The related work supports the derivation of requirement specifications of components in a MTDC network by means of simulations and calculations. It demonstrated the ability to control complex multi-terminal HVDC topologies in case of severe power variations occurring in the DC grid. It contributes to a deeper understanding of the transient behaviour of the MTDC grid during a pole-to-ground fault on both the AC and DC sides and analyses the influencing parameters. The modelling and implementation of the network components in a MTDC network for the simulation of transient voltages and currents were described first, as well as the required methods for the transient simulations.

Control and stability analysis of offshore wind power plants and HVDC grids

The implementation of frequency and DC voltage control on OWPPs was described in this section related to (i) frequency control provision from a point-to-point HVDC connected OWPP and to (ii) DC voltage control from OWPPs connected to DC grids. In the former, the similar performance of communication-based and coordinated frequency control was demonstrated and OWPPs's limitations were highlighted. For the latter, the big challenges that will have to be overcome if a significant part of DC voltage control to HVDC grids is to be provided by OWPPs have been illustrated and solutions have been discussed.

Moreover, the work performed showed that by coordinating converter controllers at offshore wind farm and one ac grid, it is possible to maximize frequency support contribution of the offshore wind farm and avoid disturbance in other AC grids connected to the MTDC. However, the proposed method works when only one ac grid is getting frequency support and the remaining ac grid connected MTDC terminals are operating in dc droop or constant power control mode. If more than one ac grids are to receive frequency support through MTDC grid, then negative interactions occur when the proposed controller is used.
Finally, a laboratory demonstration of inertial response from HVDC connected wind farm was shown, giving further credibility to some of the results obtained with simulation software.

The small signal stability of a system with three multi-machine ac grids connected through an MTDC grid was analysed. It was shown that the dynamic behaviour of ac grids is not significantly affected with the introduction of dc grids to interconnect ac power systems. In addition, the work identified that synchronous generators in asynchronous grids linked via MTDC interact dynamically through the dc grid. The change in the level of these interactions was studied for different tuning, control mode and damped frequency cases. It was found that faster and slower converter control response lead to lower and higher interactions between the asynchronous ac grids,

respectively. This observation is in line with the expectations that a faster control of the power balance within the dc grid will make the connected ac systems more decoupled. The level of this dynamic interaction was studied with dc voltage droop and master-slave control modes implemented in the MTDC terminal converter. The results indicated that when dc voltage droop control is used the level of interaction between generators in asynchronous grid is low but similar in scale. On the other hand, when master-slave control mode is used, the interaction with generators located in grids behind constant power controlled terminal is much lower than generators located in the grid where the constant dc voltage controlled (master) terminal is found. The final analysis showed that the level of dynamic interaction between asynchronous grids is highest when the dominant electro-mechanical modes in the different ac grids have similar damped frequency of oscillations. Results of a time domain simulation of the study system for a fault in one of the ac grids support findings of the modal analysis. The study results show that there exists a dynamic coupling between ac grids across dc grids and that the level of interaction is influenced by the converter controller settings.

The contribution OWPPs can give to the enhancement of small-signal stability was analysed in [Zeni, 2015a] and the findings were summarised in the second part of this section. Guidelines to tune POD control parameters on static sources were generated in [Zeni, 2015a], after emphasising the need to account for ESs and AVRs in small-signal analysis. The implementation on HVDC-connected WPP was successfully tested on a dynamic simulation tool. Moreover, limiting factors for the delivery of this feature from WPPs were discussed. Finally, the experimental validation work performed at National Renewable Energy Laboratory in the US was summarised.

Feasibility study of offshore grids in the Baltic Sea

The focus in this feasibility study was in the possible offshore grid development paths in the Baltic Sea region. The main findings of the study are:

Costs: The results show that interconnections will decrease the total costs significantly in the Baltic Sea region compared to only two-terminal connections from offshore wind power plant clusters to shore. Building separate offshore interconnectors and wind power plant connections instead of a multi-terminal-like offshore grid based on two-terminal links may result in lower investment and operation costs. According to the results, multi-terminal and meshed offshore grid structures will have lower costs than structures based on separate offshore wind cluster connections and interconnectors provided that HVDC circuit breakers are available and their price is low enough. The threshold that was found out in the study for the circuit breaker cost is approximately one fourth of converter station cost.

Annual transmissions: In all the studied cases, the annual transmissions were generally from north to south and from east to west. This is a result from the assumed deficit of inexpensive generation infrastructure in Germany. The annual transmissions were also very large from northern Sweden to southern Sweden. However, the initial transmission capacities from northern to central Sweden appear to be large enough since the optimization model did not invest in new connections from the Gulf of Bothnia to central parts of the Baltic Sea in any of the cases.

Hourly transmissions: Hourly power flow analysis results showed similar patterns as the annual transmissions. Loop flows and overloadings were detected inside and between Sweden and Norway in the analysed generation and load snapshots. If the model had included more regions from Central Europe, very likely more loop flows would have been seen there as well.

1. Introduction

Offshore wind power development has increased dramatically in the last years, reaching a total of over 11 GW in 2015, Figure 1.

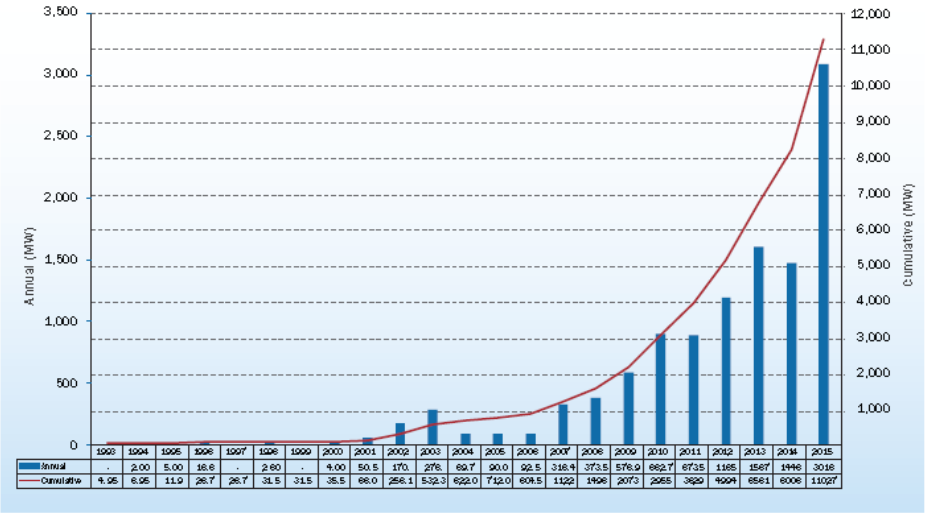

Figure 1 Offshore wind power in Europe, cumulative and annual installations MW [EWEA, 2016]

At the same time, offshore wind power plants are moving further from shore and into deeper waters. At the end of 2015, the average water depth of grid connected wind power plants was 27.1 m and the average distance to shore was 43.3 km. However, the average distance to shore is expected to grow significantly in the future, with some of the consented wind power plants being more than 100 km distance from shore (Figure 2).

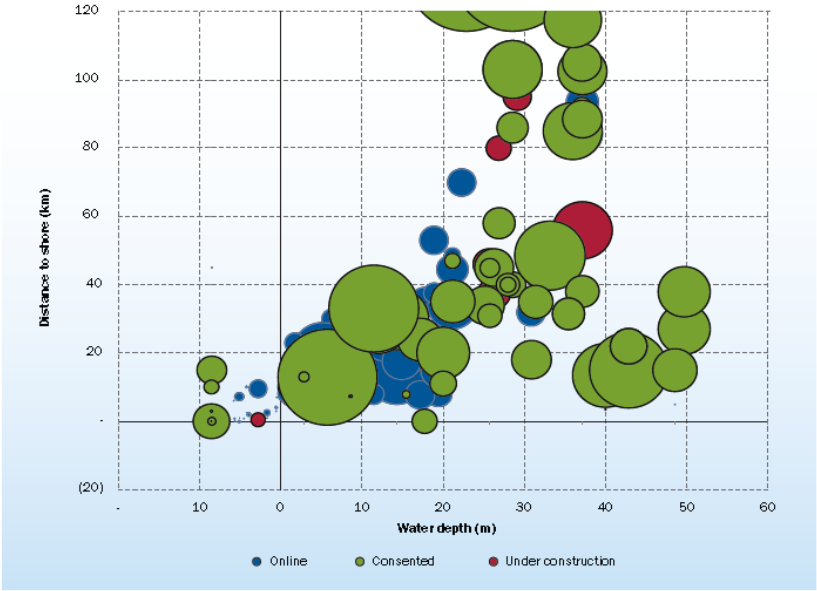

Figure 2 Average water depth and distance to shore of online, under construction and consented wind power plants at the end of 2015 [EWEA]

The long distance from shore is influencing the electrical transmission infrastructure. In general, it is considered that classical AC connections can be used for distances up to 70-100 km, while for distanced larger than that, VSC–HVDC is widely regarded as the preferred solution. This is clearly seen in Figure 3, where the German clusters with distances greater than 150 km are all connected with VSC-HVDC [Zeni, 2015].

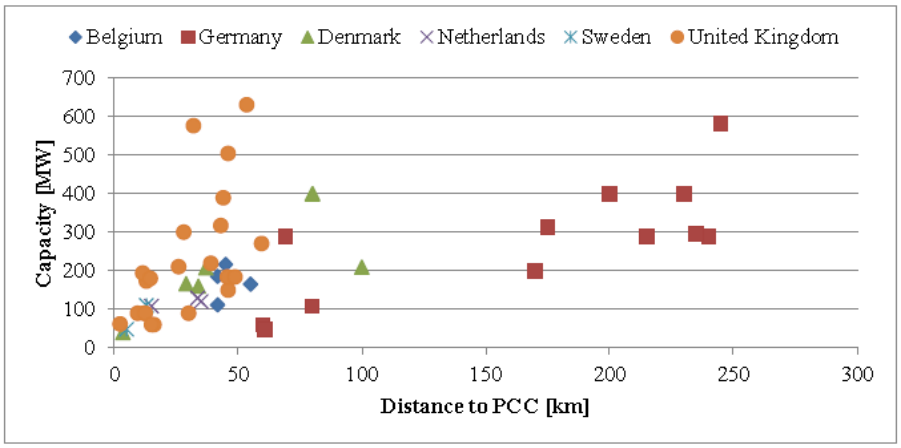

Figure 3 Overview of European offshore wind projects by distance to PCC and capacity [Zeni, 2015]

VSC-HVDC technology is very promising, with commercial applications since about the end of 90s [ABB, 2014]. Compared to the earlier LCC technology, VSC has a number of advantages that are very important for long distance applications: compactness, black-start capability, ability to connect to weak networks, independent control of active and reactive power, fast reversibility of active power flow, etc. All those advantages have made VSC-HVDC to be widely seen as the best solution for long distance transmission, i.e. interconnectors between different synchronous areas (or even embedded in the same AC power system) and for connecting offshore wind power. The limited experience with VSC-HVDC transmission technology, especially in offshore environment, means that the community is climbing up the learning curve, with a very important role played by the research community in exploring all the opportunities and limitations.

The OffshoreDC project is addressing several of the most important challenges regarding VSC-HVDC offshore transmission technology:

- Transients and interactions in VSC-HVDC systems
- Control and stability analysis of offshore wind power plants and HVDC grids
- Feasibility study of offshore grids in the Baltic Sea

2. Transients and interactions in VSC-based HVDC systems

The use of VSC-HVDC systems is considered to be a major step in facilitating long distance power transfer and integrating remotely located renewable energy sources to major consumption centres. A main objective of this chapter is to perform studies on the stability of VSC-HVDC systems and investigate the interaction between the control structures, passive components and operating points. The ultimate goal is to develop methodologies and tools that will allow the explanation and understanding of poorly-damped conditions that may appear in such systems. Furthermore, the potential of using VSC technology in large scale MTDC grids, requests a robust control structure with exceptional handling characteristics of the power-flow and direct-voltage management. This is an area to which the related work attempts to contribute accordingly.

2.1 Converter interactions in VSC-based HVDC systems

One of the problems that can generally be observed in dynamic systems is the potential occurrence of poorly-damped oscillations following disturbances. This is of great concern for HVDC applications, where the ratings and complexity level demand strict avoidance of such events. The introduction of VSC technology has undoubtedly offered great controllability to the applications used, but has also influenced their dynamic performance and therefore their ability to damp potentially hazardous oscillations.

2.1.1 Stability of two-terminal VSC-HVDC systems

In this section, the dynamics and the closed-loop stability of two-terminal VSC-HVDC systems are assessed. On the one hand, an analytical description of the systems' dominant poles is derived, giving the opportunity to establish direct relationships between a specific system parameter and the frequency/damping properties of the poles, to predict poorly-damped behaviour. Frequency domain approaches are also used to perform stability investigation. This proves beneficial for the assessment of highly detailed systems where the analytical approach cannot be applied.

2.1.1.1 Resonances in VSC-HVDC

The problem of dc-side resonances can also appear in VSC-HVDC links. A typical two-terminal VSC-HVDC system is depicted in Figure 4 where each of the transmission poles has been replaced with its equivalent π-section. A first observation is that the dc-link is effectively a closed RLC resonant-circuit. If the converter capacitors are considered equal, $C_{\mathrm{dc1}} = C_{\mathrm{dc2}} = C_{\mathrm{conv}}$, the resonant frequency of the circuit will be

$$\omega_{\mathrm{res}} = \frac{1}{\sqrt{L_{\mathrm{pole}}\left(C_{\mathrm{conv}} + \frac{C_{\mathrm{pole}}}{4}\right)}} \tag{2.1}$$

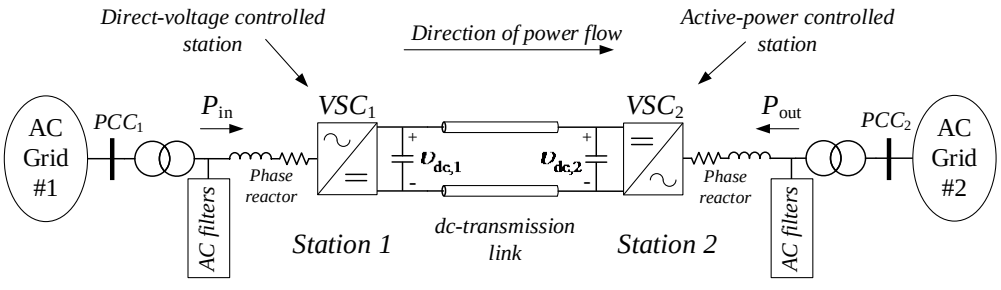

Figure 4 Two-terminal VSC-HVDC transmission link. The controlled power is the power entering the phase reactor with a positive direction towards the VSC station.

When power is imported from the rectifier-side and exported from the inverter-side, the transmission link is naturally unstable as was investigated. The rectifier station is operating in direct-voltage control mode with a certain controller speed, stabilizing the transmission link and bringing a power balance. The interaction between the dynamics of the direct-voltage controller and the dc-link leads to a closed-loop system whose properties are not always predictable. It was found that the system may have poorly-damped poles (most often those associated with the resonant frequency of the dc-link) or even become unstable. The contribution of the CPL small signal deterioration of the systems stability characteristics should also be taken into account.

In [Mura, 2010], the authors investigate the transient stability of a dc grid comprising of clusters of offshore wind-turbine converters connected through HVDC-cables to a large onshore VSC inverter. Using the traveling wave theory on long cables, it was demonstrated that choosing equal lengths for the cluster cables was a worst case scenario in terms of grid stability. A two-terminal VSC-HVDC connection between two weak ac grids is presented in [Zhang, 2007] using Power-Synchronization control on the converters, where it was also claimed that the resistance of the dc-link plays a destabilizing role. A poorly-damped resonance was demonstrated to exist and a notch filter was used in the control strategy to reduce the dc resonant peak. Investigation of the dynamic stability has also been performed in multiterminal VSC-HVDC connections as in [Rault, 2012], where the impact of the droop setting k_{droop} in the direct-voltage controller of the stations was assessed. It was found that high values of k_{droop} could turn a point-to-point droop controlled connection unstable.

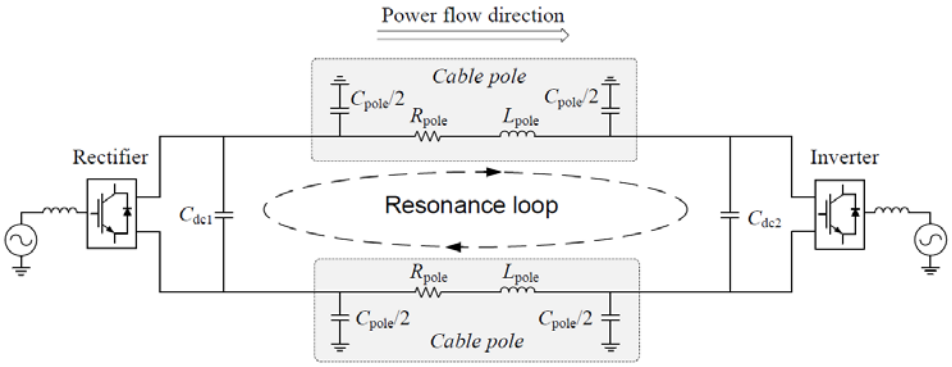

Figure 5 DC-link resonance loop in a two-terminal VSC-HVDC connection

2.1.1.2 Unstable conditions

For this scenario, the system of Figure 5 is used, with system properties defined in Table 1-The length of the overhead-line based (properties found in Table 2) dc-transmission link in the system of Figure 4 is set to 300km and a specific pattern of active-power reference is provided to the active-power controlled station, while the direct-current controller receives a constant reference u_{dc}^{*}=640kV. The sequence of events is as follows

- P_{out}^{*}=0 MW until t=5s.
- P_{out}^{*} is linearly ramped from 0 to -500MW until t=5.5s.
- P_{out}^{*} remains unchanged until t=6.5 s.
- P_{out}^{*} is linearly ramped from -500 to -900 MW until t=7s and then remains constant until t=8.5s.
- P_{out}^{*} is linearly ramped from -900 to -500 MW until t=9s and then remains constant until then end of the simulation

Table 1 Rated values of VSC-HVDC stations

P_{N}	VSC rated power	1000 MW
$\upsilon_{\mathrm{dc,N}}$	rated direct voltage	640 kV
$\upsilon_{\mathrm{s,N}}$	rated voltage at transformer's ac-grid side	400 kV
$\upsilon_{\mathrm{g,N}}$	rated voltage at transformer's converter side	320 kV
S_{N}	ac side rated power	1000 MVA
X_{l}	transformer leakage inductance	0.05 pu
L_{f}	phase reactor inductance	50.0 mH (0.153 pu)
R_{f}	phase reactor resistance	1.57 Ω ($0.1\times X_{\mathrm{f}}$)
C_{dc}	dc-side capacitor	20 μF
a_{d}	bandwidth of the closed-loop direct-voltage control	300 rad/s (0.96 pu)
a_{f}	bandwidth of the power-feedforward filter	300 rad/s (0.96 pu)
a_{cc}	bandwidth of the closed-loop current control	3000 rad/s (9.6 pu)
f_{s}	switching frequency	1500 Hz
f_{notch}	notch-filter frequency	1500 Hz
C_{filter}	ac-side filter capacitor	5 μF

Table 2 Physical properties for modelling dc-transmission lines

Type of dc-transmission line	r (Ω/km/pole)	l (mH/km/pole)	c (μF/km/pole)
Cable	0.0146	0.158	0.275
Overhead line	0.0178	1.415	0.0139

The response of the system can be observed in Figure 6. In the first 7 seconds of the simulation, the system manages to follow the active-power reference without any problems, with the direct-voltage controller performing seamlessly at all instances. However after t=7s and when the power reaches approximately 900MW, the system experiences an oscillation of 199.4Hz which constantly increases in magnitude as evidently observed in the P_{in} and υ_{dc1} responses. This oscillation quickly becomes unstable but the system integrity is sustained due to the existence of limiters in the control structures, limiting the input i_d^* at the current controllers of both VSC stations to 1.1pu in the examined scenario. As such, P_{in} never exceeds 1100MW in magnitude and the theoretically unstable oscillation is now contained in a bounded region. It should be noted that even during this event, the active power controller manages to impose the request P_{out}^* on its ac side. Only small signs of the oscillation can be traced on P_{out}. This is attributed to the fact that the corrected modulation wave of the PWM process is calculated and applied only at the switching events. For a higher switching frequency, the oscillation is much smaller until it disappears completely for non-switching converter models.

Once P_{out}^* is ramped to -500MW, the system gradually goes out of instability and becomes stable and fully operational again after t=9.4s. This demonstrates how the level of power transfer had a fundamental impact on the dynamic stability of the system. The instability exhibited in the example of this section will be further investigated in the following chapter.

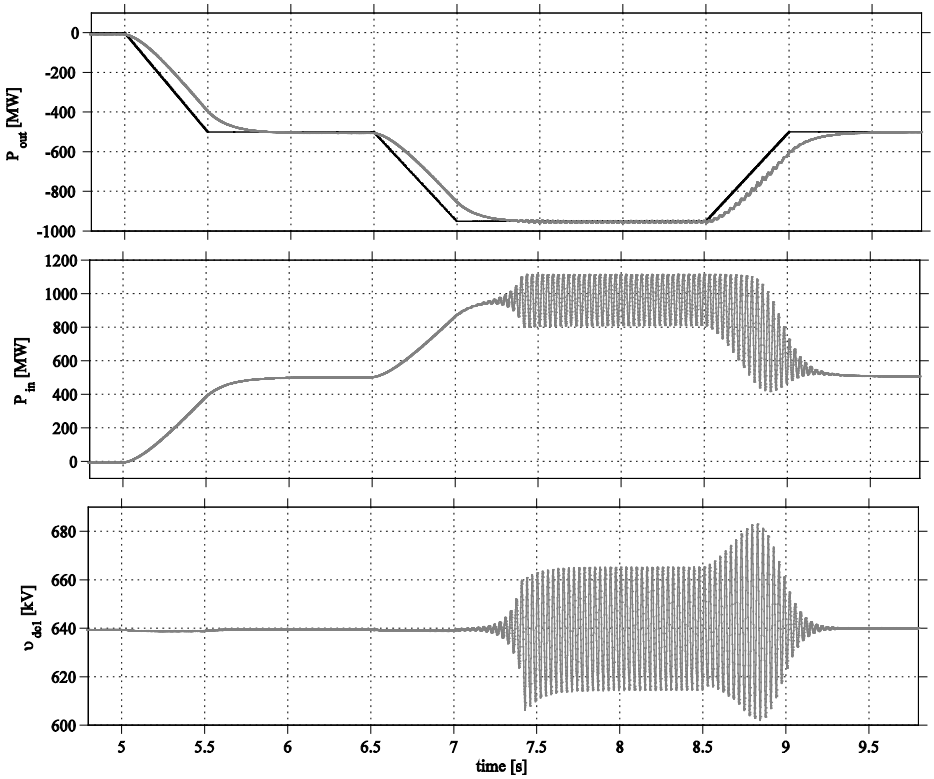

Figure 6 Power and voltage response of the system in instability conditions. Upper figure: $\mathbf{P_{out}^*}$ (black line) and $\mathbf{P_{out}}$ (gray line). Middle figure: $\mathbf{P_{in}}$. Lower figure: $\boldsymbol{\upsilon_{dc1}}$.

2.1.1.3 Passivity analysis of a two-terminal VSC-HVDC system

The length of a linear, continuous-time system described by a transfer function $R(s)$ is defined as *passive* if and only if, the following conditions apply at the same time [Willems, 1972]

- $R(s)$ is stable
- $\text{Re}\{R(j\omega)\}\rho 0, \ \forall\ \omega\rho 0$

From a complex-vector point of view, the latter is equivalent to the condition of $-\pi/2 \leq \arg\{R(j\omega)\} \leq \pi/2$, implying that the real part of the transfer function is non-negative. Additionally, if $R(s)$ is stable and $\text{Re}\{R(j\omega)\}>0, \forall\ \omega\rho 0$, the corresponding system is defined as *dissipative*.

The passivity concept can be expanded to closed-loop systems, as the Single Input Single Output (SISO) system in Figure 7 if both the open-loop transfer function $F(s)$ and the feedback transfer function $G(s)$ are passive, then the closed-loop transfer function of the complete system

$$R_c(s) = \frac{F(s)}{1+F(s)G(s)} \tag{2.2}$$

is stable and passive [Harnefors, 2008]. The opposite is however not true. If either $F(s)$, or $G(s)$, or both of them, are non-passive then $R_c(s)$ is not necessarily non-passive or unstable.

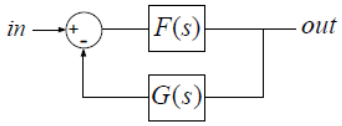

Figure 7 SISO system with negative feedback

The previous statements are very important from a control point of view. If a controlled process can be represented by the SISO form Figure 7, the passivity characteristic of the subsystems either $F(s)$ and $G(s)$ can either guarantee the stability of the closed loop, or provide a hint for instability and there is a need for further investigation using alternative tools, e.g. the Nyquist criterion, which can provide a definite answer.

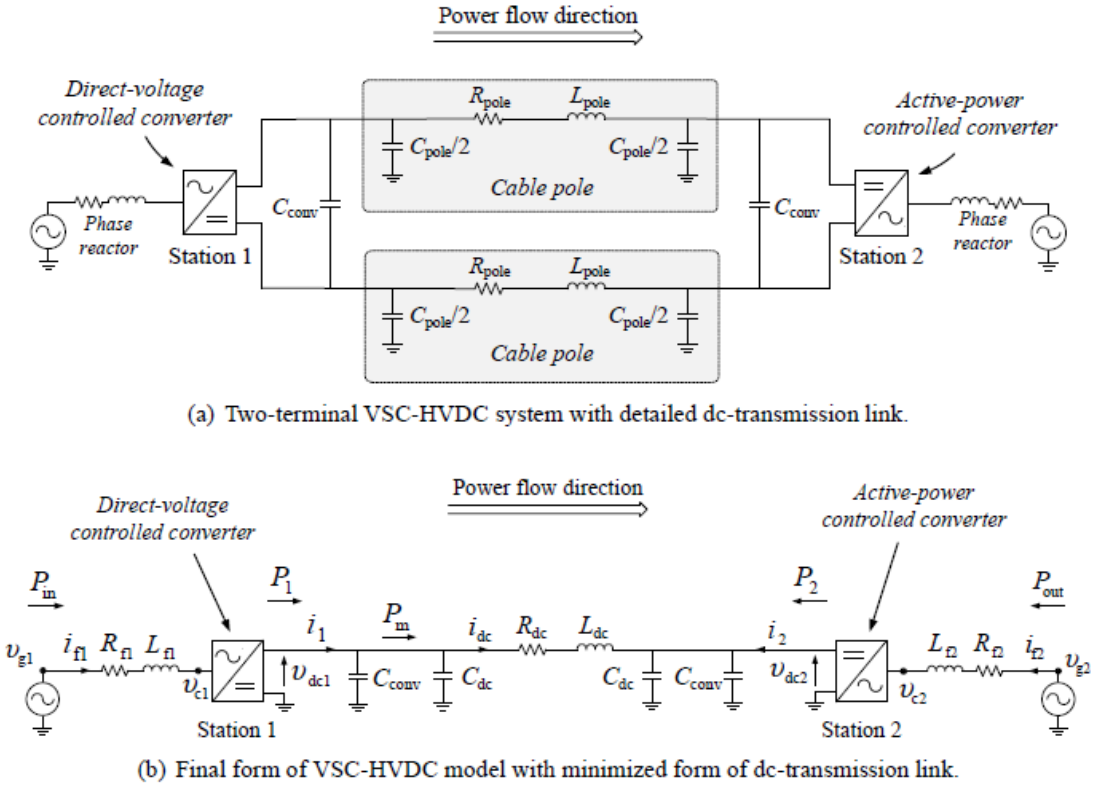

Figure 8 Two-terminal VSC-HVDC model.

A first objective is to derive a SISO representation of the two-terminal VSC-HVDC model, compatible to the depiction of Figure 7. This will allow a further investigation of the system in terms of passivity. The model under consideration is shown in Figure 8. The ac grids are assumed to be infinitely strong and are thus modelled as voltage sources, to which each VSC station is connected via a filter inductor (with inductance L_f and resistance R_f). The dc terminals of each station are connected to a dc capacitor with a capacitance C_{conv}. Each dc cable is modelled as a π-model. Given the physical characteristics of the symmetrical monopole configuration and considering balanced conditions, the model in Figure 8 (a) can be equated to the asymmetrical monopole model in Figure 8 (b). This model retains the same power and voltage ratings as the one in Figure 8 (a) and has the same dynamics. It is however simplified in form, assisting the later description of the model through equations. The transmission link values are defined as

$$R_{\mathrm{dc}} = 2 \cdot R_{\mathrm{pole}}, L_{\mathrm{dc}} = 2 \cdot L_{\mathrm{pole}}, C_{\mathrm{dc}} = C_{\mathrm{pole}}/4 \tag{2.3}$$

Choosing the correct type of input and output for the SISO representation of the system is not straightforward. The choice of the small signal deviation ΔW^* as input and ΔP_1 as output, allows a SISO formulation of the considered model, similar to the closed-loop form Figure 7, with *G*(*s*) being the input impedance of the dc grid and *F*(*s*) being the input admittance of the direct-voltage controlled VSC converter.

The Passivity approach requires both $F(s)$ and $G(s)$ to be stable. Choosing a Proportional-Integral (PI) controller for the direct-voltage control, leads to a stable $F(s)$. The dc-grid transfer function $G(s)$ has three poles, one of which is real. This real pole is always positive for a non-zero power transfer, rendering $G(s)$ unstable. However, in a related analysis in [Pinares, 2014], if $\frac{L_{\mathrm{dc}}}{C_{\mathrm{tot}}} << 2$ it is possible to approximate $G(s)$ with the transfer function $G'(s)$, where the real pole is fixed at zero. This is usually fulfilled in cable-type of lines, where the real pole is sufficiently close to zero due to the low inductance of the transmission link, but not necessarily in case of overhead lines.

The complete VSC-HVDC link is here evaluated and for scaling purposes the system is examined in per-unit. The passivity properties of the system may alter according to the operational conditions and choice of control parameters and passive elements. Their values are the same as in Table 1 with nominal power transfer and direct voltage, with the difference that the bandwidth a_{d} of the closed-loop direct-voltage control is allowed to vary. A cable-type of the transmission line is chosen with physical characteristics provided in Table 2. The cable length is here set to 50km.

The frequency response of $G'(s)$ is presented in Figure 9. A resonance peak is observed at ω=7.42pu, which is very close to the resonance frequency of the transmission link, having ω=7.40pu, as defined by (2.1). It can also be seen that the phase angle of the transfer function is always between -90° and 90° and since it is also marginally stable, $G'(s)$ is passive for all frequencies. Therefore, with $F(s)$ being already stable, the passivity analysis dictates that if there is a chance of instability in the closed-loop SISO system then $F(s)$ will necessarily be non-passive.

The system is now tested for three different bandwidths of the close-loop direct-voltage control: (a) a_{d}=0.4pu, (b) a_{d}=1.4pu and (c) a_{d}=2.4pu. Figure 10 shows the real and imaginary parts of $G'(j\omega)$ and $F(j\omega)$ for each of the cases. Observe that for the investigated cases, $\mathrm{Re}[F]$ is negative over a large part of the frequency domain, indicating that $F(s)$ is non-passive and therefore provides a hint for possible instability. Observe that $F(s)$ is non-passive for any amount of positive power transfer. In this case, the Nyquist criterion should be applied. For a certain frequency ω, the transfer functions $F(j\omega)$ and $G'(j\omega)$ can be regarded in terms of their real and imaginary parts as

$$F(j\omega) = F_{\mathrm{r}}(\omega) + jF_{\mathrm{i}}(\omega) \tag{2.4}$$

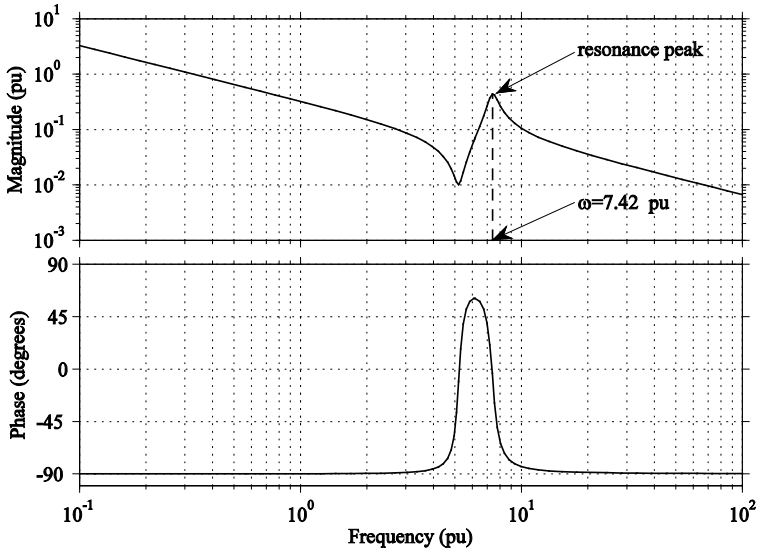

Figure 9 Frequency response of $G'(s)$

$$G'(j\omega) = G'_{\mathrm{r}}(\omega) + jG'_{\mathrm{i}}(\omega) \tag{2.5}$$

At a frequency ω_N the Nyquist curve $F(j\omega)G'(j\omega)$ crosses the real axis. There could be multiple such frequencies but if there is a poorly-damped potential resonance, then a ω_N will exist close to that resonant frequency with $F(j\omega_N)G'(j\omega_N)$ being close to the -1 value [Harnefors, 2007a]. If the closed-loop SISO system is to remain stable, then

$$F(j\omega_N)G'(j\omega_N) > -1 \Rightarrow F_r(\omega_N)G'_r(\omega_N) - F_i(\omega_N)G'_i(\omega_N) > -1 \quad (2.6)$$

Such a resonant frequency ω_N is found to exist for each of the examined a_d cases, with it being always close to the ω_{peak}=7.39 pu of $\mathrm{Re}[G']$, which is itself very close to the resonant frequency ω_{res}=7.4pu of the dc-transmission link. As it can be observed in Figure 10 (b), the value of $\mathrm{Im}[G']$ (equal to $G'_i(\omega)$) around ω_{peak} (and therefore ω_N as well) is very close to zero. A consequence of this is that the term $F_i(\omega_N)G'_i(\omega_N)$ in (2.6) becomes much smaller than $F_r(\omega_N)G'_r(\omega_N)$ and can thereby be neglected. Expression (2.6) can now be approximated by

$$F_r(\omega_N)G'_r(\omega_N) > -1 \quad (2.7)$$

and since ω_N is close to ω_{peak}, (2.7) becomes

$$F_r(\omega_{peak})G'_r(\omega_{peak}) > -1 \quad (2.8)$$

Since $G'_r(\omega_{peak})$=0.44pu, (2.8) provides the information that for an increasingly negative value of $F_r(\omega_{peak})$, the value of $F_r(\omega_{peak})G'_r(\omega_{peak})$ decreases with the possibility of surpassing -1 and the closed-loop system becoming unstable. This behaviour is observed in Figure 10 (a) where for an increasing a_d, the value of $F_r(\omega_{peak})$ is initially positive but gradually turns negative and keeps decreasing. This indicates that the increase of a_d decreases the damping of the resonant poles of the system and, eventually, leads to the instability of the system. This can be visually demonstrated in Figure 11 where the closed-loop poles of the system are plotted for the three different cases of a_d. Indeed, an increase of a_d causes the poorly-damped resonant poles of the system, with a natural frequency close to ω_{peak}, to become increasingly under-damped until they become unstable for a_d=2.4pu.

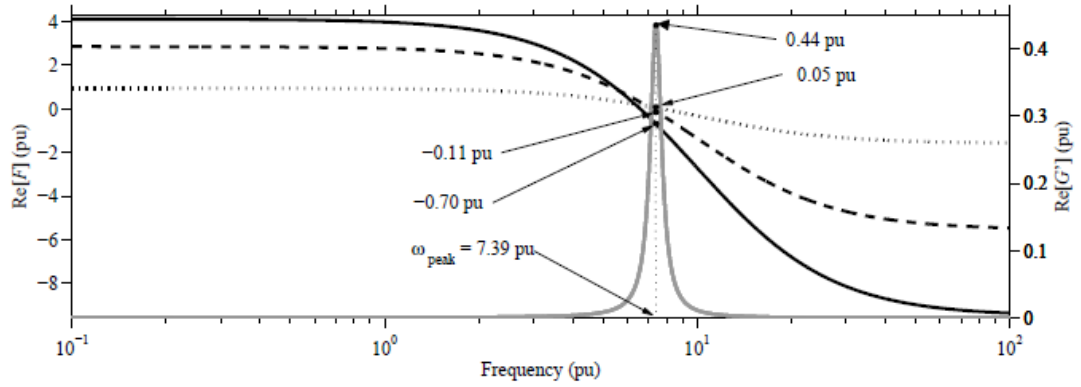

(a) Real parts of $F(j\omega)$ and $G'(j\omega)$.

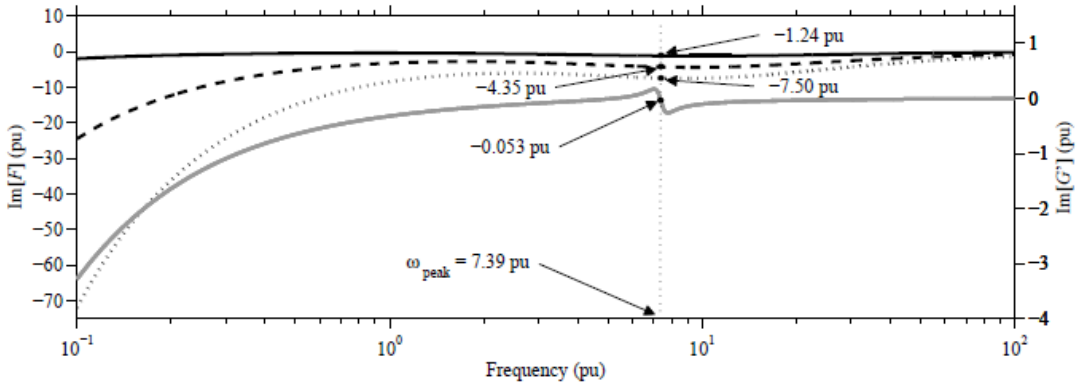

(b) Imaginary parts of $F(j\omega)$ and $G'(j\omega)$.

Figure 10 Real and imaginary parts of $F(j\omega)$ and $G'(j\omega)$. Solid gray: G'. Dotted: F for a_d=0.4pu. Dashed: F for a_d=1.4pu. Solid: F for a_d=2.4pu.

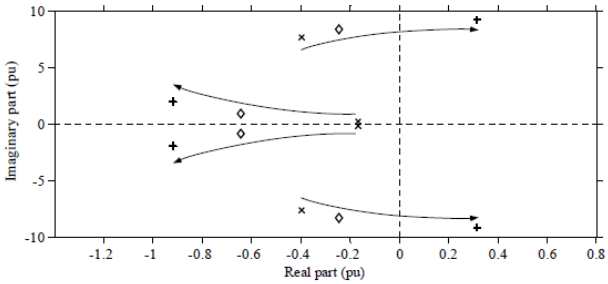

Figure 11 Pole movement of the closed-loop SISO system for a_d=0.4pu (x), a_d=1.4pu (◊), a_d=2.4pu (+). The fifth pole associated with the current-controller bandwidth a_{cc} is far to the left and is not shown here

2.1.1.4 Net-damping analysis of a two-terminal VSC-HVDC system

A useful tool in the frequency analysis of the stability of a system is the *Net-Damping* stability criterion. Its applicability can be investigated on SISO systems, identical to the one depicted in Fig. 4, where the frequency functions of the open-loop and feedback dynamics are expressed as

$$\frac{1}{F(j\omega)} = D_{\mathrm{F}}(\omega) + jK_{\mathrm{F}}(\omega) \tag{2.9}$$

$$G(j\omega) = D_{\mathrm{G}}(\omega) + jK_{\mathrm{G}}(\omega) \tag{2.10}$$

Canay in [Canay, 1982a] and [Canay, 1982b] used such a SISO representation in order to introduce the complex torque coefficients method for subsynchronous torsional interaction analysis of turbine -generator sets. In that case, $F(s)$ represented the turbine's mechanical dynamics and $G(s)$ the generator's electrical dynamics. Addressing $D_{\mathrm{F}}(\omega)$ and $D_{\mathrm{G}}(\omega)$ as damping coefficients and $K_{\mathrm{F}}(\omega)$ and $K_{\mathrm{G}}(\omega)$ as spring coefficients, the introduced method involves the evaluation of the net damping $D(\omega) = D_{\mathrm{F}}(\omega) + D_{\mathrm{G}}(\omega)$. If at each resonance of the closed-loop system applies

$$D(\omega) = D_{\mathrm{F}}(\omega) + D_{\mathrm{G}}(\omega) > 0 \tag{2.11}$$

then according to [Canay, 1982a], there is no risk for detrimental torsional interaction. Several examples where provided as proof of the statement but no strict mathematical proof. The method was shown in [Tabesh, 2005] not to correctly predict closed-loop oscillatory modes and instabilities. However, a mathematical proof of the positive-net-damping criterion (2.11) was provided in [Harnefors, 2011], using the Nyquist criterion. There, in agreement with [Tabesh, 2005], it was clarified that the net damping should be evaluated for the open-loop (not closed-loop) resonances, as well as for low frequencies where the loop gain exceeds unity.

As part of the proof process in [Harnefors, 2011], the Nyquist criterion is applied to the transfer function $F(s)G(s)$ with

$$F(j\omega)G(j\omega) = \frac{D_{\mathrm{F}}(\omega)D_{\mathrm{G}}(\omega)+K_{\mathrm{F}}(\omega)K_{\mathrm{G}}(\omega)}{D_{\mathrm{F}}^2(\omega)+K_{\mathrm{F}}^2(\omega)} + j\frac{D_{\mathrm{F}}(\omega)K_{\mathrm{G}}(\omega)-D_{\mathrm{G}}(\omega)K_{\mathrm{F}}(\omega)}{D_{\mathrm{F}}^2(\omega)+K_{\mathrm{F}}^2(\omega)} \tag{2.12}$$

To determine whether the Nyquist curve encircles -1, the imaginary part of (2.12) is set to zero, yielding

$$F(j\omega_{\mathrm{N}})G(j\omega_{\mathrm{N}}) = \frac{D_{\mathrm{G}}(\omega_{\mathrm{N}})}{D_{\mathrm{F}}(\omega_{\mathrm{N}})} \tag{2.13}$$

where ω_{N} is the frequency where the Nyquist curve intersects with the real axis. Usually, resonant frequencies are very close to events of intersections with the real axis and therefore constitute points where an encirclement of -1 could occur (thus instability of the closed loop) [Harnefors, 2011]. If (2.13) is larger than -1 then $D_{\mathrm{F}}(\omega_{\mathrm{N}}) + D_{\mathrm{G}}(\omega_{\mathrm{N}}) > 0$, giving (2.11) in the vicinity of a potential resonant frequency. However, this accounts only for $D_{\mathrm{F}}(\omega_{\mathrm{N}}) > 0$, as examined in the previous references. If $D_{\mathrm{F}}(\omega_{\mathrm{N}}) < 0$, relation (2.13) would give the following in order to avoid an instability

$$\frac{D_{\mathrm{G}}(\omega_{\mathrm{N}})}{D_{\mathrm{F}}(\omega_{\mathrm{N}})} > -1 \overset{D_{\mathrm{F}}(\omega_{\mathrm{N}})<0}{\rightarrow} D_{\mathrm{G}}(\omega_{\mathrm{N}}) < -D_{\mathrm{F}}(\omega_{\mathrm{N}}) \Rightarrow D(\omega_{\mathrm{N}}) = D_{\mathrm{F}}(\omega_{\mathrm{N}}) + D_{\mathrm{G}}(\omega_{\mathrm{N}}) < 0 \tag{2.14}$$

showing that extra attention should be given when applying the net-damping criterion, taking into account the nature of $D_{\mathrm{F}}(\omega)$ close to the resonant frequencies.

Compared to the passivity analysis, a benefit of analyzing the stability of a SISO system via the positive-net-damping criterion is that there is no need for each of the $F(s)$ and $G(s)$ to be passive or even stable. In fact it is not uncommon that one or both of the two transfer functions are individually unstable, but closing the loop through the negative feedback stabilizes the system. In such cases, the passivity analysis cannot be used, unlike the positive-net-damping criterion which can still be applied.

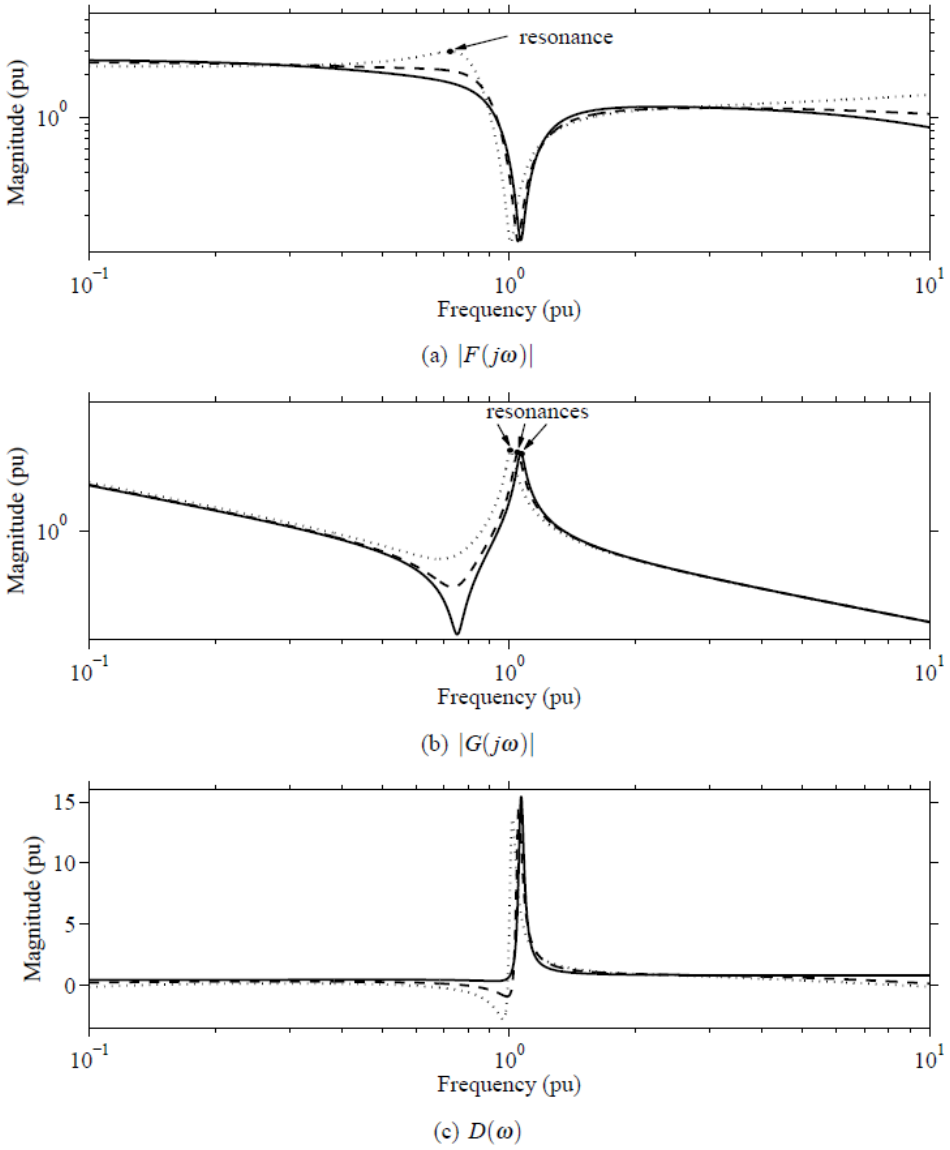

Figure 12 Frequency analysis of subsystems and total damping for transferred power equal to 0pu (solid), 0.5pu (dashed) and 0.9pu (dotted)

The system under investigation in this part is identical to the two-terminal VSC-HVDC model whose performance was examined in Section 2.1.1.2. That system featured long overhead dc-transmission lines and the transferred power was ramped up in stages, from 0MW (0pu) to 500MW (0.5pu) and finally to 1000MW (1pu). While the model appeared to be stable in the beginning, as shown in Figure 6, when the power reached 900MW (0.9pu), it became unstable with a resonance of 199.4Hz. Once the power started decreasing until 500MW, the stability was restored.

The SISO representation of the system considers the input-admittance transfer function $F(s)$ and the feedback transfer function $G(s)$ as defined earlier. The investigation starts by locating potential open-loop resonances of $|F(j\omega)|$ and $|G(j\omega)|$[1]. The frequency domain plots of those transfer functions are shown in Figure 12(a) and Figure 12(b), respectively, for the three different power transfers of interest; 0pu, 0.5pu and 0.9pu. Observing $|G(j\omega)|$, it is immediately apparent that there is always a single resonance at a frequency that is almost independent on the transmitted power and is very close to the resonant frequency of the dc grid, defined in (2.1). On the other hand, $|F(j\omega)|$ seems to exhibit no resonances for powers of 0pu and 0.5pu, but does have one for a power of 0.9pu with a frequency of 0.72pu. Table 3 displays the characteristic frequency of these resonances.

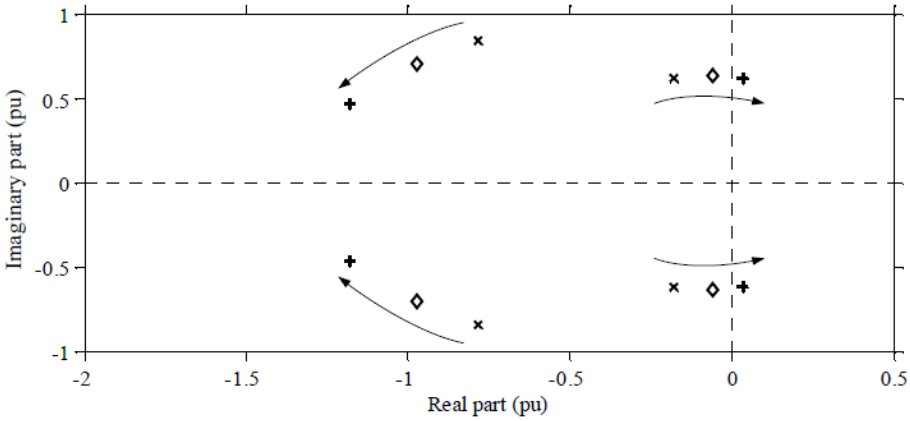

Figure 13 Pole movement of the closed-loop SISO system for transferred power equal to 0pu (x), 0.5pu ( ) and 0.9pu (+). The fifth pole associated with the current-controller bandwidth a_cc is far to the left and is not shown

The value of the damping $D_F(\omega)$ at the point of all the observed resonances is positive. Thereby, the positive-net-damping criterion of (2.11) will be evaluated. As it can be seen in Table 3, the total damping $D(\omega)$ is always positive at the open-loop resonant frequencies for powers of 0pu and 0.5pu. This means that the system should be stable, as demonstrated through the time-domain simulation of Figure 6. However, once the system has a transferred power of 0.9pu, $|F(j\omega)|$ develops a resonance at 0.72pu as mentioned before, where $D(\omega)$ is negative with a value of -0.32pu. This indicates an unstable system, confirming the unstable conditions displayed in Figure 6.

Table 3 Location of open-loop resonances and total damping

Power (pu)	$\|F(j\omega)\|$ resonant frequency (pu)	$\|G(j\omega)\|$ resonant frequency (pu)	$D(\omega)$ at $\|F(j\omega)\|$ resonance (pu)	$D(\omega)$ at $\|G(j\omega)\|$ resonance (pu)
0	-	1.07	-	15.3
0.5	-	1.05	-	13.46
0.9	0.72	1.01	-0.32	10.48

This behaviour can be observed in terms of the pole movement of the system for the different power transfers, as displayed in Figure 13. The poles are calculated for the closed-loop transfer function $F(s)/(1+F(s)G(s))$. As demonstrated, the system exhibits a pair of poorly-damped complex conjugate poles which are of concern due to their proximity to the imaginary axis. For a power transfer of 0pu and 0.5pu, these poles are stable. However, when the power increases to 0.9pu, the already poorly-damped poles become unstable with a predicted resonant frequency of 0.623pu, or 195.7Hz, which is very close to the 199.4Hz oscillation observed in the time-domain simulation.

Correlation between net-damping and damping factor

[1] $F(s)$ and $G(s)$ are both unstable. An attempt to locate their resonant points by plotting the bode plot in a way that a sinusoidal input signal is provided and the amplitude and phase of the output signal are measured, is not useful as the response of such systems for any input would be a signal that reaches infinity. However, plotting $|F(j\omega)|$ and $|G(j\omega)|$ still allows the identification of the local peaks that serve as the open-loop resonances and can be further used in the net-damping analysis.

In the previous section, it was shown how the net-damping criterion can provide direct information on whether a SISO system is stable or unstable. However there has been no information relating the criterion to poorly-damped or near-instability conditions.

Typically, the encirclement by the Nyquist plot of -1 occurs at low frequencies and in the neighbourhood of resonances [Harnefors, 2007a]. These resonances are usually identified with poorly-damped poles that move towards the RHP of the complex plane due to a change of a critical parameter (e.g. transferred power). When the system is on the verge of instability, the Nyquist curve intersects with the point -1. This occurs at a frequency ω_{crit} with the corresponding closed-loop system having either a real pole at the origin of the *s*-plane or a pair of marginally-stable complex-conjugate poles with a damped natural frequency $\omega_{\mathrm{d}} = \omega_{\mathrm{crit}}$. If these poles have not yet become unstable but are close enough to the imaginary axis, the Nyquist curve will cross the real axis on the right of -1 but in close proximity to it. This occurs at a frequency ω_{N} that is closely related to the damped natural frequency of the related poorly-damped poles.

If the system is marginally stable, its net-damping at the frequency $\omega_{\mathrm{N}} = \omega_{\mathrm{crit}} = \omega_{\mathrm{d}}$ is equal to zero

$$D(\omega_{\mathrm{N}}) = D(\omega_{\mathrm{crit}}) = D_{\mathrm{F}}(\omega_{\mathrm{crit}}) + D_{\mathrm{G}}(\omega_{\mathrm{crit}}) = 0 \tag{2.15}$$

Based on the previous analysis, it is here suggested that it is possible to correlate the level of net damping of a system measured at ω_{N}, with the existence of poorly-damped poles that are close to instability. The closer these poles approach the imaginary axis, the more the net damping $D(\omega_{\mathrm{N}})$ should approach zero until the poles become marginally stable and $D(\omega_{\mathrm{N}}) = 0$. The value that quantifies the level of damping for these poles is their damping factor. The closer the latter is to zero, the less damped the poles and the system is closer to instability.

The objective of this analysis is to provide a way through a solely frequency analysis of the system to determine whether there are poorly-damped poles critically close to the imaginary axis, without actually finding the poles of the system and the frequency characteristics of the poorly-damped poles. For this reason, four different scenarios are examined where the two-terminal VSC-HVDC system appears to have poorly-damped poles whose damping decreases with the change of a system parameter or operational condition, until they almost become marginally stable. In all cases, the damping of these poles is plotted in conjunction with the measurement of the net damping at the frequency ω_{N} where the Nyquist curve crosses the real axis closest to -1. As for the previous sections, the direct-voltage controller is at all times considered to feature the power-feedforward term.

The four different cases use the basic values as defined in Table 1 with the custom differences being identified in the following way

- Case 1: The system features overhead dc-transmission lines with their properties defined in Table 2 and their length is varied from 50-230km.
- Case 2: The system features overhead dc-transmission lines and the controller bandwidths a_{d} and a_{f} are equal and varied from 200-630rad/s.
- Case 3: The system features overhead dc-transmission lines of 230km in length and the transferred power at the inverter Station 2 is varied from 0-1000MW.
- Case 4: The system features cable dc-transmission lines with their properties defined in Table 2 and their length is varied from 26-43km.

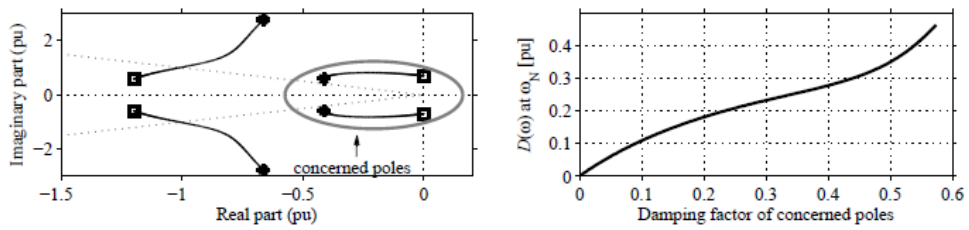

(a) Results for **Case 1** scenario.

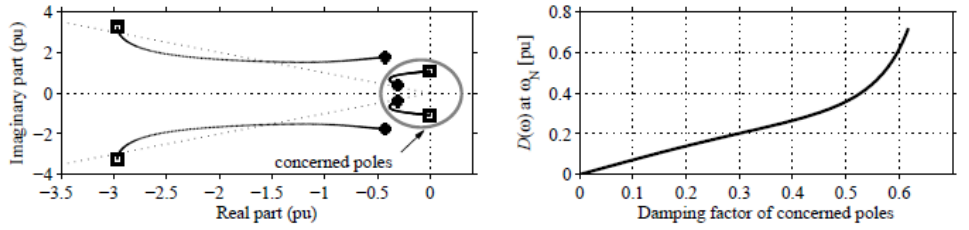

(b) Results for **Case 2** scenario.

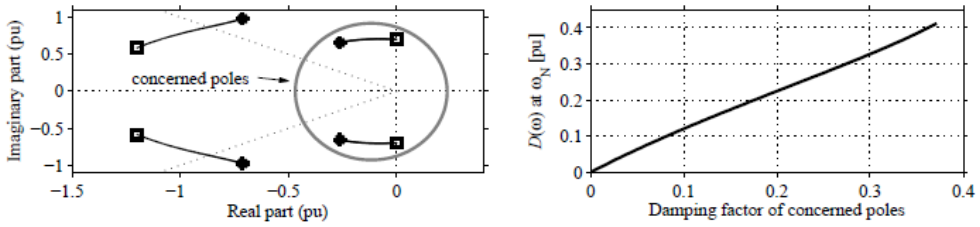

(c) Results for **Case 3** scenario.

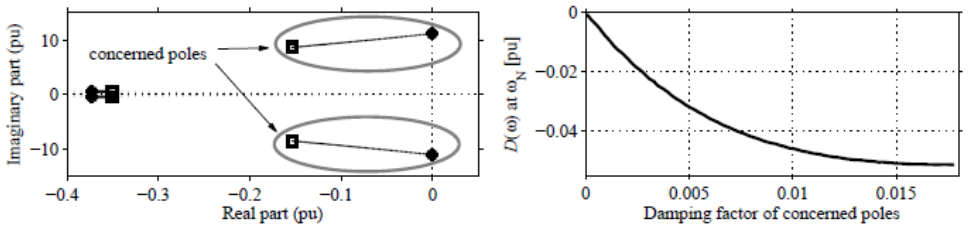

(d) Results for **Case 4** scenario.

Figure 14 Frequency analysis of poorly-damped systems. Four scenarios are examined with a different variable of the system changing in each of them. In the pole movement, "*" corresponds to the starting value and "□" to the final value of the variable. The fifth pole associated with the current-controller bandwidth $\mathbf{a_{cc}}$ is far to the left and is not shown here

Each of the graphs in Figure 14 shows the pole movement of the system for an increasing trend of the chosen variable, with the concerned poles being encircled. In the first three cases, the damping $D_{\mathrm{F}}(\omega_{\mathrm{N}})$ of the VSC input admittance is positive at ω_{N} and therefore for the system to be stable, the net-damping should be positive. This is confirmed in Figure 14(a)-(c) where the systems are already known to be stable and the measured net damping is indeed positive. On the contrary, in Case 4 the damping $D_{\mathrm{F}}(\omega_{\mathrm{N}})$ is negative and according to (2.14), the net damping should be negative to ensure stability. This is verified in Figure 14(d) where the stable system exhibits negative net damping at ω_{N}.

At this stage it is interesting to notice that for all the investigated scenarios there is a consistency in a sense that there is a monotonous relationship between the net damping of the system and the damping factor of the poorly-damped poles, provided that the latter are sufficiently close to the imaginary axis. The pattern that is exhibited in the right graphs of Figure 14 dictates that a net damping value $|D(\omega_{\mathrm{N}})|$ that is moving consistently towards zero, implies the existence of poorly-damped poles whose damping factor decreases consistently, until they become marginally stable. In this case, the system would be on the verge of stability. In fact, for poorly-damped poles which are quite close to the imaginary axis, the relation between $|D(\omega_{\mathrm{N}})|$ and damping factor

becomes almost linear. This provides the information that a certain rate of change in the net damping implies a similar rate of change in the damping factor of the concerned complex poles.
It is important to notice that the previous analysis reaches conclusions regarding

- the stability of the system
- the existence of poorly-damped poles
- the progression of the damping factor of the poorly-damped poles, for a change of a critical variable

by only using information from the frequency analysis of the system, without explicitly solving the characteristic polynomial to identify specific poles and define which of them are possibly poorly damped. Another comment on the results is that a relatively large absolute value of the net-damping measured at the frequency ω_N, suggests that even if there are poorly-damped poles, they are sufficiently far away from the imaginary axis and the risk of instability is minimized.

2.1.1.5 Damping analysis of a two-terminal VSC-HVDC system

A numerical approach and thereby pole movement of the system's eigenvalues is a very powerful tool to investigate the stability of a system and the impact of different variables (either system or control variables) on the system performance. However, one flaw in this kind of approach is that it does not provide a proper understanding of the impact of each parameter on the system stability. This is where the major advantage of an analytical over the classical numerical approach lies; by using an analytical method, the eigenvalues of the system can be expressed in symbolic form and this provides important assistance in getting a deeper understanding on how each single parameter impacts the stability and, more in general, the pole movement.

A great obstacle is that the analytical description of the eigenvalues of a high-order system is challenging and in many cases impossible. Although the eigenvalues of polynomials with a degree up to the 4th can be found analytically, the resulting expressions are usually very complex and uninterpretable if the degree is greater than two. Modelling a VSC-HVDC connection maintaining a good level of complexity, can lead to a system whose order can easily surpass the 10th order. However, under valid approximations, the description of a two-terminal VSC-HVDC connection can be reduced to a 4th-order system. This section focuses on the derivation of closed-form analytical expressions for the description of a two-terminal VSC-HVDC system's eigenvalues in terms of their real and imaginary part.

Approximating methods

The eigenvalues of a generic non-singular square matrix **A** are calculated by setting its characteristic polynomial $p(s)=\det(s\mathbf{I}-\mathbf{A})$ equal to zero and solving in terms of s. The solutions correspond to the eigenvalues of **A**. However as mentioned earlier, if the characteristic polynomial contains symbolic expressions, it is challenging to derive interpretable symbolic solutions while for more than four non-zero eigenvalues, it is generally impossible.

The determinant of a matrix that is triangular in form (either upper or lower triangular) equals the product of the diagonal entries of the matrix. If the matrix **A** is triangular, then the diagonal entries provide the eigenvalues of **A**. Consequently, the diagonal entries of A provide the eigenvalues of **A**. If matrix **A** has strictly real entries, has a block-triangular form and is known to have pairs of complex conjugate eigenvalues, then for each eigenvalue pair, a 2×2 sub-matrix will be found along the diagonal of **A**. However the opposite does not apply and the existence of such a 2×2 sub-matrix does not imply the existence of a complex conjugate eigenvalue pair. Assume that matrix **A** has the form

$$\mathbf{A}=\begin{bmatrix} a_{1,1} & & & & & \\ & a_{2,2} & \ddots & & \mathbf{0} & \\ & & a_{k,k} & a_{k,k+1} & & \\ & & a_{k+1,k} & a_{k+1,k+1} & \ddots & \\ & \boldsymbol{a}_{i,j} & & & a_{n-1,n-1} & \\ & & & & & a_{n,n} \end{bmatrix} \tag{2.16}$$

The eigenvalues of this matrix will be the set of real eigenvalues represented by all the diagonal entries of **A** (excluding those found within the 2x2 sub-matrix), as well as the eigenvalues of the 2x2 sub-matrix itself. The latter two eigenvalues will be

$$\lambda_{1,2} = \frac{a_{k,k} + a_{k+1,k+1}}{2} \pm \frac{\sqrt{a_{k,k}^2 + 4a_{k,k+1}a_{k+1,k} - 2a_{k,k}a_{k+1,k+1} + a_{k+1,k+1}^2}}{2} \quad (2.17)$$

If the expression under the square root is negative, i.e.

$$a_{k,k}^2 + 4a_{k,k+1}a_{k+1,k} - 2a_{k,k}a_{k+1,k+1} + a_{k+1,k+1}^2 < 0 \quad (2.18)$$

the two solutions in (2.17) represent a pair of complex conjugate eigenvalues, otherwise they represent two real poles. If block-diagonal matrix **A** is known to have *m* pairs of complex conjugate eigenvalues, there will be *m* 2×2 sub-matrices sufficing (2.18), along the diagonal of **A**.

Based on the previous analysis, if a random original state-matrix **A** is appropriately transformed to a *similar* matrix $\mathbf{A_o}$ that is upper or lower triangular and has the same eigenvalues, then the eigenvalues of the original matrix **A** can be found directly from the diagonal elements of $\mathbf{A_o}$. While it is impossible to find the *similar* $\mathbf{A_o}$ matrix of a high-order matrix **A** (dual problem with finding its eigenvalues), it is possible to find an approximation of $\mathbf{A_o}$, with small enough values on the upper or lower triangular portion of the matrix as follows

$$\mathbf{A}_o = \begin{bmatrix} a_{1,1} & & & & & \textbf{small} \\ & a_{2,2} & & & & \textbf{values} \\ & & \ddots & & & \\ & & & a_{k,k} & a_{k,k+1} & \\ & & & a_{k+1,k} & a_{k+1,k+1} & \ddots \\ & a_{i,j} & & & & a_{n-1,n-1} \\ & & & & & & a_{n,n} \end{bmatrix} \quad (2.19)$$

Then the elements of the diagonal can give the approximate eigenvalues of $\mathbf{A_o}$ and hence **A**. Two methods that can achieve this operation are used in this section. One of them is the iterative algorithm LR, which already exists in the literature but never used in power systems or control systems), and the other is the newly proposed Similarity Matrix Transformation (SMT). Their principles of operation are presented in Figure 15.

Application of approximating methods to a simplified two-terminal VSC-HVDC connection

The simplified model of a two-terminal VSC-HVDC model (similar to Figure 8(b)) is here used to derive a 4th order state-matrix **A**, which will lead to the calculation of four dominant eigenvalues. To achieve this, the effect of the Current Controller and the PLL at the stations is ignored assuming an instantaneous current response to the reference values, and connection of the stations to strong AC grids.

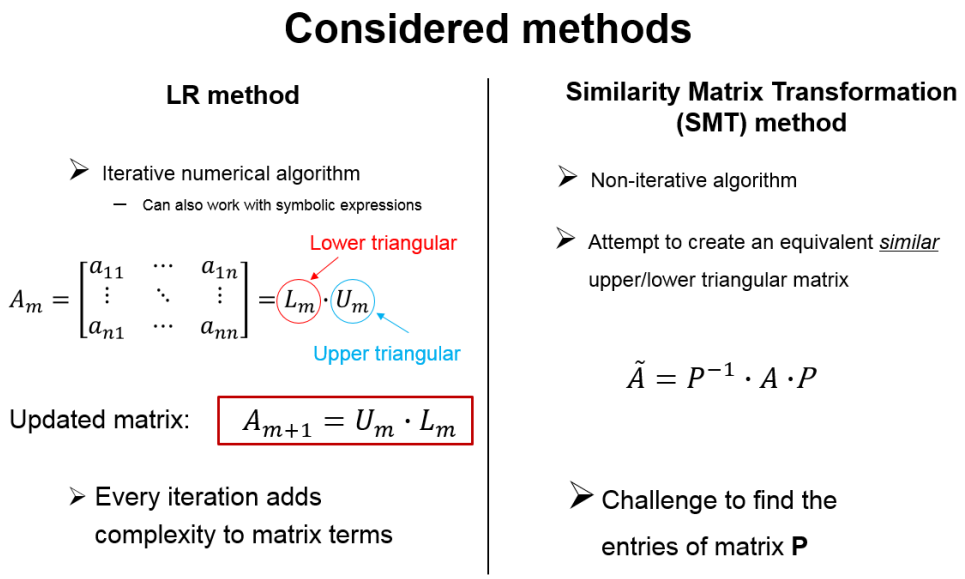

Figure 15 Principle of operation for the LR and SMT approximating methods

The use of the LR and the SMT algorithms resulted in the extraction of symbolic expressions for the four eigenvalues of the previous state-matrix. To provide a base of comparison, all the parameters of the system were kept constant at nominal values and a chosen parameter was allowed to vary. These values are shown in Table 4. The scenario where the cable length is varied from 20-600km is presented in Figure 16. For this variation, the exact numerical eigenvalues of the state-matrix **A** are juxtaposed to the eigenvalues derived by the LR and SMT methods, when the values of the parameters are replaced. It is shown that while both the LR and SMT show a good approximation of the poorly damped pole pair of eigenvalues, the LR does not perform so well in following the correct eigenvalue path for the other pair of complex conjugate poles (indicated as “well damped”). On the contrary, the SMT method performs quite well in approximating these poles as well. The same phenomenon was observed for a variation of the other system parameters as well, with the SMT performing better than the LR method.

Table 4 Rated parameters of the simplified VSC-HVDC link

P_b	rated active power	1000 MW
$V_{dc,b}$	rated dc voltage	640 kV
C_{conv}	shunt capacitor with time constant 4.1ms	20 μF
r	dc cable resistance per km	0.0146 Ω/km
l	dc cable inductance per km	0.158 mH/km
c	dc cable capacitance per km	0.275 μF/km
a_d	bandwidth of voltage controller	300 rad/s (0.95 pu)
a_f	bandwidth of power feed-forward filter	300 rad/s (0.95 pu)
length	transmission line length	100 km

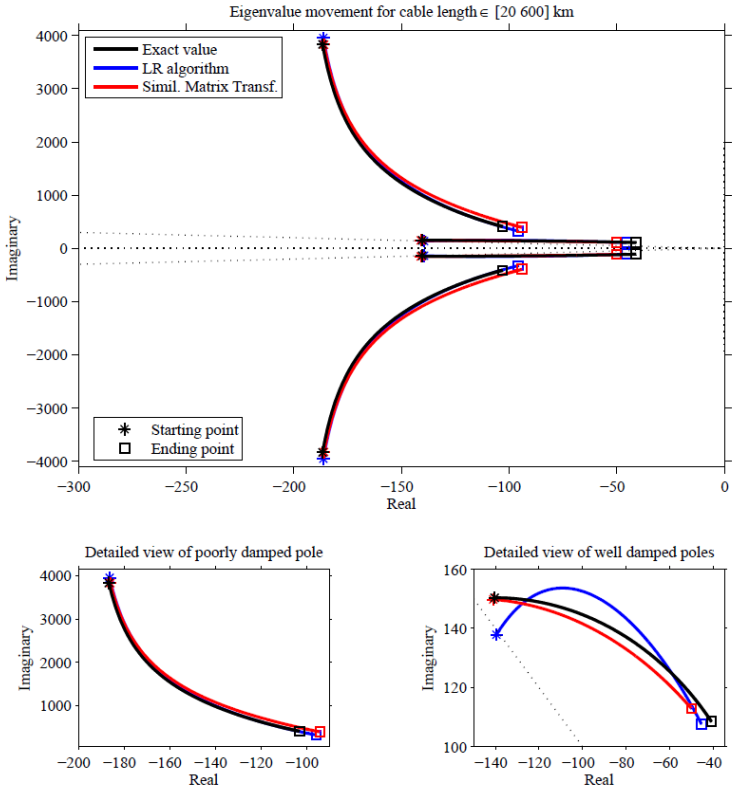

Figure 16 Comparison between LR, SMT and numerically derived eigenvalues for a change of dc-cable length

Having demonstrated a satisfactory approximation of the simplified system, the derived symbolic poles are then compared with the actual poles of a more detailed system model. The latter is designed as earlier but also considers the impact of the Current Controller on the system dynamics. Using the values of Table 4 for both systems and considering the bandwidth of the closed-loop current control $a_{cc}=10\cdot a_d$, the cable length is varied from 150-600km. The resulting pole movement is shown in Figure 17. Note that the detailed system is of fifth order and has a very well damped real pole that is not shown in the graph. As observed, the remaining four dominant poles of

the detailed system are successfully approximated by the symbolic expressions for the reduced 4th order system. These results show that the symbolic solutions derived in this article can successfully approximate the dominant poles of more detailed representations of the two-terminal system than the one used for their derivation.

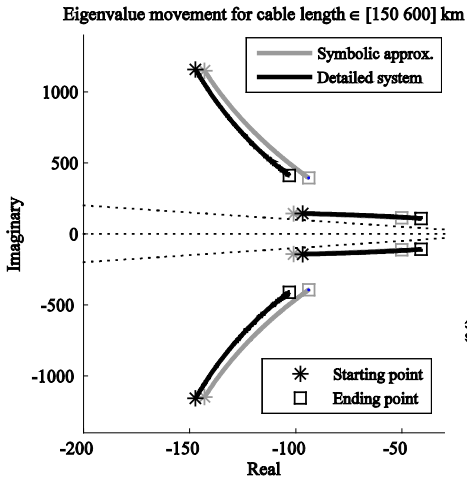

Figure 17 Comparison between the simplified model and a more detailed system with current controller

2.1.2 Control investigation in Multiterminal VSC-HVDC grids

The expansion of the point-to-point HVDC transmission concept into a multi-terminal arrangement, broadens the possibilities for a more flexible power transfer between ac grids and provides the means for a reliable integration of dispersed, high-capacity renewable power sources to highly interconnected power systems. However, moving from a two-terminal to a multiterminal scale, increases the technical requirements and adds complexity to the control strategies that can be applied.

2.1.2.1 Controller offering direct-voltage support in MTDC grids

Within the droop-control context in MTDC grids, a modified droop controller is proposed at this stage that can be utilized by any voltage controlled but also constant-power controlled stations connected to the grid. The benefit of such a controller lies in the fact that contrary to a conventional constant-power controlled station, the use of the proposed controller offers the possibility of controlling the grid voltage during contingencies while ensuring the transfer of the requested power in steady-state conditions.

A controller, which can be used to solve the problem of providing additional voltage support to an MTDC with droop-controlled and constant-power controlled stations, is proposed in this section. The same type of controller can be used in all stations. Its main design features are shown in Figure 18(a). It constitutes a cascaded structure which can be divided in two main parts. "Part 1" is a PI-based constant-power controller while "Part 2" is a Droop-based Direct-Voltage Controller (D-DVC). A selector is used to activate or deactivate Part 1, setting the operation of the complete controller to a constant-power or droop-control mode, respectively. When Part 1 is activated, the controller is in its complete form and is addressed to as "Power-Dependent Direct-Voltage Controller" (PD-DVC).

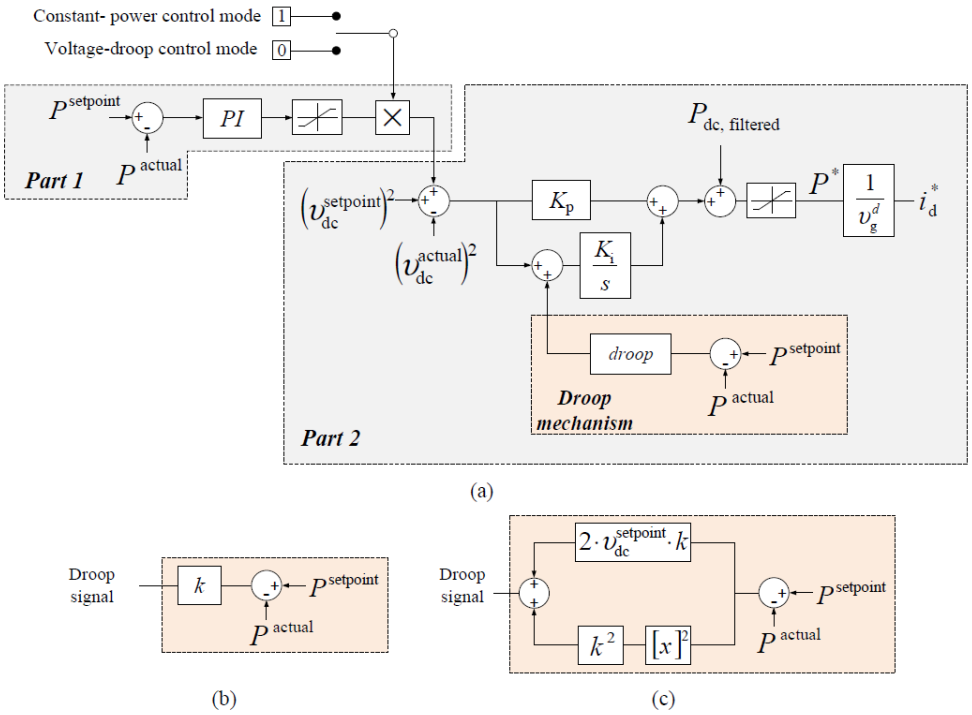

Figure 18 Power-Dependent Direct-Voltage Controller: (a) Complete structure of the controller, (b) Droop mechanism for linear relation between power and square of the voltage, (c) Droop mechanism for linear relation between power and voltage.

Voltage-droop control mode

In the Voltage-droop control mode, the controller reduces itself to the D-DVC Part 2 of the complete controller of Figure 18. This structure is similar to a standard droop controller but encapsulates a number of changes. The voltage control is not performed on the direct voltage but rather on the square of the latter. This is in accordance with the description of the direct-voltage controller suggested in [Harnefors, 2007b]. Following the same controller design, a power-feedforward term is included where the dc power P_{dc} of the converter is fed-forward through a low-pass filter $H_{\mathrm{f}}(s) = a_{\mathrm{f}}/(s + a_{\mathrm{f}})$ of bandwidth a_{f}.

Regarding the droop mechanism block, there are two options that can be selected. The first is shown in Figure 18(b), with the value amplifying the error $P^{\mathrm{setpoint}} - P^{\mathrm{actual}}$ being a droop constant *k*, exactly in the same way as in the conventional droop. However, if this is applied the controller would impose a linear connection between the steady-state power and the square of the voltage, rather than the power and the voltage as is observed in the conventional droop controller. Instead, the relation between power and the voltage will now be cubic. Nevertheless, given the small deviation region of the direct-voltage in operational conditions, the cubic curve is still close enough to the linear curve and is monotonous. The latter is more important than the linearity for the droop concept to function in a grid application. As such, the droop mechanism can be still designed with a droop constant.

If the linearity between steady-state direct voltage and active power are to be respected, the droop mechanism should be modified to the one presented in Figure 18(c).

Constant-power mode

During this mode, the PD-DVC controller of Figure 18(a) operates in its complete form including Part 1 and Part 2. This is a composite structure consisting of the D-DVC, with the addition of a standard active-power PI controller adding its output signal to the voltage error of the D-DVC. Actively adding a constant to the voltage error is equivalent to manipulating the setpoint $\upsilon_{\mathrm{dc}}^{\mathrm{setpoint}}$. As a result, the voltage-droop characteristic curve would move in a parallel motion to a new position.

Assume that a power-flow solver has calculated the necessary setpoints for the stations of a dc grid, including a constant-power controlled station. Focusing on the latter, its power setpoint P^{setpoint} is set equal to its desired constant power reference P^{*}, with its direct-voltage setpoint $\upsilon_{\mathrm{dc}}^{\mathrm{setpoint}}$ being provided by the power-flow

solution. These values are given to the controller of Figure 18 (a) and the station will ideally settle to a steady-state of $P^{\text{actual}} = P^{\text{setpoint}}$ and $v_{\text{dc}}^{\text{actual}} = v_{\text{dc}}^{\text{setpoint}}$ (if all the other stations are provided with setpoints from the power-flow solver). This point is indicated with " ×" in Figure 19, located on the droop curve of the station. It is noticed that Part 1 of the controller has not contributed at all in reaching this steady-state and its output is equal to zero.

If a contingency occurs in the MTDC grid (i.e. a station is lost), the droop-controlled stations react by following their droop curves in order to support the voltage stiffness of the grid and, as a result, re-adjust their steady-state power transfers. The station with the PD-DVC would react as well due to its droop characteristics, altering its power momentarily. However, in the new condition of the grid, the setpoint pair $\{P^{\text{setpoint}}, v_{\text{dc}}^{\text{setpoint}}\}$ cannot be followed anymore. Nevertheless, there is a request to respect the power setpoint in order to ensure constant steady-state power transfer. At this stage, Part 1 of the controller calculates a necessary corrective signal, which is added to the error at the input of the droop controller in Part 2. This operation is equivalent to the active calculation of a new voltage setpoint by an external master-level control, with the added advantage that it is performed locally. Consequently, the change in setpoints caused by the PI controller of Part 1 moves the entire droop characteristic along the voltage axis, as illustrated in Figure 19, until the pair of P^{setpoint} and an adequate voltage setpoint, which will allow the flow of P^{setpoint} in the grid, can be found on it. This new point is indicated with "·" in Figure 19. From the previous analysis it is also clear that the controller will operate seamlessly in pre- and post-contingency conditions, even if a random $v_{\text{dc}}^{\text{setpoint}}$ is originally provided.

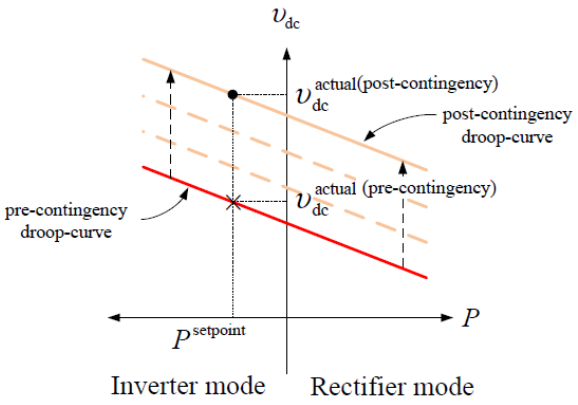

Figure 19 Operation of the PD-DVC before and after a contingency in the MTDC grid. "x" indicates the pre-contingency steady-state point while "." indicates the post-contingency steady-state point.

Application of controller in AC-side fault scenario

A five-terminal MTDC grid is considered. For simplicity, in all of the simulations the HVDC converters as well as their supplementary components (coupling inductor, transformer, ac-filters and dc-side capacitor) are considered identical in terms of ratings and physical values and their properties are described in Table 1. Any converter employing a droop functionality features the same droop characteristic *k*, equal to 2.5%. The layout of the five-terminal VSC-MTDC grid is presented in Figure 20, where for visual reasons a dc-line pair is shown as a single conductor. The grid is divided into distinct sections L_1- L_7 of overhead lines with assigned lengths of L_1=25km, L_2=50km, L_3=100km, L_4=50km, L_5=100km, L_6=70km and L_7=30km.

Two types of MTDC-grid control strategies are tested:

- "Control Strategy 1": All stations feature the PD-DVC of Figure 18(a).
- "Control Strategy 2": The constant-power controlled stations feature regular PI control with a rise time that is chosen to be close to the one achieved by the PD-DVC in "Control Strategy 1". The other stations are chosen to operate with the proposed PD-DVC in D-DVC mode (selector in position "0").

For consistency purposes, the following common settings are chosen:

- Stations 2 and 4 are in constant-power control mode.
- The ac-sides of all VSC stations are connected to infinite buses apart from the stations close to which the faults occur. These are connected to an ac grid of Short Circuit Ratio (SCR) equal to 2.

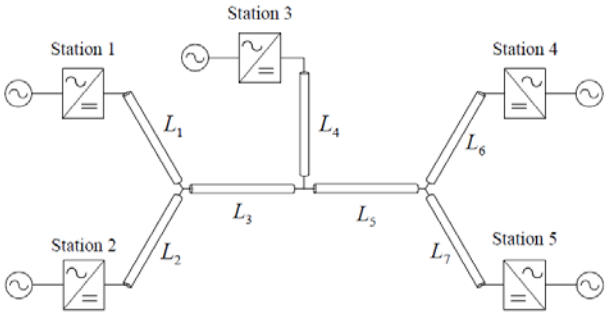

Figure 20 Testing configuration of a five-terminal VSC-MTDC grid

The distance of the fault location from the VSC station terminals has a large effect on the response of the station. The closer the fault is placed to the VSC station, the more fault current contribution is bound to come from the station rather than the connected ac-network. In the present simulation scenario, the fault is chosen to be located close to Station 2. Namely, the equivalent grid impedance of the associated ac-network (which has been calculated for SCR=2) is split into two parts in series connection. The first one is equal to the 80% of the grid impedance and is connected to the infinite ac-source while the other part is equated to the rest 20% of the impedance and is finally connected to the VSC station terminals. A small resistor is connected between the connection point of the two impedances and the earth, through a breaker.

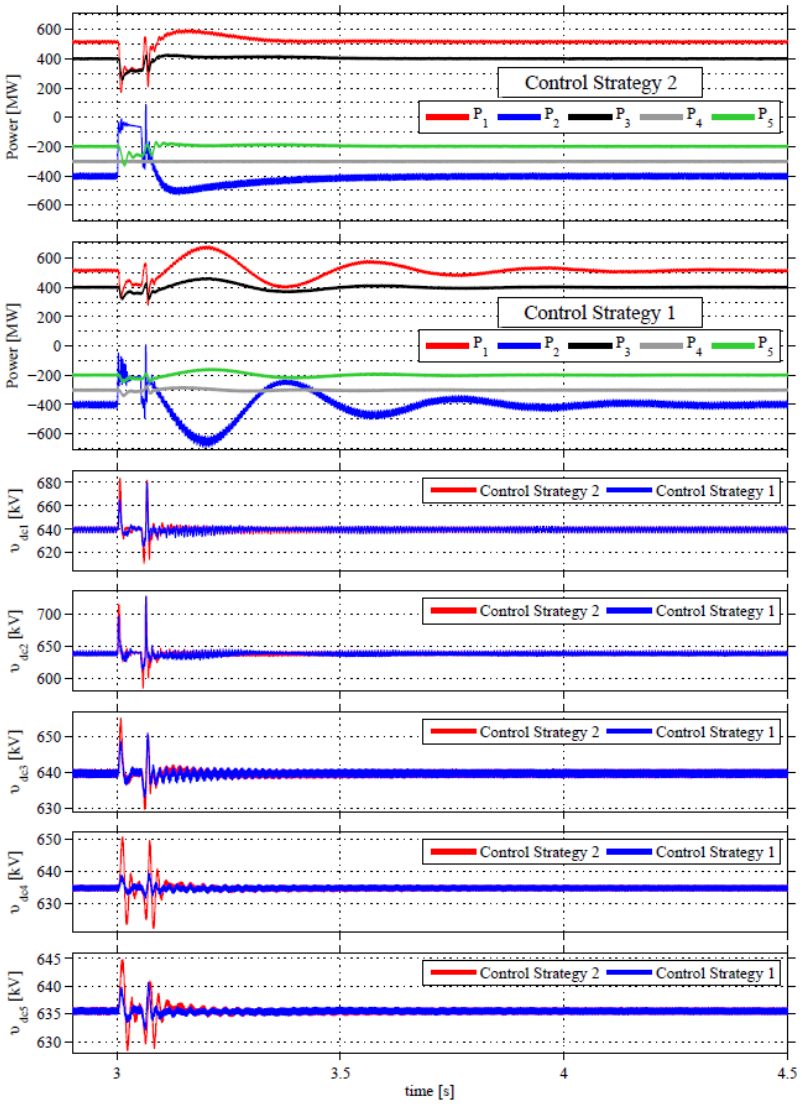

Figure 21 Active-power and direct-voltage response of the five-terminal MTDC grid using the "Control Strategy 1" and "Control Strategy 2" schemes. An ac-side fault is applied close to Station 2 at t=3s.

While being in steady-state conditions, the breaker closes at t=3s and then opens after 50ms. This causes the voltage at the fault location to drop to approximately 22% of the original 400kV. The power and direct-voltage response of the system for the two different types of control strategies is presented in Figure 21. For the "Control Strategy 2" control mode, the power references of the inverters are closely followed throughout the event, apart from the immediately affected Station 2 which experiences a great power change. The response of the droop-controlled stations is fast and the initial power flow is quickly restored after the fault is cleared. On the other hand, the direct-voltage, at the beginning and the clearing of the fault, exhibits large magnitude deviations followed by relatively poorly-damped high frequency components.

When the "Control Strategy 1" scheme is used, the power response of all stations is affected. During the fault, the power of the stations seems to change with less severity than in the "Control Strategy 2" scheme. In fact, the immediately affected Station 2 seems to be able to still export almost 200MW to its ac-side (rather than only 50MW in the "Control Strategy 2"), implying that the droop controlled stations do not have to significantly alter their contribution. After the fault clearing there is a low-frequency power oscillation until the systems quickly settles again at t=4.2s. This low frequency oscillation is identified to most systems that feature a wide use of direct-voltage droop and reflects the effort of the system to find a new power-voltage settling point, based on the distributed droop curves. Its frequency and magnitude deviation is mostly affected by the droop constant *k*.

In general, the direct-voltage response is less abrupt and better controlled compared to the one achieved with the "Control Strategy 2" control. The poorly-damped oscillations experienced previously are now slightly better damped but the major difference is identified at the voltage overshoot at the beginning and the duration of the fault, which is significantly reduced. In the same manner, the voltage overshoot at the moment of fault-clearing is generally reduced with the only exception of Station 3 where the "Control Strategy 1" scheme features just slightly higher overshoot than the "Control Strategy 2" control.

Nevertheless, the post-fault power response of the system employing the "Control Strategy 1" scheme exhibits relatively large oscillations, compared to the system with the "Control Strategy 2" scheme. It was further found that their frequency is related to the value of the droop constant *k*. Despite the fact that these oscillations are quickly damped (approximately 1s after the clearing of the fault), their magnitude is large enough to consider such a power flow behaviour as undesired in an actual MTDC. This calls for modifications in the control algorithms.

2.1.2.2 Controller for increased power-flow handling

In principle, droop-based strategies are designed in a way to secure that the direct voltage of the grid lies within strict boundaries under normal operation. However, in a post-fault scenario where there is a change in the dc-grid layout (i.e. an HVDC station is disconnected), this strategy would sacrifice the accuracy of the power flow.

Considering a conventional D-DVC, a relatively small value of the droop constant *k* implies that the controller is restrictive towards voltage and will not allow a large variation of the direct voltage for a large variation of the power. In contrast, a relatively large value of *k* renders the controller restrictive towards power, allowing a small variation of power in case of large changes of the dc-link voltage. In an MTDC grid, it is necessary to maintain the voltage within a strict margin for proper operation of the system; at the same time it is important to maintain the desired power flow in the different stations not only in steady-state, but also in case of unexpected events such as faults or unplanned disconnection of a station. Droop-controlled converters that are expected to maintain their the power flow to a large extent, require large values of *k* while converters that are mainly responsible for maintaining the direct voltage and are expected to contribute the most power during unexpected events require low values of *k*.

However, as investigated in [Rault, 2012], in a MTDC where there are stations using conventional droop control with high values of *k* (in the range of 60-100% instead of the more conventional 2%) the chances of reaching instability in the grid are very high. Therefore a new controller is here proposed to accommodate the use of large droop constants in order to offer better dynamic response during fault events or power scheduling changes.

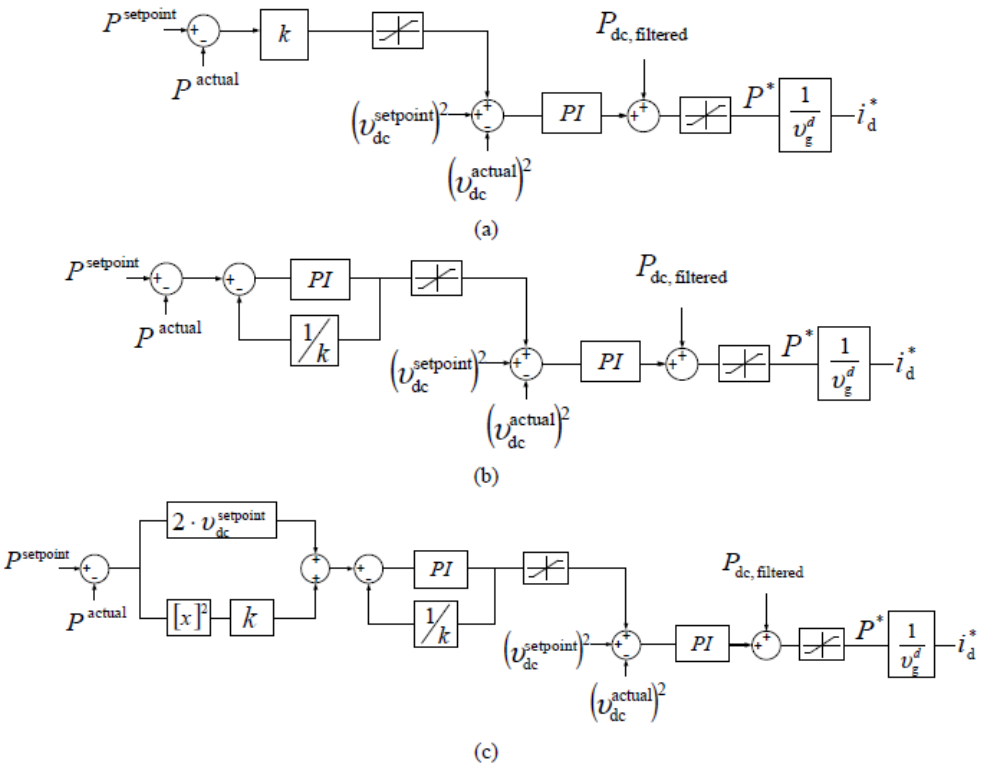

Figure 22 (a) Conventional D-DVC with linear relation between power and square of the voltage, (b) Proposed controller with droop mechanism for linear relation between power and square of the voltage, (c) Proposed controller with droop mechanism for linear relation between power and voltage

Proposed Controller

The proposed controller is presented in Figure 22 and is a modified version of a conventional D-DVC depicted in Figure 22(a), which in turn is practically identical to the one in Figure 18(a) (with the selector in position "0"). The branch that provides the droop-based correcting signal to the voltage controller consists of a PI-based droop controller that operates on the error between the reference power P^{setpoint} for the station of interest and the actual transferred power P^{actual}. The controller's corrective signal is added to the reference $\upsilon_{\text{dc}}^{\text{setpoint}}$ of the standard direct-voltage controller.

Steady-state properties

The steady-state behaviour of the proposed controller can be analysed in the simpler case of the version in Figure 22 (b). Observing the branch generating the droop signal, it is possible to derive the closed-loop transfer function of the combined PI controller with the negative feedback of gain 1/*k*. The steady-state gain, or *dc-gain*, of this transfer function is *k*. This means that in steady-state, the investigated controller behaves exactly like the conventional D-DVC with droop constant *k* of Figure 22(a). Therefore, the use of the conventional or the suggested controller has no effect on the final power flow that will be established in the MTDC grid, as long as the same setpoints and droop constants are provided to the respective stations.

Dynamic properties

In the conventional droop controller of Figure 22(a), the droop signal is created by comparing the given power setpoint P^{setpoint} of a station to the actual transferred power P^{actual}, amplified by the droop constant *k* and then added to the voltage setpoint $\upsilon_{\text{dc}}^{\text{setpoint}}$. This means that whenever there is a difference between the power setpoint and its actual value, the voltage controller will try to set the direct voltage equal to the voltage represented by the predetermined voltage setpoint, corrected by the value of the droop signal. When *k* is relatively large, rapid and large power flow changes in the system could lead to a large droop signal passing directly to the voltage controller. This explains from a macroscopic point of view the instabilities observed in [Rault, 2012]. Conversely, the proposed controller features a PI-based droop signal mechanism. Even if in steady-state the droop part of the controller reduces to a proportional gain *k* (in the case of Figure 22(b)), during transients it provides a filtering

action, preventing large and rapid droop signals from reaching the voltage controller. This allows improved dynamic performance when changing setpoints, as well as in fault or station disconnection events.

Application of the proposed controller

A four-terminal MTDC grid is considered as shown in Figure 23. The grid is divided into distinct sections L_1-L_1 of overhead lines with assigned lengths of L_1=100km, L_2=100km, L_3=100km, L_4=160km and L_5=40km. All stations are connected to infinitely strong grids, which are represented by 400kV voltage sources.

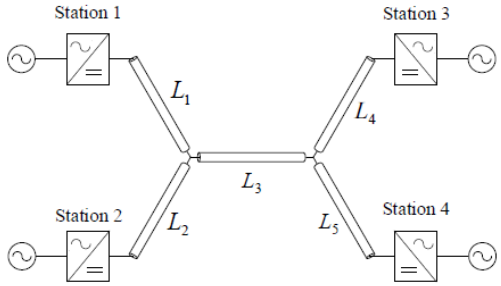

Figure 23 Testing configuration of a four-terminal VSC-MTDC grid

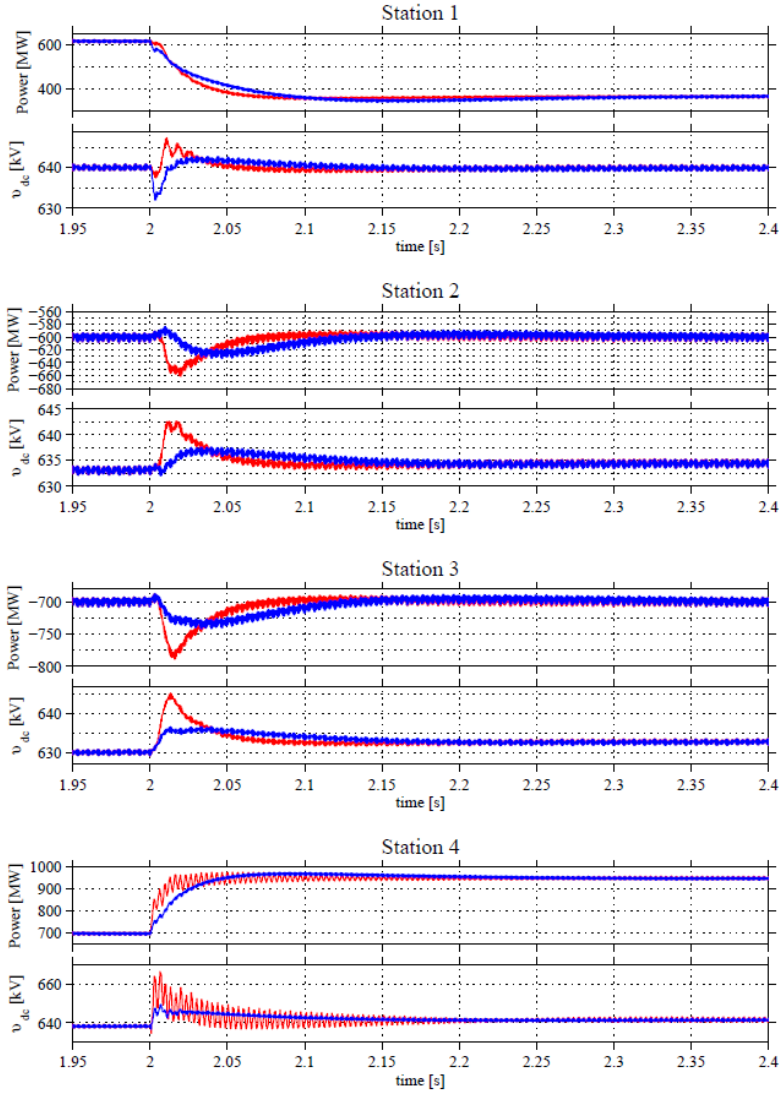

Figure 24 Power and direct voltage response in the four-terminal MTDC during a change of setpoints at t=2s. Blue color represents "Proposed" control while red color represents "Classic" control

Two different types of droop controllers will be utilized in the simulations: the conventional D-DVC of Figure 22(a) (addressed to as "Classic") and the proposed controller in its version of Figure 22(b) (addressed to as "Proposed"). In a conventional droop controller, where the voltage controller acts on v_{dc}, the droop constant *k* is defined by a percentage value e.g. 3%. This implies that if for zero power transfer the controlled station has a direct voltage at its terminals equal to $v_{\mathrm{dc},0}$, for rated power transfer the same voltage will drop by 3%. Additionally the connection between transferred power and direct voltage at the terminals of the station is linear. When the voltage controller, instead, acts on v_{dc}^2, there is no longer linear correlation between power and voltage but *k* can still be defined as earlier, corresponding to the percentage of dc-voltage change between zero and rated power transfer conditions.

The four-terminal MTDC grid used in the previous section, is simulated with all stations operating with the same type of controller at the same time (either "Proposed" or "Classic"). In both cases, the controllers of Stations 1, 2, 3 and 4 have k_1=2.5%, k_2=20%, k_3=20% and k_4=80%, respectively. This is exactly the same as in the strategy for the "Proposed" control strategy of the previous section, but now the same droop constants are applied to conventional droop controllers as well.

A sequence of events is implemented in consecutive stages, as described below

- Initially, all stations are in steady-state.
- At t=2s, new values of setpoints are provided to the stations. These are calculated based on a demand for an increase in power at Station 4 from the initial 700MW to 950MW, while Stations 2 and 3 maintain their power and Station 1 should still regulate the direct voltage at its terminals at 640kV.

The effect of the application of a new set of set-points to the stations is presented in Figure 24 where the power and direct voltage of each station is provided over time. Even though both types of control manage to establish the requested power flow changes in steady-state, the configuration using the "Classic" control appears to suffer from poorly-damped oscillations. This oscillation appears in the voltage and power of Station 4 and is located at approximately 298Hz. It should be reminded that this station features the highest value of droop constant. The performance on the other stations, which feature a smaller value of *k*, does not seem to be affected by the oscillation.

On the other hand, when the "Proposed" type of control is applied, there is no issue with the 298Hz voltage and power oscillation, which does not appear at all. Additionally, all stations (including Stations 2, 3 and 4 that feature relatively high values of *k*), demonstrate a smooth power and voltage response, ensuring the dynamic integrity of the system. Furthermore, all stations exhibited a high overshoot peak when the "Classic" control was chosen. This type of control appears to have a fast response, which in turn leads to high overshoots in the voltage response during the application of the new setpoints. On the contrary, the "Proposed" type of control seems to perform in a smoother manner, maintaining the voltage very close to the nominal values with insignificant overshoots and no poor damping issues.

2.2 Transients and protection in HVDC offshore grids

2.2.1 HVDC Cable modelling

Investigation of HVDC cables have in the past years become a necessity due to the increased deployment of HVDC around the world. Today with further usage of HVDC due to the VSC and a large increase in HVDC connected WPP's, this problem is again of relevance, how to carry out the simulation and design of the power transmission systems for HVDC links, including long submarine HVDC cables. Obviously, a new cable model with a higher accuracy, especially ever more popular multi-terminal HVDC, is required. Detailed mathematically calculated π-circuits equivalent are known to give relatively good simulation results for cable. However when long distance cables are to be modelled the number of π-circuit equivalents increases drastically. Thus the computation time in most time domain programs becomes unacceptable. A solution for a simple and accurate time domain cable model has yet to be found. As a well-known fact, the problem is due to that the cable and the cable screens etc. are inherently frequency dependent [Budner, 1970] and [Silva, 2010], and it is difficult to simulate the frequency dependent characteristics of a cabling system directly in time domain, for instance, by using the cable model of the EMTP and EMTDC program [CIGRE, 1996]. In the PSCAD/EMTDC program the two cable models, namely the Bergeron model and the frequency dependent model with a constant transformation, are included. A third model is

also given called “frequency dependent model with frequency dependent transformation”. This work will compare detailed mathematically calculated π-equivalent models to the PSCAD/EMTDC cable models. Frequency sweeps will be performed for all models to investigate and analyse the various cable model performances and frequency.

2.2.1.1 Mathematical model

The skin-effect exists for electromagnetic wave to travel in a conductive media, and is dependent on only the characteristics of the material and the propagating wave frequency. As a convenient measure to evaluate the skin-effects, the “skin-depth” concept is used. One can think of the wave as having essentially disappeared after penetrating a few values of the skin-depth. Normally, the skin depth, δ, in a homogenous conductive media is calculated by the following formula,

$$\delta = \sqrt{\frac{1}{\pi f \sigma \mu}} \tag{2.20}$$

where f is frequency, σ is the conductivity, and μ is the permeability. The skin-depths for the configuration of HVDC cable deep in seawater has to be found individually for the cable main conductor, the cable lead sheath, the cable armour steel tapes the cable armour steel wires and for the seawater [23].

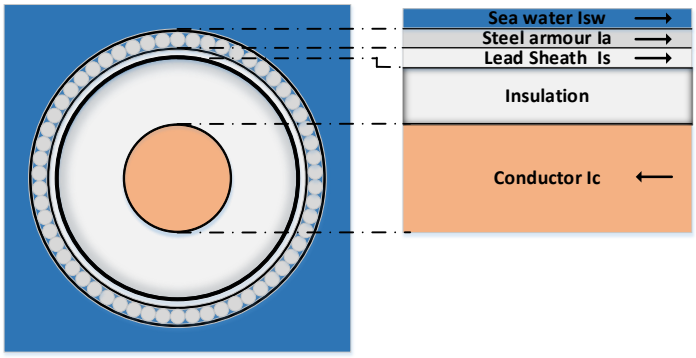

Figure 25 Cable cross-section

According to an ordinary design of a HVDC cable transmission system, the lead sheath and the steel armour of the cable are always connected together and earthed to the local earthing system at two terminations. The dc voltage is applied on the insulation between the main conductor and lead sheath. As illustrated as in Figure 25, the transmitted dc and low frequency current shall go through the main conductor and returns through the three different ways in parallel: 1) the lead sheath, 2) the armour and 3) the seawater. The reason is explained that if all of the currents in the conductors of returning path operate in the same direction, the electric and magnetic interaction within the returning path conductors through the insulations has to be very small. Only the internal impedances of the conductors of three returning path are dominant, and shall therefore be included in the cable model. Acceding to the basic concepts of cable model above, a π-circuit section per unit length for the low frequency cable model may be established as shown in Figure 26, where Z_1 is the internal impedance of the main conductor of cable and Ze is the total impedance of the current returning path. For the main conductor the method is to use a R-L circuit of some type to approach the frequency characteristics of the impedance Z_1 for which has an inductive characteristics. With a ladder-shape circuit, the boundary condition is that the impedance Z_1 at dc reduces to the parallel combination of all resistors, R1 through Rn, and equals to the dc resistance of the cable main conductor.

$$Z_1 = Z_2(f_2) // Z_3(f_3) ..... // Z_n(f_n) \tag{2.21}$$

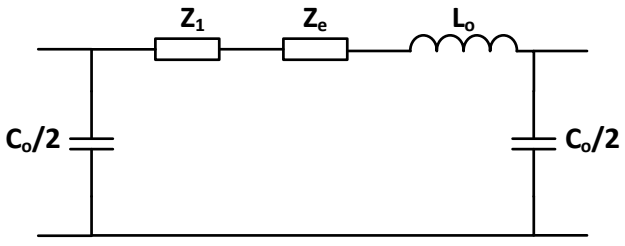

Figure 26 Mathematical π-model

The calculation of Ze is formulated as equation.

$$Ze = Ze_2 // Ze_3 // Ze_4 // Ze_5 \quad (2.22)$$

where the parameters are Ze_2 for the internal impedance of lead sheath, Ze_3 for the internal impedance of the armour steel sheath, Ze_4 for the internal impedance of the armour wires and Ze_5 for the internal impedance of seawater. The C_0 and L_0 are the capacitance and inductance over the main insulation between the main conductor and lead sheath, respectively.

At low frequency, Z_1 is equal to the dc resistance of the main conductor. At high frequency the skin effect must be included. The formula in [24] may calculate Z_1 in both low and high frequencies. That is,

$$\left.\begin{aligned} Z_1 &= \frac{\rho_1}{\pi r_1^2} + \frac{\mu_0 \mu_{r1}}{8\pi} \end{aligned}\right\} r_1 \le 2\delta_1 \quad (2.23)$$

$$\left.\begin{aligned} Z_1 &= \frac{1}{2r_1}\sqrt{\frac{\mu_0 \mu_{r1} \rho_1}{\pi}} \cdot \sqrt{f} \\ &+ \frac{1}{4\pi r_1}\sqrt{\frac{\mu_0 \mu_{r1} \rho_1}{\pi}} \cdot \frac{1}{\sqrt{f}} \end{aligned}\right\} r_1 \le 2\delta_1 \quad (2.24)$$

where δ_1 is the skin depth of the main conductor. The unit is Ohm/m for R_1 and H/m for L_1. The internal impedance of the lead sheath is given by the formula [21].

$$Z_{2,3} = \frac{\rho_2}{2\pi\sqrt{r_{2,4} r_{3,5} \cdot \delta_{2,3}}} \quad (2.25)$$

$$For\ r_{2,4} \ge T_{2,3} \le \delta_{2,3}$$

where $\delta_{2,3}$ is the skin depth of the lead sheath, the sheath thickness $T_2 = r_3 - r_2$, $T_3 = r_5 - r_4$ and the impedance unit is Ohm/m. Owing to the neglecting of the shielding effects of the armour wire ring, the total impedance, Z_4, shall be only the internal impedances of all wires. For each armour wire, the internal impedance, z4, including skin-effects may be calculated using the same method as for the impedance, Z_1, applying the formula (2.23) and (2.24). Then the total impedance is

$$Z_4 = \frac{1}{nw} z_4 \quad (2.26)$$

where nw is the total number of the armour wires. The formula for the self impedance of the seawater Z_5 of the immersed cable has been worked out by E Vance [25].

2.2.1.2 PSCAD/EMTDC model

In PSCAD/EMTDC we find four models that are used for cable model-ling.

1) π-Models: This model consists of the well-known lumped R and L, but an equally divided C at both ends. The concept of π-equivalent model is also used in a distributed system. The distributed π-model results in high-order functions which will take long time to be solved or simulated [Gustavsen, 1999].

2) Bergeron Model: The Bergeron model is a development of the simple π-model. It is a constant frequency model based on travelling wave theory. The cable is considered to be lossless infinite number of π-sections. It accurately represents the distributed L and C, but resistance R is added as a series lumped component. Thus the resistance is not represented in a distributed manner. Furthermore all parasitic components are not included in the model as it the case in the π-equivalent model. As a result of this the model has none or minimum frequency dependency. It is accurate at a specified frequency and is suitable for studies where the specified frequency is important [PSCAD]. However, for harmonics and electromagnetic compatibility (EMC) study, some frequency response information will be missed with this and the above simple π-model.

3) Travelling Wave Model in the modal domain (Frequency Dependent in Mode): As the name indicates, frequency dependent (FD) models are models that have frequency dependent cable parameters. This is achieved by using the cable's propagation and admittance matrices. When compared with the Bergeron models, the use of the frequency domain increases the results accuracy. In FD-models all calculations are performed in the frequency domain and the solutions converted to time domain by the using transformations such as Fourier-transform or Z-transform. The frequency dependent model in mode is achieved with a constant transformation matrix [Gustavsen, 1999]. The frequency dependent model represents the frequency dependence of all parameters (not just at the

specified frequency as in the Bergeron model). This model uses modal techniques to solve the cable constants and assumes a constant transformation. It is therefore only accurate for systems of ideally transposed conductors (or 2 conductor horizontal configurations) or single conductors.

4) Travelling Wave Model 2 (Frequency Dependent in Phase): The frequency dependent phase model also represents the frequency dependence of all parameters as in the above model. However, the problem of a frequency dependent transformation matrix will be overcome by formulating the model directly in the phase domain (without diagonalization). This is the most accurate model [Gustavsen, 1999] since it includes frequency dependence of internal transformation matrices.

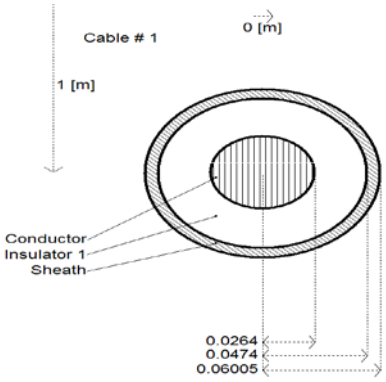

Figure 27 PSCAD coaxial cable model EMTDC configuration (for dc under-ground dc positive and

Both the Bergeron and the frequency dependent models in PSCAD/EMTDC are applied as comparison, which includes all the layers: copper core, insulation, armour and sheath, shown in Figure 27. Most simulation software cannot model segmented and stranded conductors, as it only allows the modelling of solid and hollow conductors, which due to skin effect are not used for cables with large cross-sectional areas. A conductor's DC resistance is calculated as shown in (2.27), where l is the conductor length, ρ the material's electrical resistivity and A the conductor's cross-sectional area. The cross-section of a segmented conductor as given in the datasheet is not equal to πr2, where r is the conductor radius. This difference is used to correct the resistivity as shown in (2.27), where ρ is the material's resistivity and ρ' the corrected resistivity.

$$R_{DC} = l\frac{\rho}{A} = l\frac{\rho'}{\pi r^2} \Leftrightarrow \rho' = \rho\frac{\pi r^2}{A} \qquad (2.27)$$

The DC resistance of the main conductor is given by the manufactory. However this resistance can be adjusted to the proper temperature level using the following equation.

$$R_{DC\_cor} = R_{DC}[1 + \alpha_{20}(\theta - 20)] \qquad (2.28)$$

Where R_{DC} is the given conductor resistance, α_{20} is the metal temperature coefficient at 20° per kelvin and Θ is the nominal operating temperature.

2.2.2 Simulation results

In this section the simulation results of the two models are compared and the results are explained. The mathematical model is compared to the three models available in PSCAD/EMTDC the Bergeron, the frequency dependent phase and mode models.

As mentioned earlier the Bergeron model doesn't include any parasitic components. Hence the model has none or minimum frequency dependency. This is clearly seen from Figure 28 where the EMTDC results seem more as a calculation errors compared to the mathematical model. This is clearly due to the change in frequency that the model isn't able to compensate for. Initially the cable is inductive, however with increasing frequency the skin and proximity effects will start to influence the impedance. Consequently making the cable capacitance dominate, nevertheless this behaviour isn't seen for the EMTDC Bergeron model.

When comparing to the Frequency Dependent (Mode) Model, the two models behaves similarly, due to the inclusion of frequency dependency. However it is clear that deviations will occur at higher frequencies. Increasing the cable length will increase the effect of the parasitic components. Hence the resonances are moved to lower frequencies Figure 29.

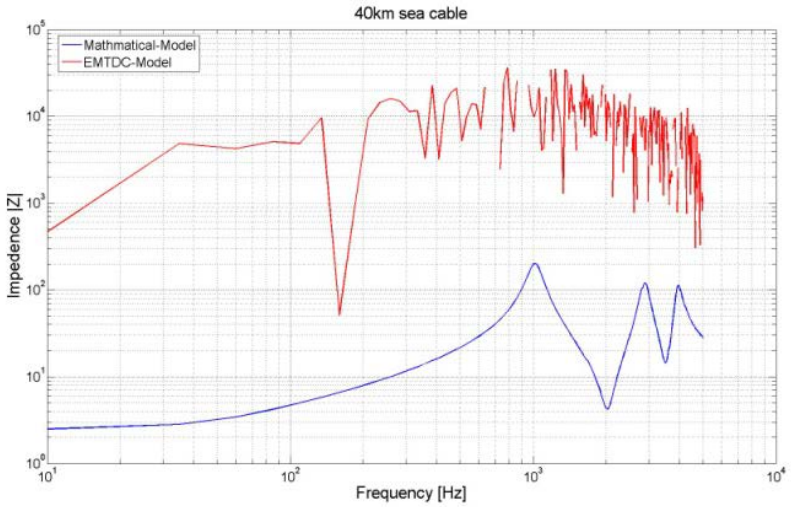

Figure 28 Bergeron Model compared to mathematical π-model 40km cable

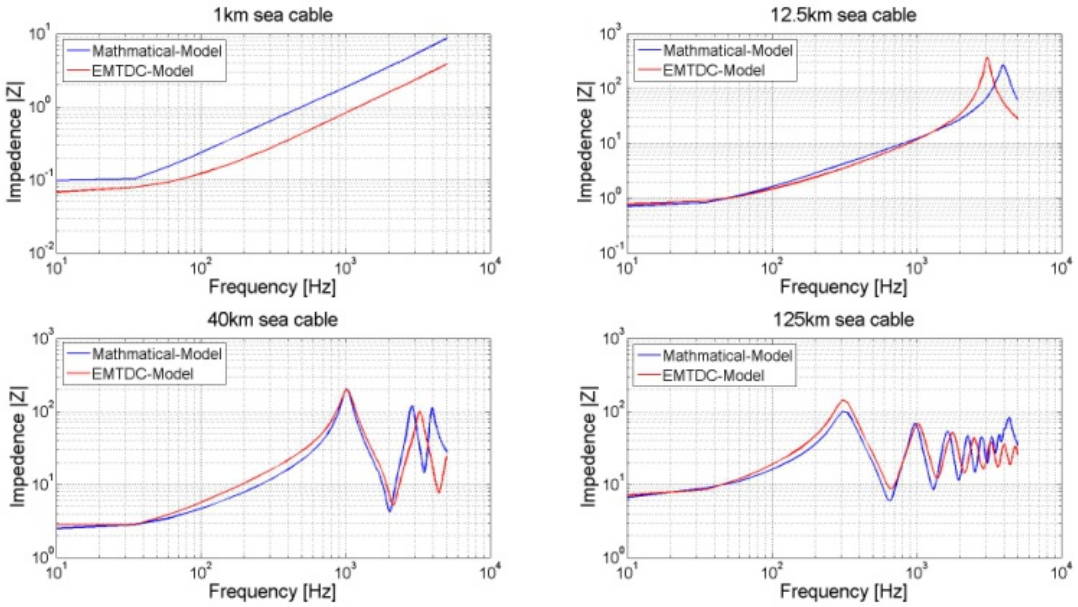

Figure 29 Frequency responds for Frequency Dependent (Phase) Model com-pared to mathematical π-model for different cable lengths

The Frequency Dependent (Phase) Model is according to PSCAD/EMTDC the best model to use when investigating high frequent behaviour since it includes frequency dependence of internal transformation matrices. Nonetheless when comparing the two FD models Figure 29 and Figure 30 they appear alike however the resonances are slightly shifted in frequency.

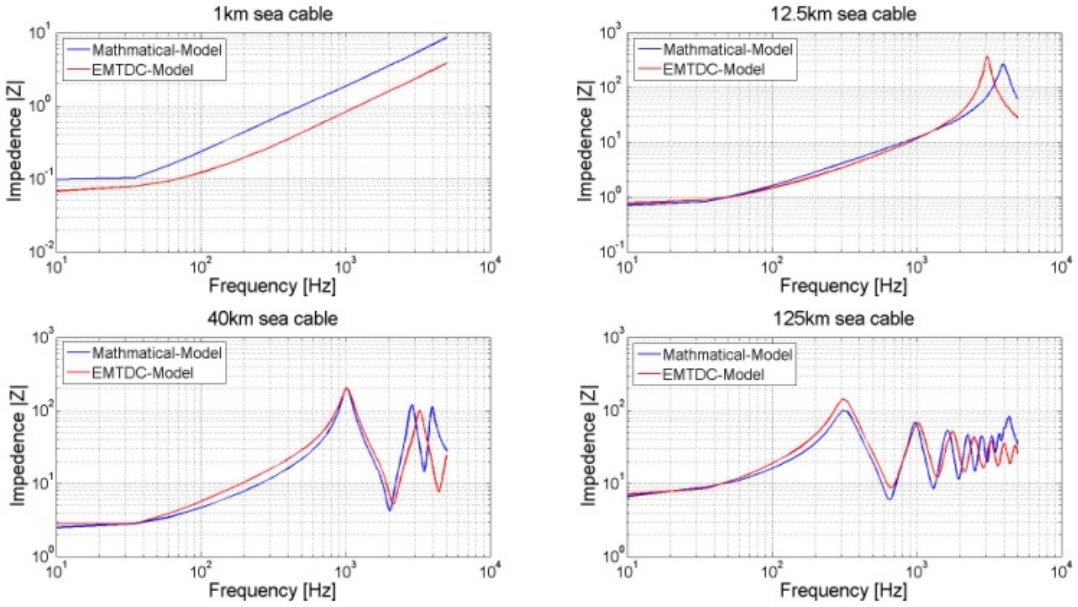

Figure 30 Frequency responds for Frequency Dependent (Phase) Model com-pared to mathematical π-model for different cable lengths

The mathematical π-model simulation results are close enough to the accurate cable model as shown in Figure 31 which zoomed to show some minor difference between the two simulation results. This is due to the various frequency components in the overcurrent. However, it clear that when looking at the low frequency oscillations the two models behaves almost identically.

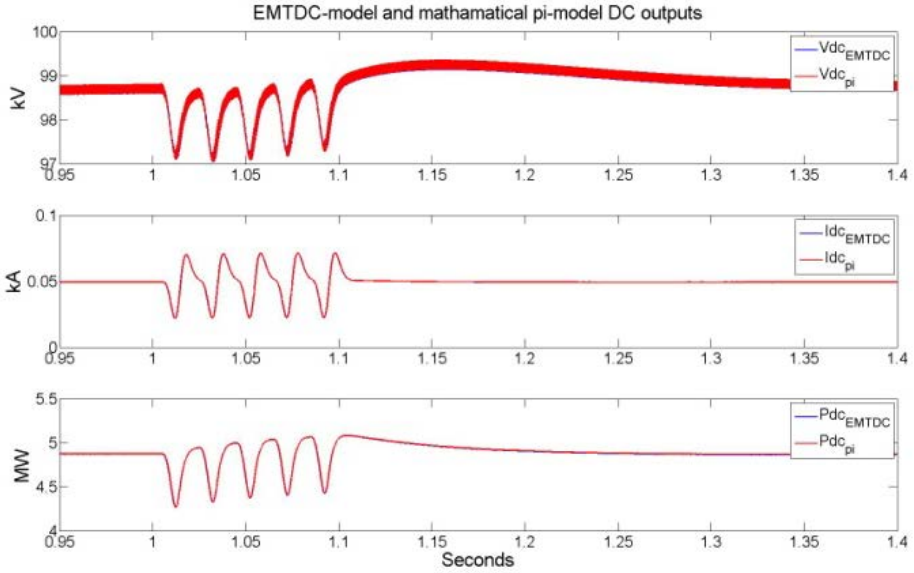

Figure 31 DC-line outputs for rectifier phase arm fault for both models

On the other hand, when simulating an energization using the two models Figure 32, the travelling wave behaves similar in both models. Nonetheless, in the mathematical π-model there is a high frequency oscillation of 4 kHz that cannot be found in the EMTDC model. This can be explained from the lower plots in Figure 30 where it is noticed that the EMTDC model has greater damping in the higher frequencies compared to mathematical π-model.

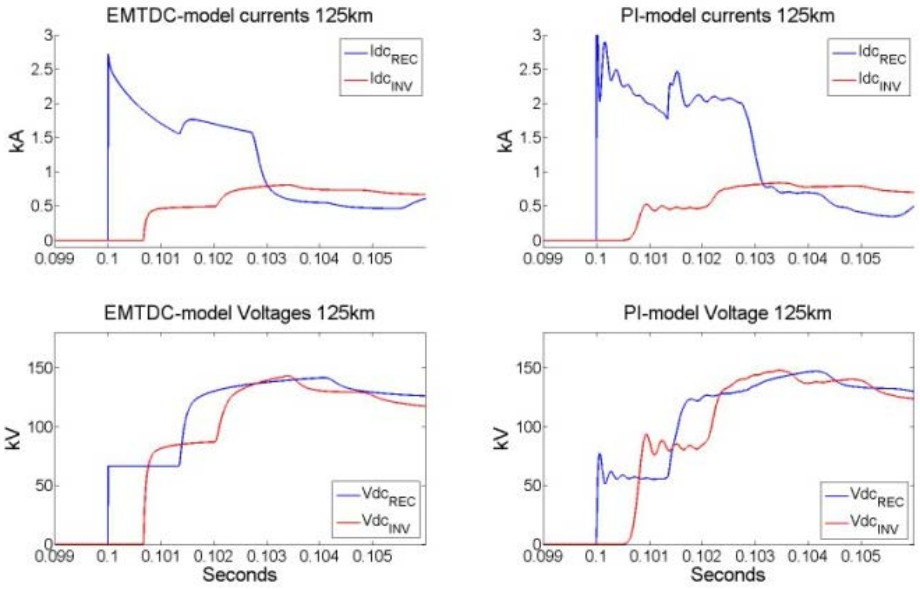

Figure 32 Energization simulation for both models

2.2.3 Modular Multilevel Converter modelling

One of the important aspects to be considered in connection with HVDC transmission systems is the transient behaviour, including both components that are able to generate steep flanks all around the power system and the transients that can occur in fault situations. For transient investigations in all kinds of power systems, usually high frequency models are necessary and for HVDC, this includes the converters, and, in particular regarding future systems, the more flexible VSC. Due to the VSC's ability to connect large offshore wind power plants to the onshore grid, and furthermore its ability of connecting asynchronous networks, while keeping the stability of the power system, it offers the opportunity for considerable integration of a larger share of renewable energy in the power system.

However the large number of switching elements in the modular multilevel converter (MMC) introduces a challenge for modelling the converter, on electromagnetic transient (EMT) simulation programs. To properly model the switching operation, the admittance matrix which has a size equal to the total number of nodes in the net-work subsystem, must be inverted (re-triangularized) every time a switch operates. In comparison to a two or three level VSC, the number of nodes (and, hence, matrix size) in the MMC is typically orders of magnitude larger. Also a large number of switching operations are necessary to generate the large number of output waveform levels. Therefore, without an approach such as the one proposed in this paper, it would be practically impossible to simulate HVDC systems containing MMC converters on EMT-type simulation pro-grams. However, since they do not model every level independently, they are not able to simulate abnormal operation of the converter such as failure of a module's control system or failure of the module itself. To overcome this drawback, this paper introduces a new approach to modelling the MMC, using the method.

2.2.3.1 High frequent modelling

In this section there will be presented a VSC-model based on passive components, suitable for numerical simulations in time domain. Even though VSC is a well-known topology, only few modelling approaches seem to be available, especially regarding transients and the related high frequency range. A possible reason for this might be the large number semiconductor switches in a MMC. Simulating such complex components with a considerable number of nodes in electromagnetic transient simulation programs such as PSCAD will have a negative effect on the calculation with simulation times being remarkably increased, often up to non-acceptable levels. Methods to simulate the converter without using any kind of semiconductors in order to reduce the simulation time are presented in the following. The model consists only of passive components representing the submodules in different states. For each state, new values are calculated for the converter. In order to cover the transient and high frequent range, all parasitic components, in in this case mainly of capacitive character had to be added to the model. All contributions are taken into account forming a mathematically and dynamically equivalent, which models

the entire converter. That accurate and well defined model allows for a considerable reduction of the simulation time.

2.2.3.2 Parasitic components

When trying to model the IGBT in terms of passive components, we again have two situations. The first case is that IGBT is turned off, thus no current is flowing through it, which means that the IGBT will constitute a capacitance only [Boonchiam, 2006]. However as there inevitably will be some inductance in the IGBT, this will have to be modelled as well by insertion of the inductor. Therefore the representation of the turned off IGBT will constitute in a capacitance in series with an inductor.

In case the IGBT is turned on, there will be some conductive losses, and these losses will represent the dynamic resistance of the IGBT [Duncan, 2010]. Furthermore the inductance of the IGBT will have influence in high frequencies and needs to be included. Also, as it can be seen in Figure 33, a capacitor has been placed in parallel, which is applied in order represent the capacitance of the IGBT. When the IGBT is turned on, a small forward voltage exists across the IGBT due to its dynamic resistance, and when examining the voltage characteristics of the IGBT-capacitance it is clear that the capacitance of the IGBT is significant at low voltages.

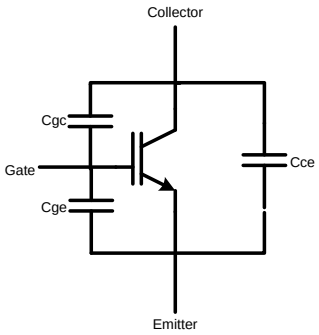

Figure 33 Capacitances of an IGBT [Duncan, 2010]

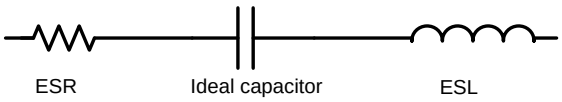

Figure 34 Equivalent circuit of the physical submodule capacitor. ESR: Equivalent Series Resistance, ESL: Equivalent Series Inductance

In the datasheet of an IGBT, usually a number of capacitances are listed. Figure 33 shows 3 different capacitances in an IGBT, with a capacitance between each terminal of the IGBT. The optimization of the gate control is not considered here. In addition, the sizes C_{ge} and C_{gc} are negligible compared with C_{ce}, hence it doesn't contribute to our work to represent them individually, these 3 capacitances have been combined into a single capacitance, Figure 34.

2.2.3.3 Submodule Capacitor

For transient investigations, the submodule capacitor cannot simply be modelled as an ideal capacitor, as this component besides the capacitance also includes some inductance known as the Equivalent Series Inductance (ESL), which is mainly caused by the leads and internal connections used to connect the plates or foil to the outside environment. It is obvious that the ESL will get increased influence at high frequencies, in particular when approach-ing the resonance frequency formed together with the capacitor.

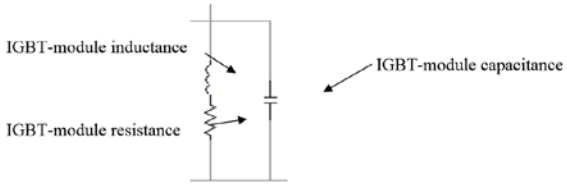

Figure 35 IGBT implementation in PSCAD

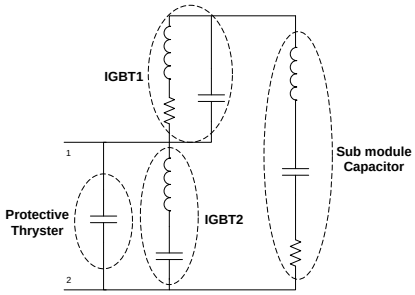

Figure 36 Principle submodule circuit in on-state as implemented in PSCAD

The resistance known as the Equivalent Series Resistance (ESR) covers the physical series resistance in the physical capacitor (e.g. the ohmic resistance of the leads and plates or foils). Including all parasitic components, the model of the submodule capacitor looks as seen in the Figure 35 (Barkhordarian, 2001).

2.2.3.4 Converter arm

When analyzing the submodule in the 2 situations the submodule can attain, it is clear that in either of the situations one of the IGBTs of the submodule will be turned off and the other will be turned on. Whenever the IGBT is turned on there will be a very small voltage drop across the IGBT due to the conducting resistance, this of course depends upon the collector-emitter voltage and the DC-collector current. This fact also requires that the capacitance of the IGBT, whenever the IGBT-module is turned will be represented accordingly. However as seen in the figure above, displaying the capacitance of the IGBT-module as a function of the collector-emitter voltage, does not show the relation between these parameters at higher voltages, and as the IGBT will experience a high voltage, it has been assumed that the capacitance levels off as it can be seen in the figure above.

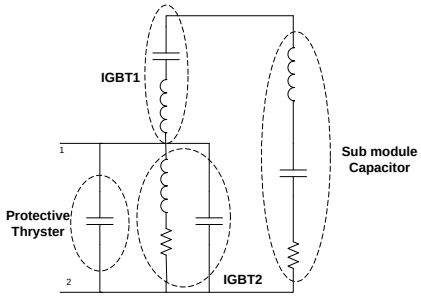

Figure 37 Principle submodule circuit in off-state as implemented in PSCAD

When examining the non-linear characteristic seen above, it becomes clear that at such low voltage levels the capacitance can become significant. When the IGBT is turned on the equivalent circuit can be seen below, where the capacitor has been placed in parallel, in order to represent the capacitance of the IGBT-module when the IGBT is turned on.For transient investigations, the submodule capacitor cannot simply be modelled as an ideal capacitor, as this component besides the capacitance also includes some inductance known as the Equivalent

Modelling IGBT OFF

In this case the IGBT is turned off, hence no current is flowing through, it meaning that the IGBT will constitute a capacitance, however as there inevitably will be some inductance in the IGBT this will have to be modelled as well, which has been done with the incorporation of the inductor.

Modelling IGBT ON

In this case the IGBT is turned on, therefore there will be some conductive losses, but also the inductance of the IGBT will be present. At the same time as it can be seen the figure above a capacitor has been placed in the parallel. This capacitor is applied in order represent the capacitance of the IGBT. When the IGBT is turned on, a small voltage exists across the IGBT due to the small resistance of the IGBT, and when examining the voltage characteristics of the IGBT-capacitance, it is clear that the capacitances of the IGBT are significant at low voltages.

Figure 36 shows the circuit diagram as implemented in PSCAD for the situation in which the submodule is turned on. Here we have also added the protective thyristor as a capacitor for a more uniform picture of the submodule.

Figure shows 37 the circuit diagram is shown for the situation in which the submodule turned off.

From Figure 36 and Figure 37 it can be seen, how a submodule is expressed in terms of passive components. Knowing that there are a number of *N* submodules connected in series, it makes the task of expressing them a bit simpler. All components are added together into two modules, representing all submodules, which are on and one for those which are off, this is done for each multivalve as seen in Figure 38.

As explained earlier, the two multi valves in each phase are direct opposite of each other. Therefore, when calculating the component sizes of the upper multivalve, the results can be used for the lower just by switching the number of on and off submodules and vice versa.

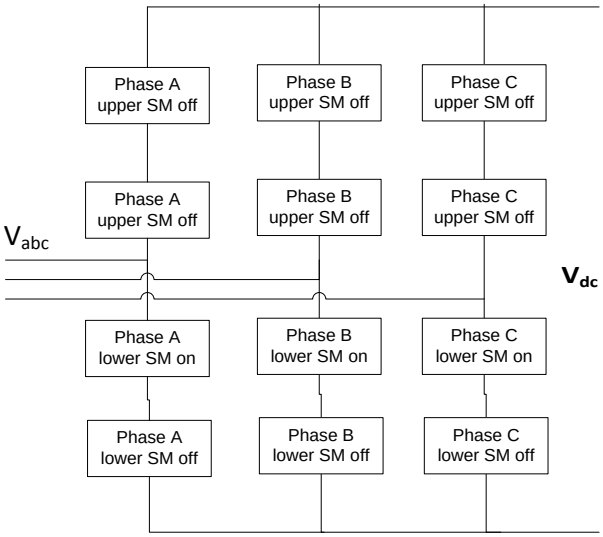

Figure 38 The structure of the simplified passive component model with the 3 phase arms, each of which consists of 2 circuits, one representing the on-state and the other representing the off-state

When summing the capacitors into one equivalent capacitor it is necessary to monitor the arm currents i_{k1} and i_{k2}. While keeping track of which submodule is turned on or off. By integrating the capacitor currents an equation can be written to find the voltage across each individual submodule capacitor:

$$U_{kc,sm}(t) = U_{kc,sm}(t-\Delta t) + \Delta t \frac{1}{6C_{sm}}(i_{k1}(t) + i_{k1}(t-\Delta t) + i_{k1}(t-2\Delta t)) \quad (2.29)$$

where Δt is the simulation time step, using the above equation insures that the model includes capacitor voltage balancing issues and makes the model more adequate for transients simulations compared to the mathematical model.

2.2.3.5 CPU Efficiency

A 1-s period was simulated with a simulation time step of 5us. The simulations were conducted on a Microsoft Windows 7 Professional platform with a 2.67 GHz Intel Core i5 E8400 CPU, 8 GB of RAM running PSCAD version X4. Table 5 tabulates the CPU times for the proposed equivalent converter model, the traditional mathematical model and a full implemented model for different numbers of submodules. As the number of submodules grows, the CPU time of the traditional mathematical model and the full model grows at a much faster rate than that of the proposed model. For 10 submodules per multivalve, the traditional simulation takes more than 6 minutes whereas the proposed model takes 16.43 s, a speedup of 1537% or over 15 times faster. Looking at the growth of the full implementation this would have increased exponentially with an increasing number of submodules.

Table 5 *CPU time*

Number of submodules (N)	*Full implementation [s]*	*Mathematical model [s]*	*Proposed model [s]*
2	38.51	20.21	14.63

4	70.74	27.44	15.62
6	111.39	31.31	16.01
8	170.42	38.07	16.17
10	252.48	40.78	16.43

2.2.3.6 Model verification

A versatile multi-phase MMC prototype has been designed and realized in the laboratory of DTU Powerlab. This reduced-scale IGBT based 5-level voltage source 10kW modular multilevel converter laboratory setup is shown in Figure 39, has been used for the validation of the proposed concepts. It has been extended, accordingly, in order to experimentally test the concepts that are proposed in the section 2.3. The design and development of the MMC prototype is done as described in this and earlier chapter. The Omikron CMC256-6 is used to emulate the grid and various AC faults.

2.2.3.7 DC voltage precharging

Figure 40 shows a time trace for DC-link charging of both DC sources. The precharge contactor is closed at t = 0. After about 0.5 s, the main contractor is closed. When the sum of both sources U_{DC} is above 400 V, the *dq*-controllers take over. The lower graph shows the charge current. Even with a precharge, the current spikes are rather high, though only 80% of the nominal current. Adding all components and most parasitic components in the PSCAD simulation gives a similar behaviour as the measured value. When looking closely at the phase current while precharging note that it is not continues, it will only be conducting when the phase voltages are higher or lower than the pole voltages. Only under this circumstance will the diodes becomes forward biased and conducts current making the converter function as a diode bridge rectifier.A versatile multi-phase MMC prototype has been designed and realized in the laboratory of DTU Powerlab.

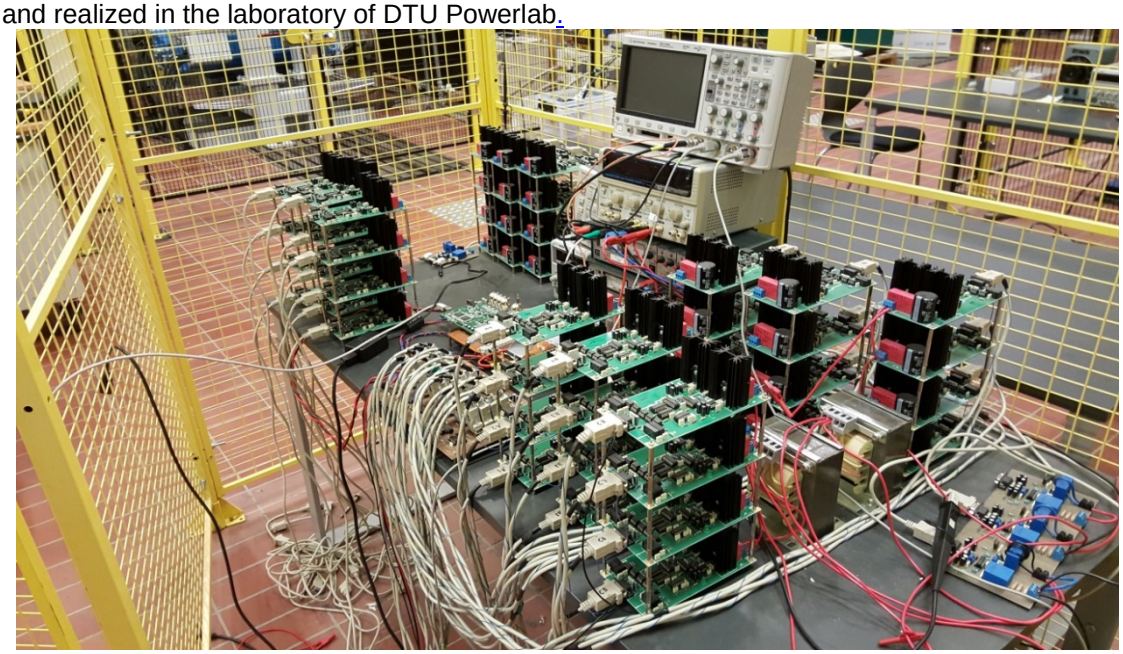

Figure 39 VSC-MMC 10kW laboratory setup

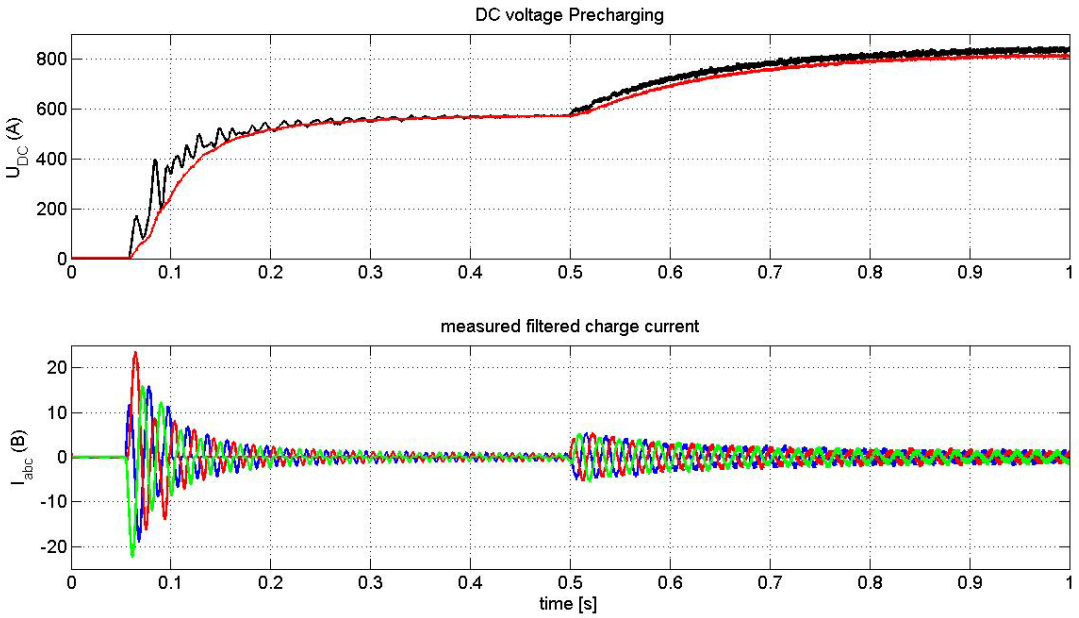

Figure 40 Precharging result, a) DC voltage, b) AC current

2.2.3.8 DC voltage step

This second test scenario shows a change in the DC voltage reference command. In this scenario, the reactive current command is set at 0 pu, while the DC voltage reference steps from 1.0 to 1.1 pu at t = 0.1sec. For this test, the circulating current controller is activated throughout the measurements.

This reference change will directly affect the individual capacitor module voltages, which will now support a higher voltage level. As the DC side is represented by a fixed load, the system will transfer more power after the change to support the desired voltage. As such, the AC and arm currents are expected to increase. The reactive command remains unchanged, thus the i_q component of the AC current should be unaffected. However, the previous simulations have shown that the i_d and i_q components are not perfectly decoupled, so a short transient is expected. As the circulating current controller is active in this simulation, current should remain unaffected, with the possible exception of a short transient.

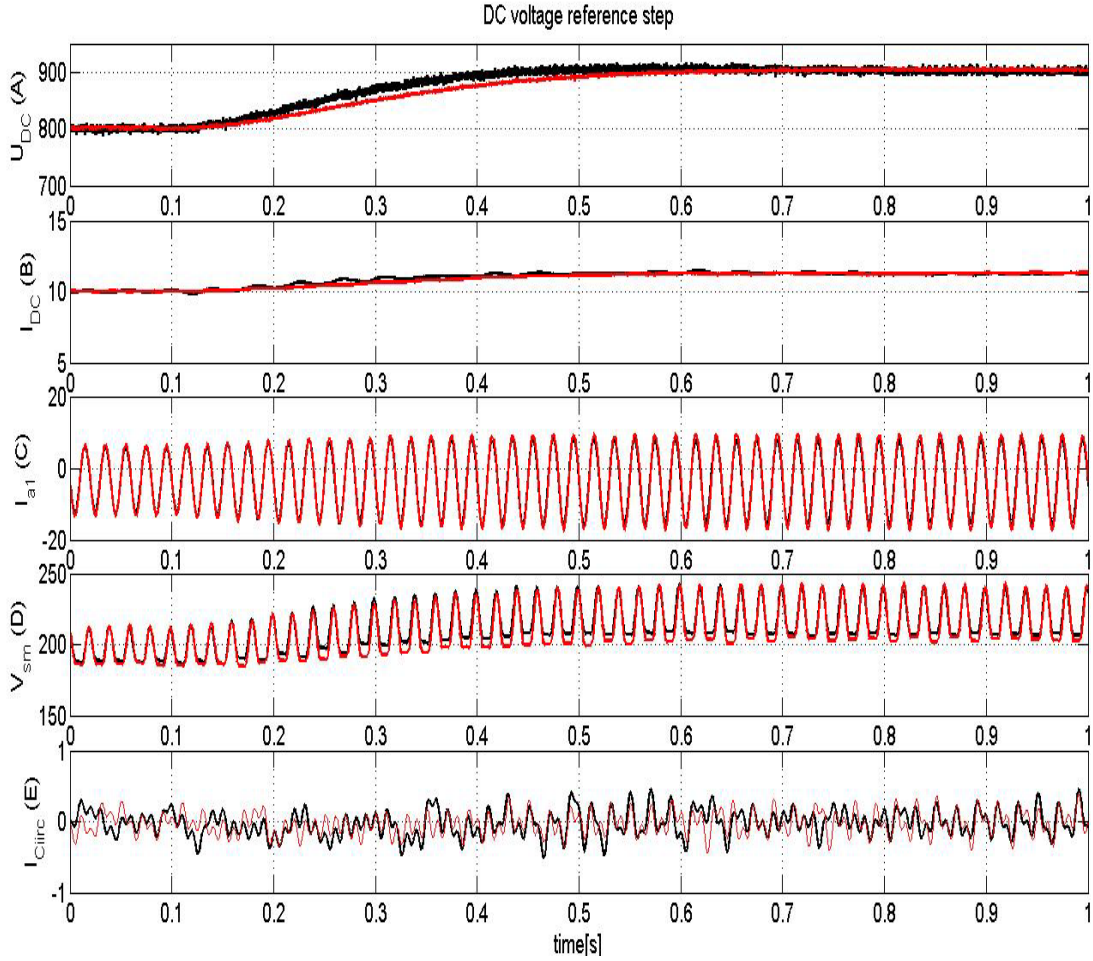

Figure 41 DC voltage step, a) DC voltage, b) DC current, c) arm current, d) submodule voltage, e) circulating current

Figure 41 shows that the model measurements produce fairly equivalent results in this scenario. Some discrepancies are noticeable during the transient, most noticeably on the arm and circulating currents, but their amplitude is limited and they settle quickly with the DC voltage. Figure 41(a) shows that the control operates smoothly and the capacitor voltages settle at the new reference value within approximately 300ms. The higher voltage reference, sustained by larger arm currents does increase the amplitude of voltage fluctuations. The upper arm current of phase A, shown in s Figure 41(c) is also affected by the reference change, as expected since more power is transferred through the converter to the DC side. It also shows short lived differences between the results as the control settles to the final value, but their overall amplitude is a bit less than 10% of the total current or voltage, and their duration are rather short. Looking at Figure 41(f), the fluctuations track the circulating currents. As such, slight offsets in the timing of the reaction of the controllers and the parasitic components between the two results seem to be the most likely the reason for the discrepancies in arm currents.

Here again, most oscillations in the circulating currents are quite small, mostly hidden in the noise caused by controller. There are noticeable oscillations in Figure 41(d) for 200ms after the reference change, as the control adjusts to changing module voltages and arm currents. The controls perform well and limit the circulating current magnitude. Figure 41(d) shows some discrepancies between both results. They are, however, very short lived and most likely caused by small timing differences in the operation of the controllers.

Figure 41(b) shows that the DC current looks very similar however with oscillations on the measured current. There is a small discrepancy, between the simulations as the voltage settles to the new steady-state position. But these differences are small (less than 5% of the total current) here again most likely caused by slight timing differences in the control reactions, parasitic components etc.

2.2.3.9 Power reference step

This test scenario shows a change in the active power reference command. In this scenario, the reactive current command is set at 0 pu, dc voltage reference set at 1 pu, while the active power reference steps from 1.0 to 1.1 pu at *t* = 0.1sec. For this test, the circulating current controller is activated throughout the measurements.

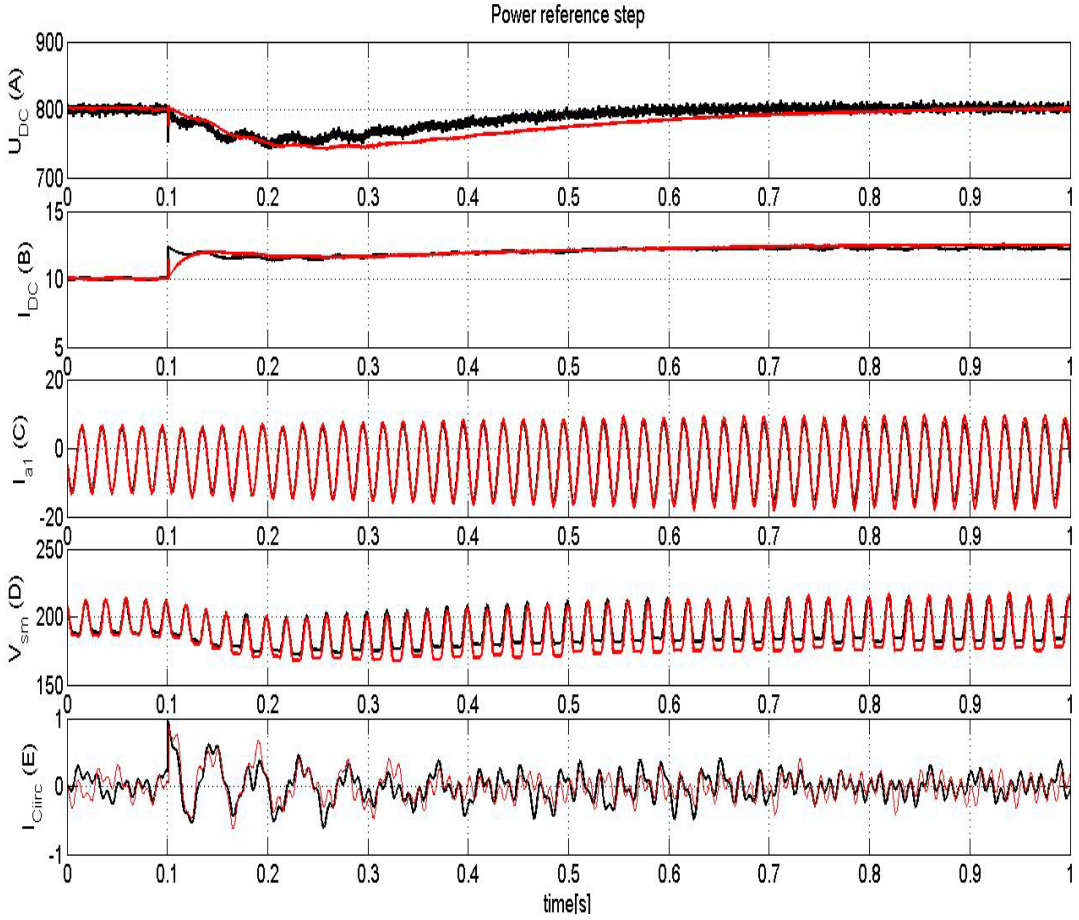

Figure 42 DC voltage step, a) DC voltage, b) DC current, c) arm current, d) submodule voltage, e) circulating current (red-simulations and black-measurements)

This reference change will naturally directly affect the individual capacitor module voltages, which will now support a higher arm current. As such, the AC and arm currents are expected to increase. The reactive command re-mains unchanged, thus the iq component of the AC current should be unaffected. As the circulating current controller is active in this simulation, cur-rent should remain unaffected, with the possible exception of a short transient.

From the responses plot in Figure 42, the system works stably with the change in active power as well. Due to the change in power, the DC voltage is naturally affected (Figure 42(a)), both results seem to behave similarly with a reduction of around 5% in DC voltage during the transient. However the measured current again has an oscillation of ≈125Hz. It should be mentioned that this frequency appears whenever the control is changing. Hence it could be that this is coming from the physical control and not present when using simulation tools. Nonetheless, the control seems to be a bit faster reaching steady state before the simplified model simulation. The arm current behaves in both cases exactly as expected with increase in the peak current and a larger DC offset Figure 42(c). The submodule voltage (Figure 42(d)) behaves similarly to the DC voltage step with an increase in the ripple due to the increase in arm current.

2.2.4 MT-HVDC

In the four-terminal VSC-HVDC transmission model shown in Figure 43, two of the VSC-HVDC terminals (i.e. VSC3 and VSC4) are set to be operated in constant power control mode (meaning no indifferent of the DC voltage) whereas the other two VSC-HVDC terminals participate in the dc voltage droop control.

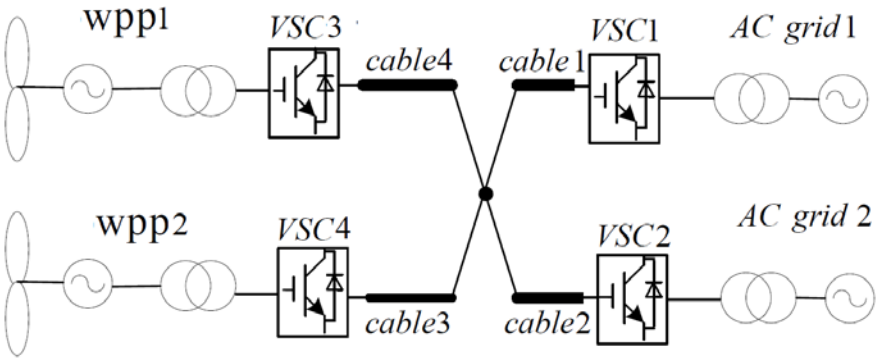

Figure 43 MTDC topology used for simulations

Table 6 MTDC parameter for EMTDC simulations

Station	*Nominal voltage*	*Nominal Power*	*Operating Power*	*Cable1*	*Cable2*	*Cable3*	*Cable4*
VSC1	±320kV	1000MW	600MW	100km	55km	78km	50km
VSC2	±320kV	1000MW	Slack				
VSC3	±320kV	200MW	-500MW				
VSC4	±320kV	300MW	-350MW				

Now, let us consider an arbitrary power flow schedule for the hypothetical dc grid. In Table 4, the desired power flow pattern is given. In the power flow schedule of Table 6 terminals 3, 4 are desired to inject a power of -500MW, -350MW respectively into the dc grid. The minus signs show that power is taken away from the dc grid to ac grid via a VSC-HVDC terminal, implying inverter mode of operation. Terminals with positive power injection are in rectifier mode of operation. The “slack” in the *Operating Power* column of Table 6 shows that VSC2 will try to maintain the power balance with no regard to its own power level. If we do not give any regard to the dc line voltage drops and the associated line losses, VSC2 will be expected to inject a power of -350MW into the dc grid. Hence the dc voltage references will be assigned to 640 kV. The power and dc voltage references to be used in the simulation are listed in Table 7.

Table 7 MTDC parameter for EMTDC simulations

Station	U_{DC}^{*}	P^{*}
VSC1	640 kV	600MW
VSC2	640 kV	250MW
VSC3	640 kV	-500MW
VSC4	640 kV	-350MW

VSC3 and 4, which are constant power terminals, do not need dc voltage references although these were included in Table 7 for the sake of completeness. In order to better understand the influence of dc line resistance on power flow and the reaction of the system to power changes a simulation case will be considered for the study specified in Figure 44. It is clear to see that before the power transmission is initiated the converters are only delivering the power needed for the losses to maintain the DC voltage. When the power order is applied an increase in all the stations occurs to reach their reference values. This will cause a short increase in the DC voltage which quickly will be seen by the controller and adjusted for. Furthermore a clear difference is seen between the droop control and the constant power controlled stations due to the voltage drops in the cables. When the station is droop control it will adjust it control reference signals will be adjusted to ensure the power order is meet while the DC voltage reference is meet as well. However in the constant power controlled stations the voltage drop across the cable is not considered leading to a higher DC voltage at the terminals.

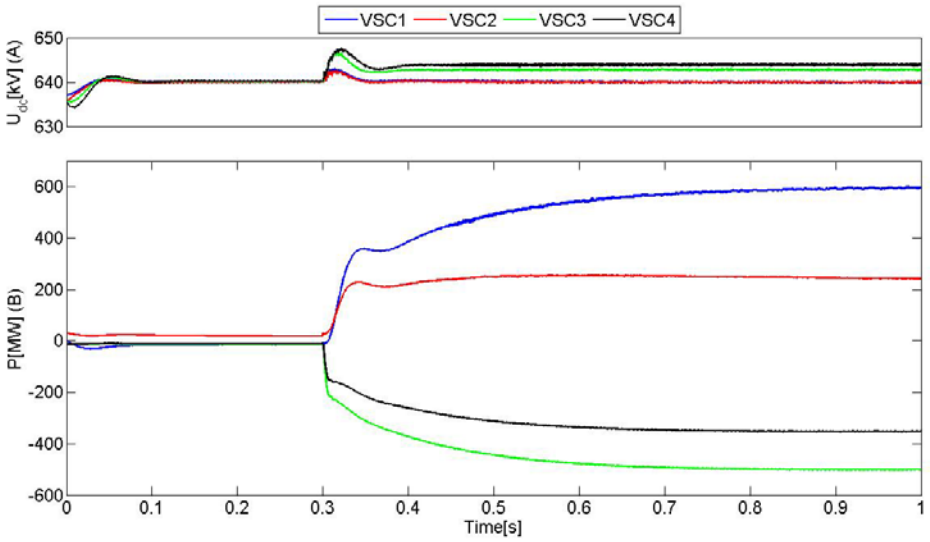

Figure 44 Power transfer startup

At this stage, the functionality of the droop control in establishing a desired power flow to the previously described MTDC grid is demonstrated. Among them, VSC 1 and 2 are selected to operate as pure droop-controlled stations while VSC 3 and 4 have been set, to operate in constant-power controlled. The gain values of the PI controller in the power droop controller are chosen appropriately to provide a setting time of approximately 1s for a power-step reference. The droop mechanism is chosen to be the one in ensuring a linear relation between voltage and power change. For the purpose of this example, the onshore stations are connected to strong grids, which are thus represented by 400 kV voltage sources.

2.2.5 DC fault

To assess the control on multi-terminal HVDC systems, a trip of VSC3 of the four-terminal topology presented in Figure 43 is tested. Substations connected to the mainland are droop controlled, others are power controlled again. Substation VSC3 is disconnected from the DC grid at 0.5 s and then the voltage is restored at 0.55 s by assigning a new power set points coming from the secondary control. The voltage and power injected at each terminal are shown in Figure 45.

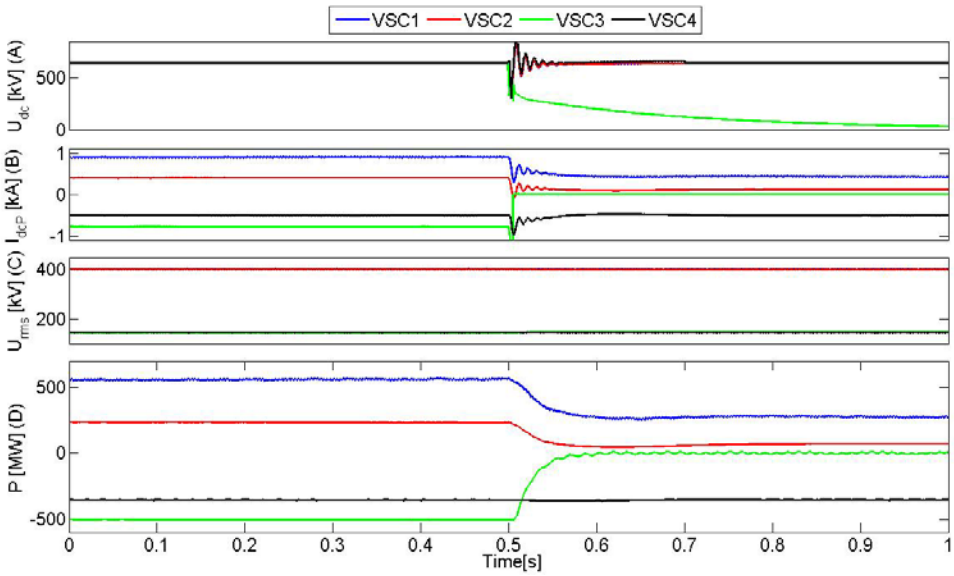

Figure 45 Trip of VSC3, a) DC voltage, b) DC current, c) AC voltage in rms d) converter station active power

In this simulation detailed converter models are used, cables are represented by wideband models which have been defined by earlier. The base power for this simulation has been chosen at the highest converter power rating (600MW) and the base voltage at the nominal value (640kV). An initial transient in the DC voltage are visible because of the sudden loss of the VSC3. When substation VSC3 trips the voltage decreases because there is a lack of power injected in the DC grid. Thanks to droop control on substations connected to the AC grid, the power

flow equilibrium is getting back, however the voltage level will oscillate for a short time while the remaining converter currents settles. As expected, the power adjustments of substations VSC1 and VSC2 are not equal because they don't have same droop parameter. During the transient there are a lot of oscillations which can come from resonances between cable and DC substation filter. The voltage readjustment is realized by setting actual power outputs as power references. Due to the ramp rate limiter there is very limited excitation of resonances and then the voltage level returns back smoothly towards its original value. However the resonance and the peak of the DC voltage are influenced by the breaker time delay. When increasing the breaker time delay and thereby the fault clearing time it noted that the DC voltage will initially reach equilibrium at a lower voltage before returning to the original voltage level Figure 46(a). The resonant frequency and damping time are naturally not affected in any notable way. However due to the longer delay the fault current spike, consequently the DC current drastically increased. This is caused by the discharging of the stored energy in the DC grid, resulting accordingly in an increase in first voltage spike in the DC voltage.

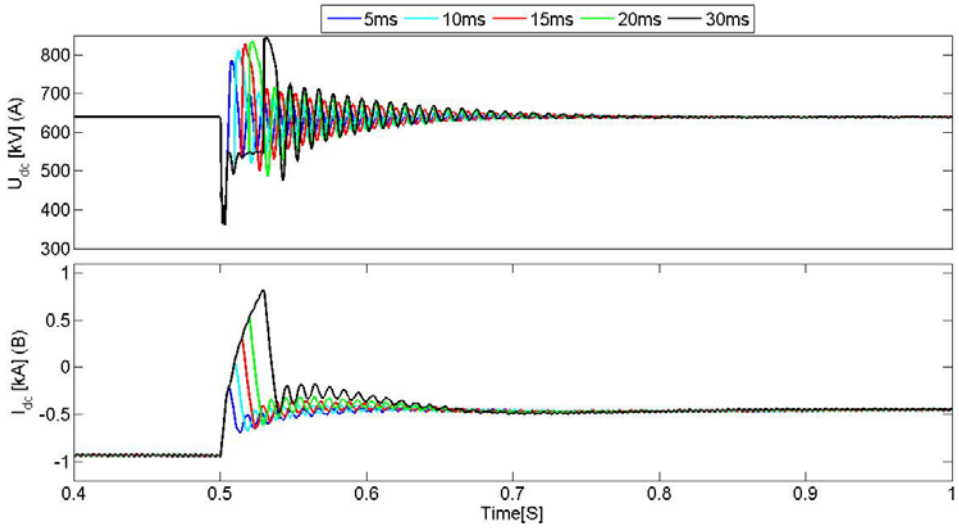

Figure 46 VSC1 response to an increase DC breaker time delay, a) DC voltage, b) DC current

The easiest way to reduce the oscillations would be to increase the number or size of the surge arrestor Figure 47. This will not reduce the first much since there is too much energy and an unreasonable amount of surge arrestors would be needed. Nonetheless it is clear to see that the oscillations are damped much faster than previously.

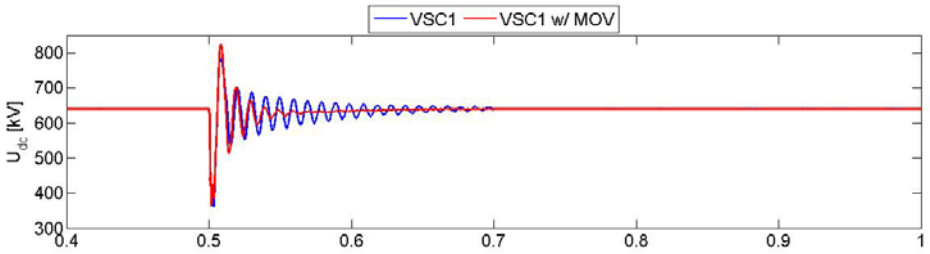

Figure 47 Increasing number of surge arrestor

2.2.6 AC fault

To perform AC fault simulations, the exact same network as described in the previous section is used, however no DC fault is applied instead an 100ms one phase AC fault to ground is applied. The AC one phase onshore fault was applied at 0.6 seconds at VSC1 as shown in, the DC voltage of all stations decreased a bit and starts to oscillate due to the sudden drop in power import at the onshore station VSC1 Figure 48. However due to the droop control VSC2 will quickly increase the import of active power to stabilize the DC voltage. It is clear that even before the fault is cleared the DC oscillations are already being damped and the voltage is kept relatively stable at around 640kV. Both offshore converters will continue to export power since they are in constant power

mode. Some natural variation will happen due to the changes in DC voltage nevertheless both converters succeed in maintaining their power output. As soon as the fault at VSC1 is cleared the entire system returns to its previous operation condition and the system is quickly stable again.

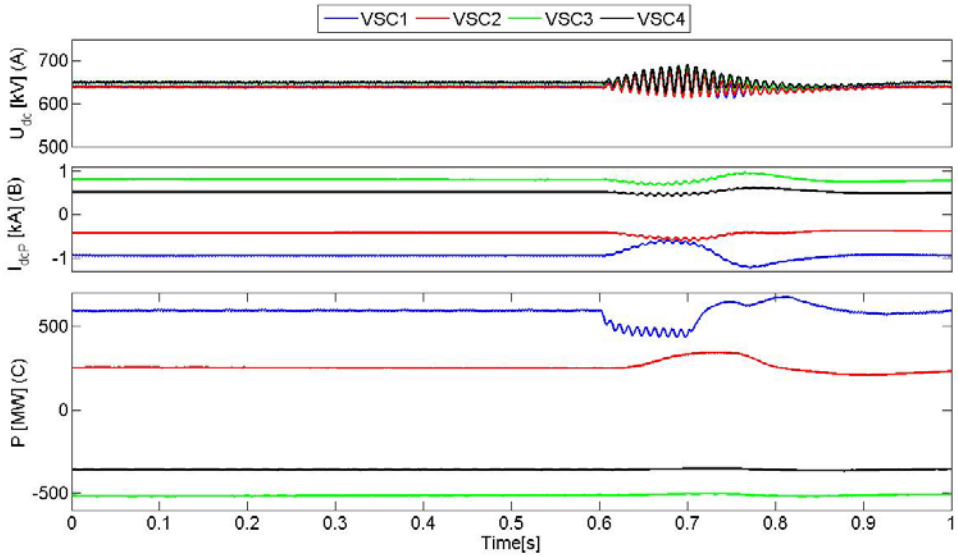

Figure 48 AC fault at VSC1, a) DC voltage, b) DC current, c) Active power

To investigate the effect of the droop control on the fault clearance of VSC1 the simulation is redone while changing the droop percentage Figure 49. It becomes truly clear that the droop percentage has little effect on during the fault, if one looks closely it is possible to notice that the influence on DC side is reduced, however marginally compared to large change that is made. This is clearly due to that the converter is not operating in normal condition. This is a result of decreased controllability of the AC voltage and subsequently the reactive current is prioritized during such faults.

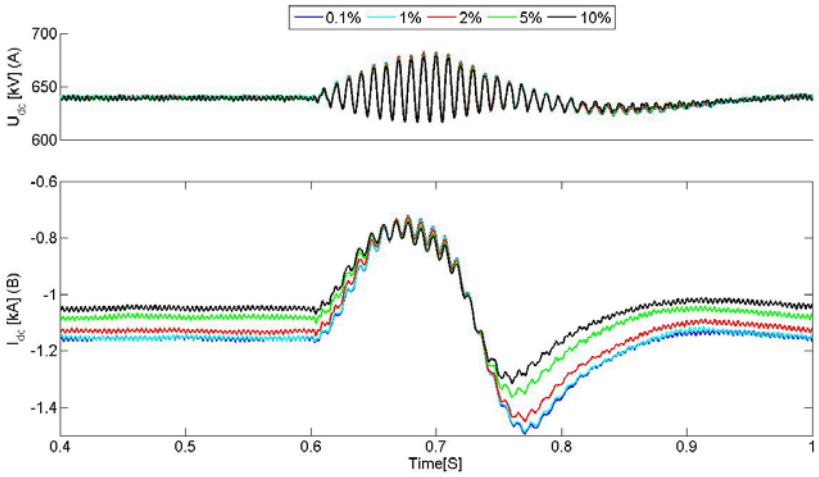

Figure 49 AC fault at VSC1, varying droop percentage, a) DC voltage, b) DC current

The second test is done for the current controller speed, where 1 is nominal speed used speed for the previous simulation Figure 50. During the pole to ground fault at the AC side the converter VSC1 behaves similarly in all cases. Nevertheless the behaviour starts to differ when VSC1 starts to regain full control and tries to return to the initial state. Once the controller is slowed down a faster stabilizing time is achieved, on the other hand it takes over 1.2s to return to the initial operating voltage. The reason for this is the reduced PI controller gain which will become slow once the DC voltage error becomes relatively small. Increasing the speed will give a fast return to 640kV although larger overshoot will occur as a result. If the overshoot becomes large enough it will have a direct impact on the DC voltage given an increased voltage drop.

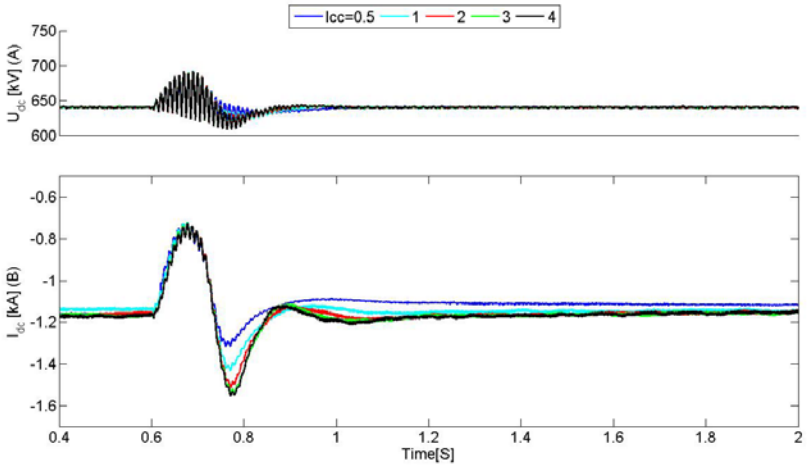

Figure 50 AC fault at VSC1, varying current controller speed, a) DC voltage, b) DC current

2.3 Summary

The dc-network dynamics of VSC-HVDC systems were thoroughly investigated in two-terminal connections and new perspectives were introduced to the control of VSC-MTDC grids.

Regarding the stability investigation, two-terminal VSC-HVDC system was modelled as a SISO feedback system, where the VSC-transfer function $F(s)$ and the dc-grid transfer function $G(s)$ were defined and derived. Two different methods were then utilized to assess the closed-loop stability of the complete system by observing the separate frequency domain behaviour of the $F(s)$ and $G(s)$. The *Passivity* analysis focused on the related passivity properties of the two transfer functions at critical frequencies. This tool showed satisfactory results as long as both transfer functions were stable. However, once the latter was not valid, the passivity approach could no longer be used. The *Net-damping criterion* approach did not have this complication and proved to be a superior tool in analyzing the stability of the system and deriving useful results, based on the individual net-damping of $F(s)$ and $G(s)$. It was also found that the absolute amount of net-damping in the system measured at the frequency where the Nyquist plot crosses the real axis closest to -1, is directly related to the existence of poorly-damped dominant poles and their damping factor. A net-damping approaching zero at that frequency indicates the existence of poorly-damped poles with constantly decreasing damping factor.

The analysis of the previous systems was also observed from an analytical-pole description. The *SMT* analytical method was developed and presented in conjunction with the already known *LR* method, which had nevertheless never been implemented in the analysis of power systems or control related processes. A benefit of the *SMT* focused on the fact that is not iterative, meaning that the form and complexity of the final analytical eigenvalue expressions is known from the beginning, in contrast to the iterative *LR* where each additional iteration theoretically improves the accuracy but dramatically worsens the compactness of the expressions. Both methods showed impressive results in approximating the actual values of the VSC-HVDC model, but the *SMT* showed a consistent increase in accuracy compared to the *LR*.

In the area of Multiterminal HVDC, focus was given on the development of droop-based controllers. In the beginning, a controller was proposed for use in cases where a VSC station required to maintain its designated power flow after unexpected contingencies in the grid, such as the loss of a station following a dc-side fault, while maintaining voltage-droop characteristics during transients in the grid. The concept was tested in a five-terminal MTDC, where the performance of the controller was favourably compared to that of a conventional PI-based power controller. A second droop-controller variation was proposed for use in MTDC grids where a droop-controlled station requires a very high droop constant, meaning that it should maintain its power flow almost constant under all grid conditions, but still provide direct-voltage support as a conventional droop-controlled station would during grid contingencies. The proposed controller was tested in a four-terminal MTDC and compared to the performance of conventional droop-controllers, with the same droop constants being used for the same stations in both scenarios. It was shown that following a rapid change of power and voltage setpoints, the two controllers had no difference in steady-state performance (as desired), but the proposed control provided a smooth power and direct-voltage reaction from the stations that used it, compared to the conventional control that even exhibited poorly-damped oscillations.

Many properties of the MMC have been illustrated and explained. Theoretical evaluations and simulation results have been related to examine the similarity. It is desired that the simulation model mirrors the properties of a real life converter, to make the analysis valid also in that context. In order to study various dynamic behaviours of HVDC transmission systems, a dynamic simulation model is developed. Furthermore, since the transient behaviour was very important in this work, a high frequent model had to be developed for the main components. This includes wind turbine, collector network, transformers, VSCs, cables and other major components of the system. Nevertheless the main two components affecting the simulation time negatively (cables and converter) where modelled in a simplified manner which preserved their functionality and dynamic performance. The converter model was verified against a 5-level VSC-MMC laboratory construction. The MMC converter, together with its control and protection, was designed and constructed during this project.

The performance of HVDC transmission was analysed for multiple types of connections. The system was analysed for point-2-point MMC interconnector power transmission. Simulation showed how even with a low number of submodules the converter was able to continue operating with the loss of submodules.

Transients in HVDC connected WPPs was analysed and compared with HVAC. A method was proposed to minimize the inrush currents and damping resonances using the offshore converter. The importance of reactive power support in weak offshore grids was pointed out and a chopper was proposed to further protect the system. The related work supports the derivation of requirement specifications of components in a MTDC network by means of simulations and calculations. It demonstrated the ability to control complex multi-terminal HVDC topologies in case of severe power variations occurring in the DC grid. It contributes to a deeper understanding of the transient behaviour of the MTDC grid during a pole-to-ground fault on both the AC and DC sides and analyses the influencing parameters. The modelling and implementation of the network components in a MTDC network for the simulation of transient voltages and currents were described first, as well as the required methods for the transient simulations.

3. Control and stability analysis of OWPP and HVDC grids

3.1 Interaction between offshore HVDC grids and AC power systems

This section presents the results regarding the interactions between HVDC grids, onshore AC power systems and OWPPs. In particular, the implications for power system services and stability are discussed, starting with active power balance control (AC frequency and DC voltage), continuing with AC voltage control and concluding with small-signal stability.

3.1.1 Frequency and DC voltage control

Contribution of OWPPs

Participation of OWPPs to the power balance control in AC-DC grids implies upgrades to their controls, so that they can respond to AC frequency and/or DC voltage variations across the network. This section describes how the service can be implemented on modern OWPPs based on Type 4 WTs. Furthermore, sample results are shown in order to visualise performance and limitations in providing such features. The reader is referred to [Zeni, 2015a] and [Zeni, 2012] for more details.

Implementation of frequency and DC voltage control on OWPPs

Assuming that an OWPP has to be seen as a lumped unit (like any other power station), frequency control and DC voltage control service must be delivered at the OWPP point of connection as a lumped, coordinated response. Hence, the services can be implemented at plant control level as depicted in Figure 51.

The frequency control is derived directly from the frequency f, which can be sensed offshore (controlled by HVDC converter) or communicated from onshore – see next sections. The nature of the frequency control can be inertial and/or proportional (droop). The frequency control signal is then processed by the active power controller (PI), but it can also be fed forward (through flag F_{FFf}) to the dispatcher – here represented by the rightmost lead-lag block (time delay). On the other hand, the DC voltage control signal is assumed to be directly input as power reference and must be fed forward to the dispatcher, so as to avoid delays due to the power controller – the reasons for this are explained below. The generated signal P_{refWTG} is passed to the WTs.

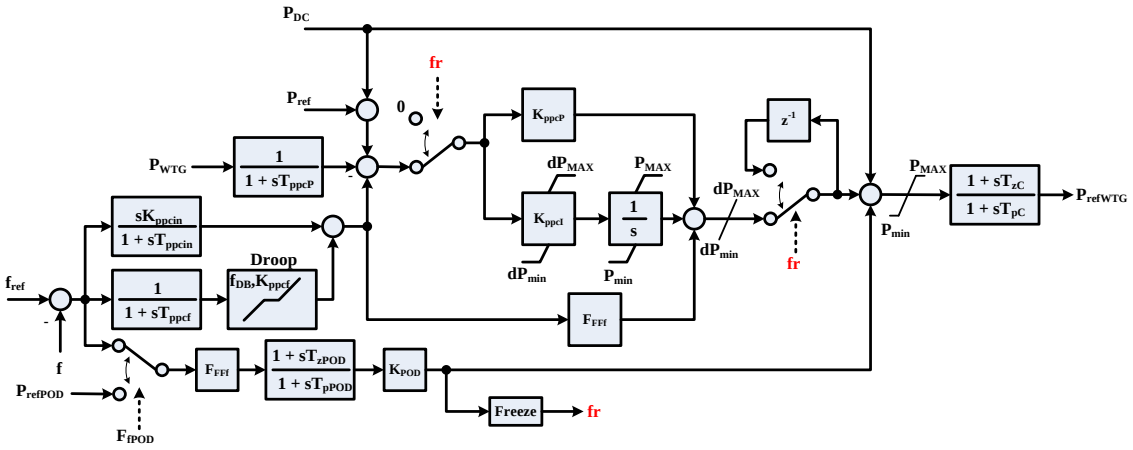

Figure 51 Wind power plant active power control [Zeni, 2015a].

Coordinated frequency control vs communication in point-to-point connection

When a point-to-point HVDC connected OWPP is called to deliver frequency control to an onshore terminal, this can be achieved by communicating the onshore frequency directly to the OWPP or by a coordinated scheme where the onshore HVDC converter controls the DC voltage proportionally to the onshore frequency and the offshore HVDC converter controls offshore frequency according to the DC voltage so as to achieve mirroring of onshore frequency in the offshore network – see [Zeni, 2015a] and [Zeni, 2012] for details. A comparison of the two alternatives highlighted that in such a scenario, and for typical onshore frequency variation time constants, the

communication-based scheme can be used without significantly affecting the performance, as depicted in Figure 52. Both inertial and droop frequency control are tested simultaneously. Case “Base” is without frequency control, case “1B” makes use of communication with 100 ms delay and case “2B” represents the coordinated scheme described above. The active power delivered to the onshore terminal is plotted.

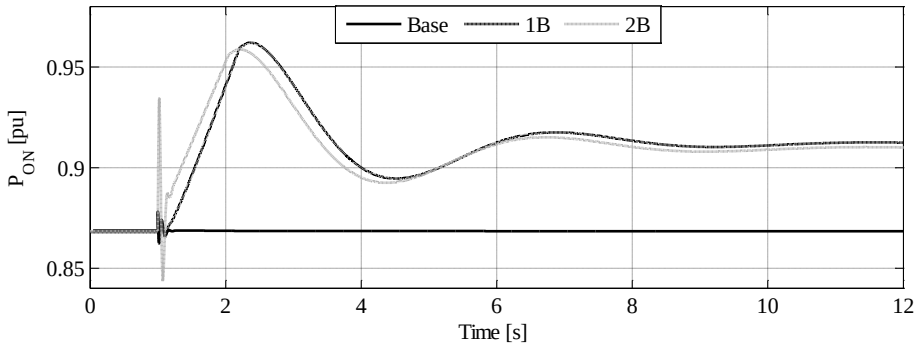

Figure 52 Inertial and droop response of HVDC-connected OWPP: comparison between scheme without (Base), with communication-based (1B) and coordinated (2B) frequency control (Zeni, Margaris, Hansen, Sørensen, & Kjær, 2012).

In terms of power delivered to the onshore grid, the two schemes do not differ significantly, also considering that (i) a large value for the communication delay has been assumed and (ii) the onshore grid parameters have been set so as to have a quite low time constant. It is hence recommended to use communication in such a scenario.

Limitations of frequency control provision from OWPP

Generally, frequency control is related to time constants within which OWPPs can in principle act satisfyingly, i.e. several seconds. However, some settings such as ramp-rates might pose a limit to the delivery of frequency control. Ramp-rate limiters (dP_{min} and dP_{MAX} in Figure 51) are used so as to protect the WT system – mainly its mechanical part – from excessive stress. As depicted in Figure 53, where the OWPP’s active power reference is compared to its ramp-rate-limited value are plotted, when inertial control or fast droop response is needed, ramp-rate limiters may limit the initial frequency response. A ramp-rate of 0.1 pu/s has been assumed in the figure. This is an especially important issue as the share of wind power grows and frequency control requirements become more dynamically demanding.

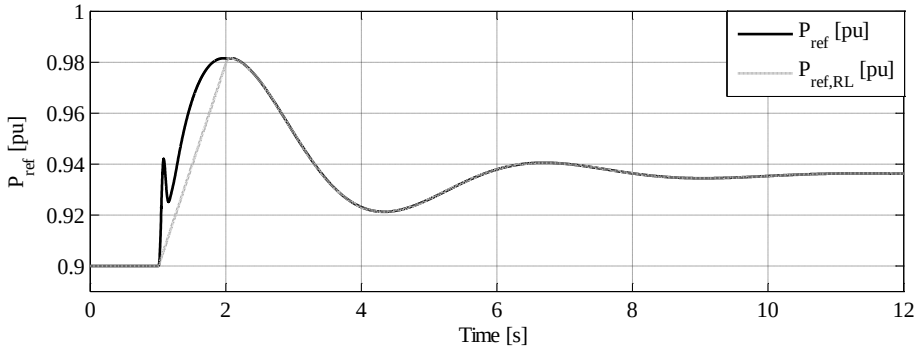

Figure 53 Effect of ramp-rate limiters on active power delivered by OWPP (Zeni, Margaris, Hansen, Sørensen, & Kjær, 2012).

Other factors which limit the active participation of current OWPPs to the frequency control service are:

- Poor economic incentive to deliver the service due to favourable energy price as compared to regulation power price.
- Insufficient accuracy of wind speed prediction to guarantee safe estimation of available regulation power and energy.

Limitations of DC voltage control provision from OWPPs

The limitations for delivery of DC voltage control from OWPPs are much more restrictive than for frequency control. This is due to the fact that HVDC grids store a quantity of energy which is 10-100 times less than in usual AC grids,

because of the limited energy storage of DC capacitance as compared to rotating masses associated with synchronous generators.

The above means that delivery of fast DC voltage control is way more challenging than frequency control. This is illustrated by the following example. The three-terminal HVDC grid is simulated, where converter HVDC 1 controls power, while HVDC 2 controls DC voltage in droop mode. So does the WPP, controlling P_{OFF} as a droop function of the DC voltage. The control signal $P_{DC} = K_{DC}\Delta V_{DC,OFF}$, is passed to the WPP controller according to Figure 51, and the WTs are assumed to be instantaneously controlled power sources, with bandwidth equal to that of their current controller. Two cases are simulated:

- Case 1: $K_{DC} = 4$ for HVDC 2 and $K_{DC} = 1$ for the WPP.
- Case 2: $K_{DC} = 1$ for HVDC 2 and $K_{DC} = 4$ for the WPP.

In both cases a power step in HVDC 1 and its subsequent outage are simulated. The results are plotted in Figure 54.

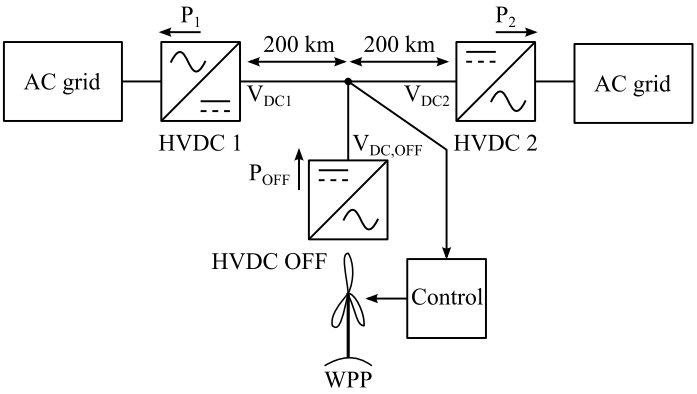

Figure 54 Simulated three-terminal HVDC network [Zeni, 2015a].

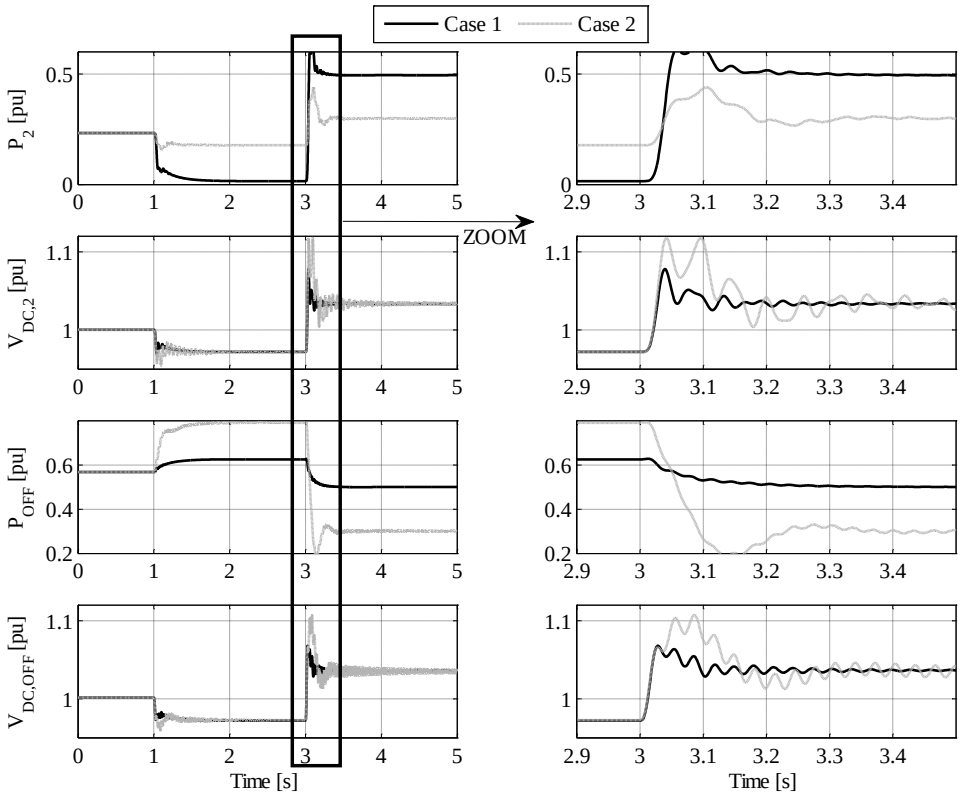

Figure 55 Results for OWPP contribution to DC voltage control [Zeni, 2014].

As can be seen, the disturbance has much more disruptive effects when the OWPP is required to play a major role in the DC voltage control (Case 2). It must be noted that very ideal conditions were assumed, i.e. no communication delays and ideal behaviour of the WTs.

The above illustrates that DC voltage control from OWPPs is indeed a challenging task and the proposed way to deliver it at a plant level may not be the most effective one. Distributed controllers nearer to the converters may be necessary to provide the required dynamic performance. This is true particularly when the share of OWPP generation is relevant as compared to the total size of the DC grid, but this may not be an unlikely scenario if large offshore grids evacuating wind power will become reality.

Coordination between HVDC and onshore power system

In HVDC links connecting offshore wind farms to onshore grids, the onshore HVDC converter controls dc link voltage, while the offshore side converter determines frequency and ac voltage for the offshore wind farm grid. If the offshore wind farm is going to be involved in frequency regulation of the onshore grid, then auxiliary controllers are added to both the onshore and offshore side HVDC converters. Thus, the onshore converter changes dc link voltage when frequency deviation occurs in the onshore grid. The offshore HVDC converter will then change offshore grid frequency according to the change in dc link voltage. Alternatively, a communication system can be used to directly transfer onshore frequency signal to the offshore HVDC converter controller. With this method, the onshore side HVDC converter controls dc link voltage, while the offshore side HVDC converter controller changes the offshore frequency (therefore, wind farm output) based on onshore frequency deviation. A further alternative is for the onshore frequency signal to be directly communicated to the wind farm, which will act accordingly, modulating its active power output. As shown in the previous section, from the perspective of the ac grid, the control methods described above (using dc voltage change or communication system as a signal medium) produce the same result. As the wind farm is connected to only one grid, all the power produced by the wind farm flows into that grid, and any power flow change at the wind farm terminal is also reflected in the power flowing into the ac grid. However, the two control methods have different results if the wind farm is connected to ac grids through an MTDC grid.

MTDC

DC voltage droop control is considered to be the most appropriate converter control strategy for MTDC grids. With this control method, two or more terminals with droop characteristics regulate dc voltage, and the involved terminals share power imbalances in the dc grid according to their droop settings. If an offshore wind farm is connected at one of the MTDC terminals, then that terminal controls the wind farm's voltage and frequency (similar to the case of HVDC) allowing the wind farm to inject all its power production into the dc grid. For the offshore wind farm to participate in onshore frequency regulation, the converter control structure of the offshore wind farm terminal and the onshore terminal(s) receiving the frequency support are modified. By using both frequency and dc voltage droop control, changes in onshore grid frequency are counteracted by changes in power flow into/out of the grid. This causes a power imbalance in the dc grid leading to change in dc grid voltage. MTDC terminals operating in dc voltage droop control mode and the offshore wind farm terminal change their power flow to remove dc grid power imbalance and regulate dc voltage. The onshore grid gets frequency control support from the dc grid. However, the actual power support comes both from the offshore wind farm and the other ac grids connected to the dc grid whose terminals are operated in dc voltage droop control mode.

Proposed coordinated converter control

Using communication system to send ac grid frequency directly to an offshore wind farm MTDC terminal converter control is not a feasible control option because the change in wind farm power output would be considered as a dc grid power imbalance, and all terminals operating in dc voltage droop would react to remove the imbalance. Therefore, a coordinated MTDC converter control is proposed where frequency and dc voltage droop is used at an onshore terminal and, at the same time, ac grid frequency is communicated to the offshore converter terminal to modulate offshore wind farm power output. Figure 56 shows control block diagram for onshore and offshore converters.

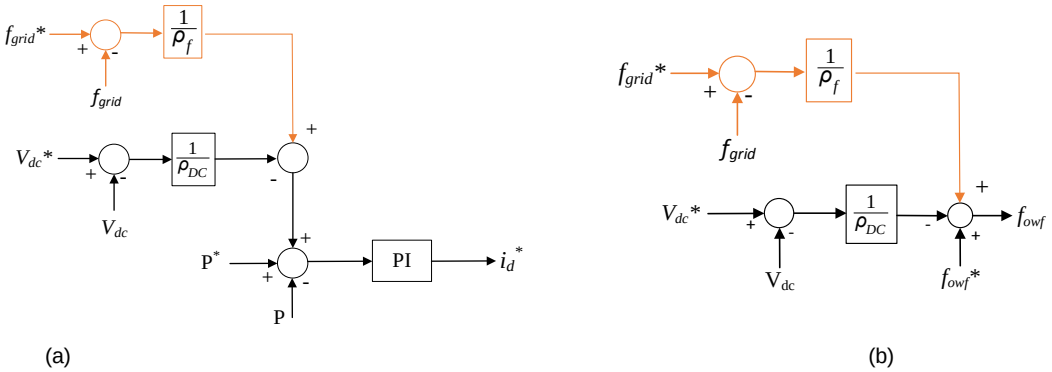

(a) (b)

Figure 56 Auxiliary MTDC converter controllers on (a) onshore grid side and (b) offshore wind farm side.

With the proposed coordinated converter control strategy, dc grid power imbalance is reduced as the power change in wind farm's output would compensate the power demand change at the onshore grid's terminal converter. This implies that frequency control support from offshore wind farm is maximized and frequency disturbance in other ac grids connected to MTDC is reduced.

The following section present different case studies that demonstrate the effectiveness and limitations of the control strategy.

Study case description

A test power system that has three terminal VSC-MTDC grid connected to an offshore wind farm and two asynchronous grid is used for the case studies (Figure 57). Wind turbines and internal collection grid of the offshore wind farm are not modelled in detail. Instead, a stiff bus was used behind the offshore terminal converter to represent the wind farm. This is considered sufficient for the study because the focus is on coordination of the MTDC converter controllers. DIgSILENT *PowerFactory* was used for the simulation studies. At initial steady state conditions, the wind farm was producing 600 MW. Grid #1 imports 400 MW while Grid #2 imports the remaining power.

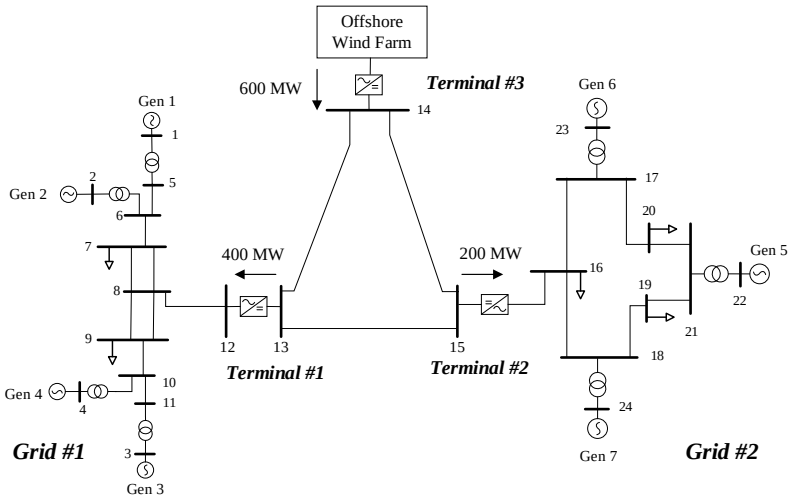

Figure 57 Study system.

Four different cases were studied, and were compared with each other. Table 8 lists types of converter controls used at each MTDC terminal for the different cases. Loss of load in Grid #1 and Grid #2 were simulated to create a frequency disturbance in the grids and study the performance of the proposed coordinated control strategy.

Table 8 List of study cases.

	Terminal #1	Terminal #2	Terminal #3
Case 1	Freq + Vdc droop	Vdc droop	Vdc as freq. change signal
Case 2	Freq + Vdc droop	Vdc droop	Vdc droop + Frequency signal via communication

Case 3	Freq + Vdc droop	Freq + Vdc droop	Vdc as freq. change signal
Case 4	Freq + Vdc droop	Freq + Vdc droop	Vdc droop + Frequency signal via communication

Case 1 and 2: single grid receiving frequency support

Loss of load in Grid 1

Loss of load in Grid #1 causes frequency disturbance in the grid. In order to remove the power imbalance (control frequency), the governors make the synchronous generators reduce their power output. At the same time, Terminal #1 converter controller reduces the power flowing from the dc grid into Grid #1.This leads to power imbalance in the dc grid and increase in dc voltage level, which is picked up by both Terminal #2 and #3. Both terminals will try to regulate the dc voltage by changing converter power flows. Terminal #2 takes in more power from the dc grid, while Terminals #3 injects less power into the dc grid. Figure 58 shows Grid #1 and Grid #2 frequencies in Case 1 and Case 2.

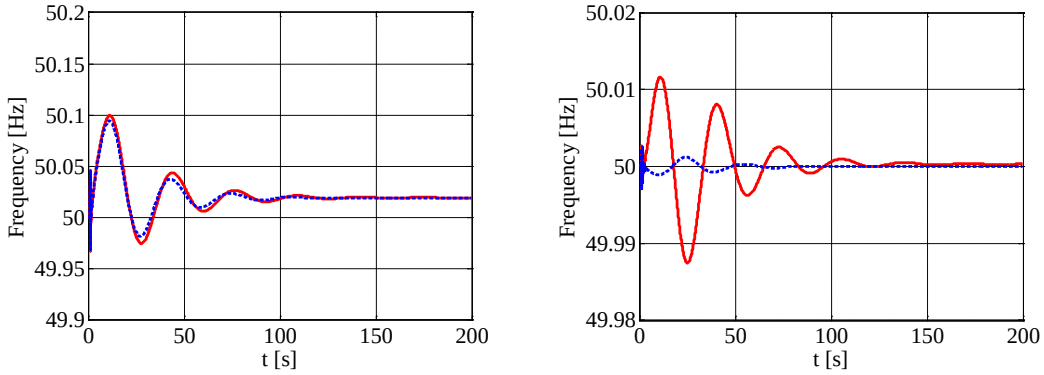

(a) Grid 1 Frequency (b) Grid 2 Frequency

Figure 58 Frequency in Grid #1 and #2 for Case 1(solid line) and Case 2 (dashed line) for loss of load in Grid #1.

The frequency disturbance in Grid #1, where the load loss occurs, is similar in both cases. However, the disturbance in Grid #2 is significantly less in Case 2 than in Case 1. This is because in Case 1 the frequency support to Grid #1 comes not only from the wind farm but also Grid#2; which participates in dc grid voltage regulation and indirectly shares the frequency support duty according to its dc voltage droop setting. On the other hand, in Case 2, by communicating Grid #1 frequency directly to Terminal #3, the reduction in wind farm's power output is higher compared to Case 1. Thus, the wind farm contributes most of the power needed to regulate the frequency in Grid #1 and the power flow at Terminal #2 remains almost unchanged. This is reflected in Grid #2 frequency for Case 2 in Figure 60(b). The power output from the wind farm for Case 1 and Case 2 is shown in Figure 59.

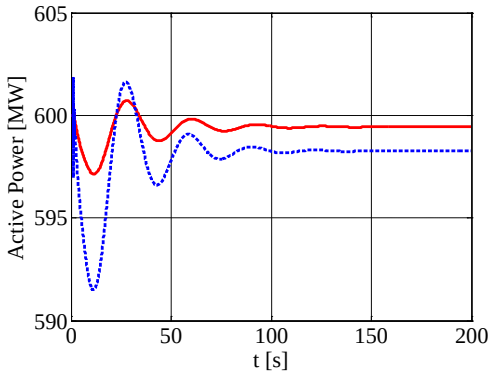

Figure 59 Wind farm power output in Case 1(solid line) and Case 2 (dashed line) for loss of load in Grid #1.

Loss of load in Grid 2

Since MTDC converter at Terminal #2 is operating only in dc voltage droop control mode in Case 1 and Case 2, neither the wind farm nor Grid #1 participate in frequency control of Grid #2. Only governors of the synchronous

generators regulate any frequency disturbance in the grid. Figure 60 presents frequency in Grid #1 and Grid #2 for a loss of load in Grid #2 in both Case 1 and Case 2.

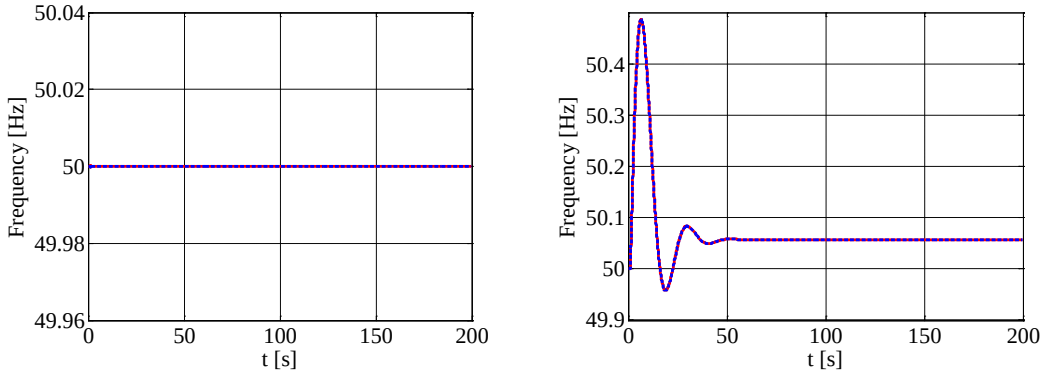

(a) Grid 1 Frequency (b) Grid 2 Frequency

Figure 60 Frequency in Grid #1 and #2 for Case 1 and Case 2 for loss of load in Grid #2.

Case 3 and 4: multiple grids receiving frequency support

In Case 3 and Case 4, both Grid #1 and Grid #2 receive frequency support from the offshore wind farm. Therefore, the converter controllers at Terminal #1 and #2 operate both in frequency droop and in dc voltage droop. In Case 3, converters controller at Terminal #3 changes the offshore grid frequency in proportion to change in dc voltage, while in Case 4, Grid #1 frequency is directly sent to the Terminal #3. Again, loss of load in Grid #1 and Grid #2 are simulated for these two cases.

Loss of load in Grid 1

A loss of load in Grid #1 was simulated for Case 3 and 4. Frequency plots for the two ac grids are presented in Figure 61. The results show that coordinated converter controller has a better performance. The results are similar to results from Case 1 and Case 2 for frequency disturbance in Grid #1.

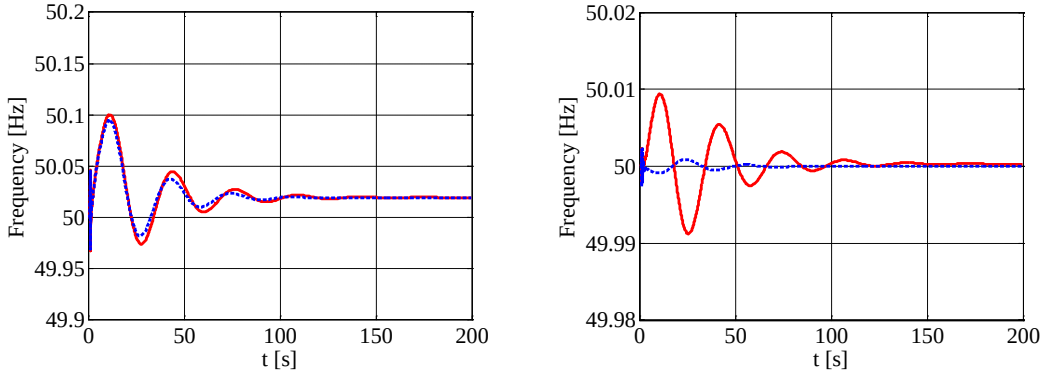

(a) Grid 1 Frequency (b) Grid 2 Frequency

Figure 61 Frequency in Grid #1 and #2 for study Case 3 (solid line) and Case 4 (dashed line)

Loss of load in Grid 2

For a frequency disturbance in Grid #2, both Terminal #1 (Grid #1) and Terminal #3 (wind farm) change their power flow and participate in the frequency regulation. Case 3 results are similar to Case 1. However, in Case 4, the offshore wind farm tries to regulate Grid #1 frequency and undesired interactions between the converter controllers in Terminal #1 and #3 is occurs. This can be seen from Figure 62 (a), where the frequency disturbance in Grid #1 is higher in Case 4 than Case 3.

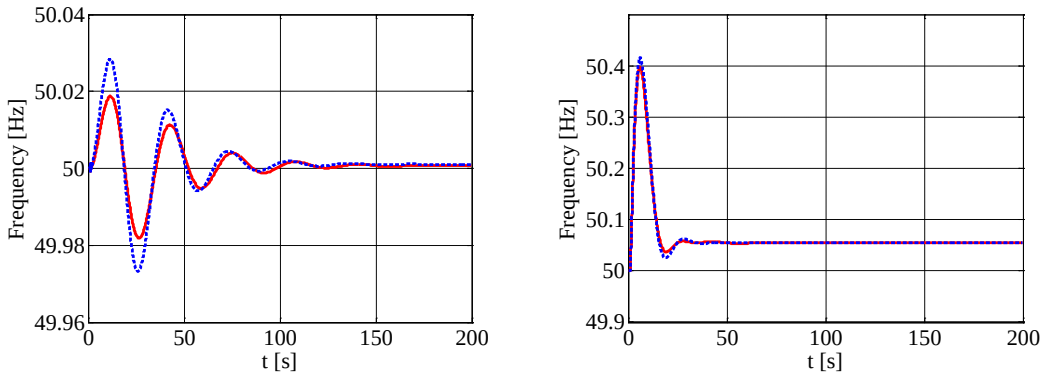

(a) Grid 1 Frequency (b) Grid 2 Frequency

Figure 62 Frequency in Grid #1 and #2 for study Case 3 (solid line) and Case 4 (dashed line)for loss of load in Grid #2.

Furthermore, the power production from the wind farm oscillates between increasing and decreasing its output. This is because the wind farm is trying to regulate Grid #1 frequency, while Terminal #1 is trying to contribute to the dc grid voltage regulation.

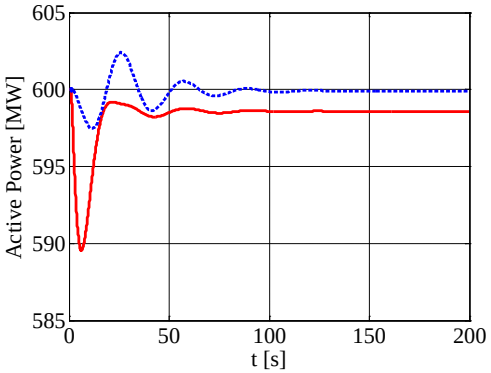

Figure 63 Offshore Wind farm output for Case 3 (solid line) and Case 4 (dashed line) for loss of load in Grid #2.

Laboratory demonstration of inertial response from VSC-HVDC connected OWPPs

This work was carried out as a master's thesis work. Detailed descriptions of the laboratory setup and obtained results can be found in [Støylen, 2015] and [Støylen, 2014].

A communication-less method for obtaining inertial response from a HVDC-VSC connected wind farm was proposed and verified experimentally. A simplified sketch of the laboratory set-up used in the experiments can be seen in Figure 64. An induction motor-generation set is used as a wind farm equivalent and a synchronous generator together with a transmission line equivalent is used to represent a weak AC grid. The wind farm equivalent and weak grid are interconnected through a HVDC network using two VSC converters. The DC cables are modelled as resistances. The laboratory components have ratings in the range of 20 kVA. Some simplifications were made regarding modelling of the wind farm. The generator representing the wind farm is directly connected to the HVDC converter terminal VSC_A. Hence, the wind farm collection grid and the turbine frequency converter are neglected. In a real system, the frequency converter in the turbines would directly relate to the kinetic energy stored in the rotating parts of the wind turbine, whereas the converter control in VSC_A would modify the frequency in the collection grid.

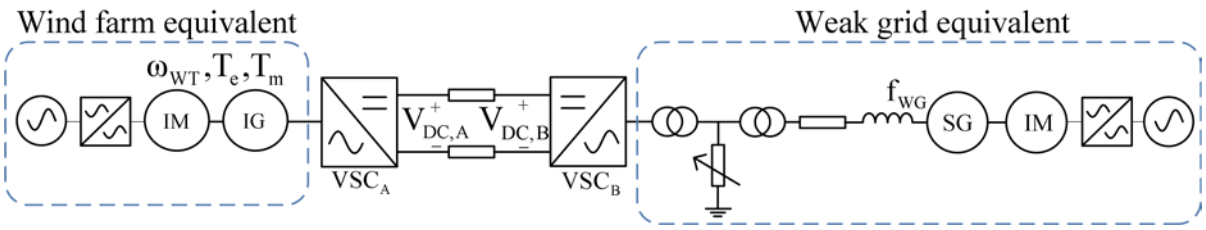

Figure 64 Laboratory system set-up.

The objective of the work was to enhance the frequency stability of the weak grid following a disturbance in power balance by emulating an inertial response from the HVDC-VSC connected wind farm. This is done by implementing additional controls on the VSC converter terminals. On the weak grid connected converter, the control relates DC voltage $V_{DC,B}$ to changes in system frequency f_{WG}. Further, the control on the wind farm connected converter relates changes in DC voltage $V_{DC,A}$ to changes in the electrical torque reference T_e in the wind turbines. In this way, a coupling of the inertia of the wind turbines to the weak grid is obtained.
The results show that the inertial response from the wind farm has a beneficial impact on the frequency response in the weak grid during the transient event following a power imbalance. The wind farm equivalent is able to modify the frequency nadir and the time at which it occurs. In the best case, the first frequency dip is reduced from 3.7 Hz to 2.5 Hz, which corresponds to an improvement of 48.2 %. The first dip is also shifted in time with approximately 1.3 seconds, compared to base case.

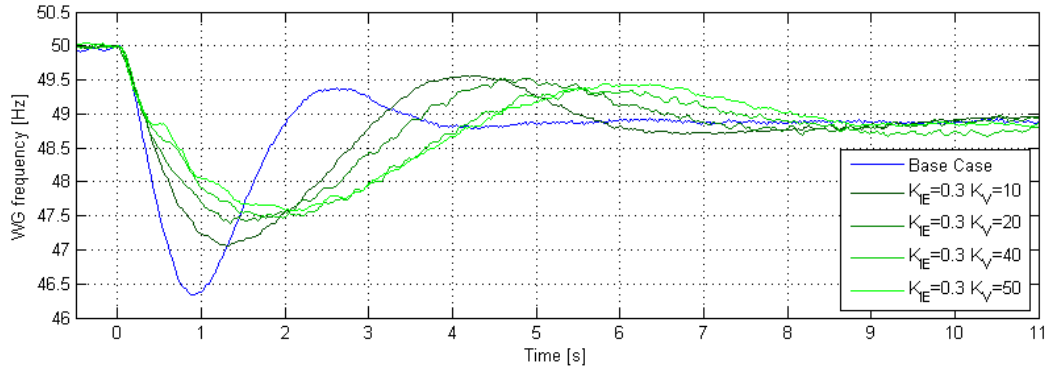

Figure 65 Laboratory measurement of frequency response with different levels of inertia emulation.

Summary
The implementation of frequency and DC voltage control on OWPPs was described in this section related to (i) frequency control provision from a point-to-point HVDC connected OWPP and to (ii) DC voltage control from OWPPs connected to DC grids. In the former, the similar performance of communication-based and coordinated frequency control was demonstrated and OWPPs's limitations were highlighted. For the latter, the big challenges that will have to be overcome if a significant part of DC voltage control to HVDC grids is to be provided by OWPPs have been illustrated and solutions have been discussed.

Moreover, the work performed showed that by coordinating converter controllers at offshore wind farm and one ac grid, it is possible to maximize frequency support contribution of the offshore wind farm and avoid disturbance in other AC grids connected to the MTDC. However, the proposed method works when only one ac grid is getting frequency support and the remaining ac grid connected MTDC terminals are operating in dc droop or constant power control mode. If more than one ac grids are to receive frequency support through MTDC grid, then negative interactions occur when the proposed controller is used.
Finally, a laboratory demonstration of inertial response from HVDC connected wind farm was shown, giving further credibility to some of the results obtained with simulation software.

3.1.2 Onshore AC voltage control

Onshore AC voltage control is a service that can most of the times be decoupled from the behaviour of the OWPP, in case it is HVDC connected. In these terms, interesting results related to the connection of an onshore HVDC terminal to weak networks were derived in [Zeni, 2015a] and [Zeni, 2014], where it was shown that the non-linearity of a weak network's characteristic in the Q-V plane may give rise to non-constant contribution of the HVDC station's voltage control to the small-disturbance short circuit power of the AC network it is connected to.

A case when onshore AC voltage control and OWPP's operation is not decoupled is related to the long-term voltage control stability of the system. As was shown in [Zeni, 2015a] and [Zeni, 2013], the prioritisation of reactive power in heavily stressed power systems undergoing possible voltage collapse is crucial. Taking the simple circuit

in Figure 66 as an example, a load Z_{LD} is placed in between a stiff network V_g and an HVDC converter, modelled as voltage source V_{AC} in normal operation and as a current source I_C when its current limit is reached.

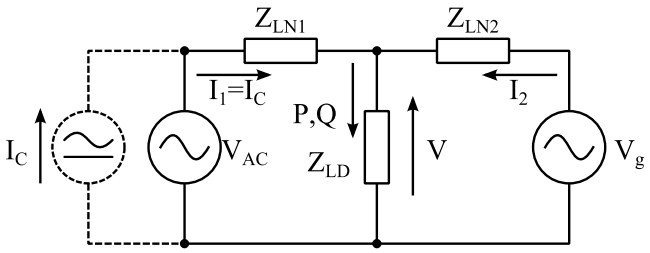

Figure 66 Simple circuit for long-term voltage stability assessment [Zeni, 2013].

As the load increases, assuming equal sharing of the load by the two sides, the HVDC converter reaches its current limit and hence voltage control capability. The prioritisation strategy of the current under such conditions has an influence on the long-term voltage profile of the system (PV curves). As shown in Figure 67, using a vector prioritisation for the current rather than prioritising active current (I_d, related to P) is beneficial for the voltage stability period, as the active power limit where the voltage stability is lost is larger. The ideal case is that in which both terminals are ideal voltage sources.

Although this result is not surprising by itself, it has counterintuitive implications for the OWPP operation, since its prime objective is to maximise its active power production and hence prioritisation of active current would be the most intuitive choice. The results emphasise that coordination between TSO and OWPP/HVDC operator is crucial to maintaining a mutually beneficial system integrity.

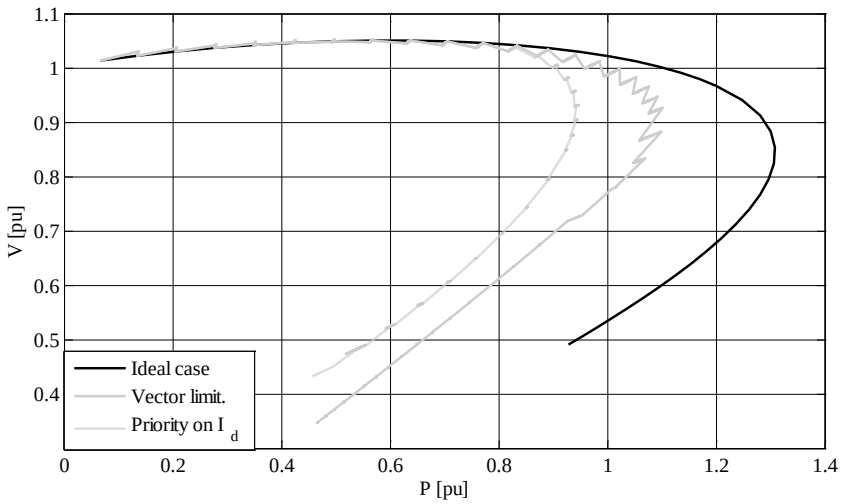

Figure 67 Influence of current prioritisation strategy on long-term voltage stability of three-bus system (Zeni, 2015).

3.1.3 Small-signal stability and power oscillation damping

Interactions across AC-DC grids

An important research topic is the dynamic interactions between MTDC grids and the ac systems. In recent years, different methods for building small signal model of dc grids [Rault, 2012] in combination with ac grids [Chaudhuri, 2011], [Kalcon, 2012], [Rault, 2013] have been presented in literature. In [Rault, 2013], the interaction between ac and dc grids is investigated by using modal analysis. Recently, reference [Zadeh, 2014] analysed the small signal stability of the CIGRE test grid system and studied the effect of using different controller types. Although in essence, the dc voltage droop control is a distributed system control, which might cause an increased coupling of dynamic phenomena in different subsystems, little work has been conducted so far to study possible coupling of ac system dynamics through MTDC systems. This research work aims at addressing this lacuna by focusing on identifying interactions between the different ac systems connected to the same dc grid. This section deals with a case where synchronous generators are located in different ac grids that are linked through a dc grid. The study investigates interactions between the electro-mechanical modes of synchronous generators across a dc system, and how different conditions such as the MTDC converter control mode, tuning, etc. influence these interactions.

Modal analysis is used in order to identify these interactions and the findings are verified through time domain analysis.

System modelling

Figure 68 shows the test system used to investigate interactions between asynchronous ac grids connected through an MTDC grid. It is a symmetrical monopolar ±400kV four-terminal VSC-based MTDC grid connected to three different multi-machine ac systems, modelled in DIgSILENT *PowerFactory*. In total, there are eight synchronous generators in the test system. AC grid #1 has four generators and is largely based on the two area system in presented [Kundur, 1994]. Identical grids with two generators are used for AC grid #2 and #3. Governor and automatic voltage controller models are included for each generator so as to capture the complete generator dynamics.

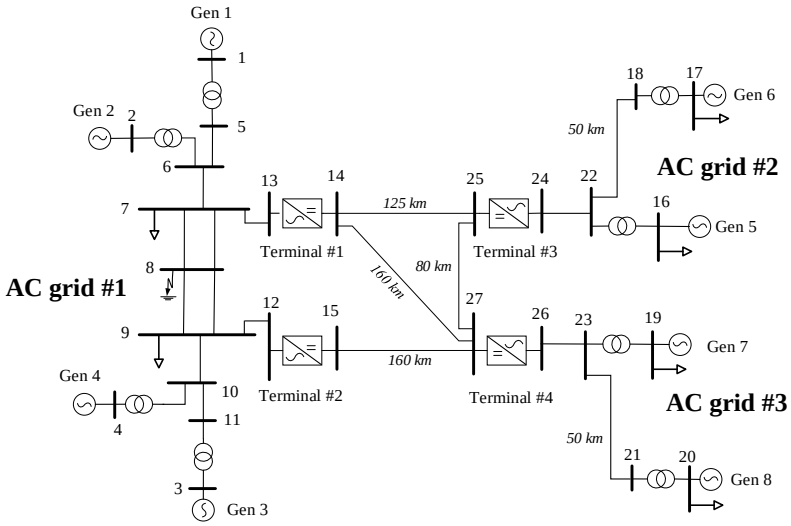

Figure 68 Studied hybrid AC/DC system.

The dc grid has a symmetrical monopole configuration. DC cables are modelled as π models with lumped parameters. Two of the dc grid terminals (#1 and #2) are connected to the same ac grid with two long transmission lines between them on the ac side. The other two dc grid terminals (#3 and #4) are connected to different ac grids each. Converters at terminals #1 and #2 operate in rectifier mode while converts at terminals #3 and #4 operate in inverter mode. The initial steady state dc grid voltages and power flows at the converter terminals are presented in Table 9. A power flow out of the dc grid and into the ac system is defined as positive.

Table 9 Initial power flow and dc voltage values at MTDC converter terminals

Terminal #	**1**	**2**	**3**	**4**
P_{rated} (MW)	750	1000	900	800
U_{rated} (kV)	400	400	400	400
$P_{initial}$ (MW)	-500	-800	600	685.4
$U_{initial}$ (kV)	406	401.1	399	400

All dc grid terminal converters are operating in dc droop and reactive power control modes. DC droop control is a distributed type of converter control where more than one converter participate in the dc voltage control by contributing balancing power. It is considered as the most appropriate control strategy in MTDC grids because it provides higher reliability as the system is not dependent on a single converter to control the voltage. Furthermore, the strategy does not require communication. The steady state equation of a dc droop controller is:

$$P^* - P + k_{droop}\left(U_{dc}{}^* - U_{dc}\right) = 0 \qquad (3.1)$$

Where P^* and $U_{dc}{}^*$, and P and U_{dc} represent reference and measured active power and dc voltage, respectively. The droop constant k_{droop} defines the relationship between the change in active power flow and the change in dc

voltage. The block diagram of the outer converter control loops are shown in Figure 69. The internal current controllers defined in *PowerFactory* are used for the inner converter control loops.

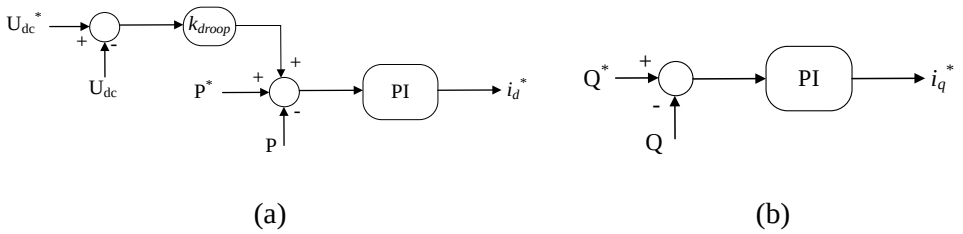

(a) (b)

Figure 69: Converter outer converter control loop: (a) dc voltage droop and (b) reactive power control.

Modal Analysis

Small signal stability is defined as the ability of the power system to maintain synchronism when subjected to small disturbances [Kundur, 1994]. Small signal stability problems are usually analysed by linearized models, and thus powerful methods based on linear algebra are used to characterize the dynamic behaviour of the system. In this case, modal analysis is used to identify electro-mechanical modes and their interactions. The dynamic behaviour of a power system can be described by a linear differential equation of the form:

$$\Delta\dot{\mathbf{x}} = \mathbf{A}\Delta\mathbf{x} + \mathbf{B}\Delta\mathbf{u} \qquad (3.2)$$

where **x** is the state vector, **u** is the input vector, **A** is the state matrix and **B** is the input matrix. Eigenvalues, also known as modes, are the roots of the characteristic equation of the state matrix **A**, and can be real or appear in complex conjugate pairs ($\lambda = \sigma \pm j\omega$). If all the eigenvalues have negative real parts, the system is stable. For each eigenvalue λ_i, one can define right ($\mathbf{\Phi_i}$) and left ($\mathbf{\Psi_i}$) eigenvectors which satisfy the equations $\mathbf{A}\mathbf{\Phi}_i = \lambda_i\mathbf{\Phi}_i$ and $\mathbf{\Psi}_i^T\mathbf{A} = \lambda_i\mathbf{\Psi}_i^T$, respectively. The elements of each of the right eigenvectors ($\mathbf{\Phi_i}$) indicate the relative activity of the state variables when the associated mode is excited. This gives information about the observability of the different modes. The magnitudes of the eigenvector elements describe the extent of the activity, while for complex (oscillatory) modes, the relative phase angles indicate the direction of oscillation in the associated state variables. The elements of the right eigenvectors are also called *mode shapes*. Left eigenvectors measure the activity of a state variable in an eigenvalue, and thus they contain information about the controllability of the modes. Moreover, by multiplying elements of the right and left eigenvectors, i.e. $p_{ji}=\phi_{ji}\psi_{ji}$, one can obtain an indication of the participation of state variable *j* in mode *i* (defined as participation factor p_{ji}).

Effect of DC grid interconnection

This section investigates how the dynamic behaviour of ac grids is affected by the introduction of MTDC systems. Two modal analyses were carried out using DIgSILENT *PowerFactory*. First, linear analysis is carried out for three isolated asynchronous ac grids separately. Then, a four terminal dc grid is used to interconnect the asynchronous grids and create the hybrid ac/dc power system shown in Figure 68. The hybrid ac/dc system is studied to with focus on ac grid modes to see whether they shift their positions in the complex plane, when a dc grid is added compared to the case where the ac grids were operating independently.

In the case of eigenvalue analyses for the individual isolated ac grids, it was found that AC grid #1 has 44 modes, while both AC grid #2 and #3 have 28 modes each. All eigenvalues have negative real parts indicating stable operating conditions. The state variables in the AC grids are related to the generators, AVRs and governors. AC grid #2 and #3 have identical grid topology and same types of generator controllers are used for the generators the grids. The difference between these two grids is the initial operating condition before the linear analysis is done. Therefore, the (small) difference in modes in these two grids arise from difference in power flow. Table 10 shows the least damped eigenvalues in the different ac grids with damping ratio less than 15%.

Table 10 Modes of asynchronous AC grid with less than 15% damping ratio

Grid 1				
Name	**Eigenvalue**	**Damped Frequency**	**Damping Ratio**	**Damping Time Const.**

$\lambda_{26\&27}$	-0.06 ± j3.41	0.54	0.016	18.15
$\lambda_{24\&25}$	-0.64 ± j6.32	1.01	0.101	1.56
$\lambda_{22\&23}$	-0.65 ± j6.36	1.01	0.101	1.54
Grid 2				
$\lambda_{14\&15}$	-0.59 ± j6.13	0.975	0.097	1.68
Grid 3				
$\lambda_{13\&14}$	-0.41 ± j5.78	0.920	0.070	2.45

A second eigenvalue analysis was done for a system with an MTDC system interconnecting the three asynchronous ac grids. DC voltage droop control is implemented at all dc grid terminal converters. In this case, the total number of modes in the system increased to 160. In addition to the state variables associated with the generators and their controllers in each ac grid (44+28+28=100), the states in the hybrid AC/DC system include 44 state variables associated with the filters, VSC converters and their controllers, and 16 state variables related to the DC grid cables. The least damped modes, with damping ratio less than 15%, in the hybrid AC/DC system are presented in Table 11.

Table 11 Poorly damped modes in hybrid ac/dc grid with dc droop control in MTDC converters

Name	Eigenvalues	Damped Frequency	Damping Ratio	Damping Time Const.
$\lambda_{120\&121}$	-0.06 ± j3.45	0.55	0.017	17.29
$\lambda_{104\&105}$	-0.17 ± j5.63	0.90	0.029	6.03
$\lambda_{106\&107}$	-0.45 ± j5.79	0.92	0.078	2.22
$\lambda_{102\&103}$	-0.63 ± j6.29	1.00	0.100	1.58
$\lambda_{100\&101}$	-0.65 ± j6.35	1.01	0.102	1.54
$\lambda_{6\&7}$	-149.23 ± j1423	226.59	0.104	0.007
$\lambda_{2\&3}$	-176.18 ± j1427	227.19	0.122	0.006
$\lambda_{10\&11}$	-149.23 ± j1069	170.20	0.138	0.007

Table 10 and Table 11 are used to examine the effect of addition of the MTDC on the ac modes. The modes in the hybrid AC/DC system are a mere combination of the modes in the separate ac grids, and the additional modes that are related to the dc grid, converters and their controllers. The poorly damped mode in AC grid #2 ($\lambda_{14\&15}$=-0.59 ± j6.13) had a damping ratio of 9.7% when the ac grid was evaluated independently. However, this mode shifted its position to -0.17 ± j5.63 in the hybrid ac/dc grid, and became more critical with damping ratio of 2.9%.
The eigenvalues do not change when the type of control method implemented, either dc voltage droop or master-slave control, in the MTDC converters is changed.

Case studies
Mode shapes of the eigenvalues are studied in detail to understand interactions between asynchronous ac grids. Furthermore, the control parameters of the MTDC converter controllers are varied and its effect on the degree of interaction between the different ac grids is investigated. Finally, time domain simulation of the test system for a fault in AC grid #3 is presented to support the findings of the modal analysis.

Mode shapes
The mode shapes (right eigenvectors) of λ_{120}, λ_{92} and λ_{94} have been calculated using the *modal analysis* function in *PowerFactory*. As stated earlier, mode shapes measure the relative activity of the state variables when a particular mode is excited. Thereby, it shows how observable a mode is in a state variable. To be able to make a direct and fair comparison of mode shapes we focus on generator speeds as the state variable of interest. Table 12 presents the normalized mode shapes of the generator speeds for eigenvalues λ_{120}, λ_{92} and λ_{94}. The normalization of the magnitudes of the mode shapes is performed by rescaling them such that the relative contribution of the largest speed mode shape magnitude is equal to 1. This means that the mode shape magnitudes of the remaining generators are presented in reference to the generator with the largest observability. This normalization method is used in the following sections.

Table 12 Normalized mode shapes and angles of dominant modes in all of the ac grids.

State variable	AC grid #	Mode shapes					
		λ_{120}		λ_{104}		λ_{106}	
		Mag.	Angle (deg)	Mag.	Angle (deg)	Mag.	Angle (deg)
Gen1: speed	1	0.8117	24.23	0.0232	-83.82	0.0158	-82.29
Gen2: speed	1	0.6016	33.46	0.0054	69.91	0.0053	1.19
Gen3: speed	1	1	-141.6	0.0252	-77.39	0.0208	-80.77
Gen4: speed	1	0.9026	-143.66	0.0055	95.96	0.0056	3.95
Gen5: speed	2	0.0130	108.98	0.5502	97.48	0.0232	72.4
Gen6: speed	2	0.0183	107.14	1	-83.22	0.0690	-70.03
Gen7: speed	3	0.0118	109.12	0.0419	-68.99	0.5016	61.45
Gen8: speed	3	0.0167	109.01	0.0480	107.97	1	-98.51

Eigenvalues λ_{120}, λ_{104} and λ_{106} have the highest observabilities in speed state variables of Gen3, Gen6 and Gen8, respectively. For eigenvalue λ_{120}, Gen3 has the largest magnitude followed by Gen4, Gen1 and Gen2. From the relative phase angle difference of mode shapes of λ_{120}, it can be seen that speeds of Gen1 and Gen 2 are oscillating against Gen3 and Gen4. This indicates that λ_{120} is an inter-area mode in AC grid #3. However small, λ_{120} is also observable in Gen5-8, which indicates a coupling of this dynamic interaction (dominant in AC grid #3) with generators in other ac systems connected via the MTDC grid. A similar conclusion holds for the other two modes that are studied.

Controller tuning

To investigate the effect the tuning of converter controllers has on the interaction (and the extent to which this is translated into changes of the modes shapes), the integral time constants (T_i) were changed in the PI controller of the outer loop of the VSC converters, i.e. P and Q control (see Figure 69). The results of the modal analysis were used as a reference base case. Two cases of T_i values were considered. In the first case, T_i=0.08 was used, which made the converter respond faster compared to the base scenario. In the second case, T_i=0.5 was implemented and the response of the converter controllers was slower compared to the base scenario. The mode shapes of λ_{120}, λ_{92} and λ_{94} were calculated for the two cases, and their changes compared to the base case are presented in Table 13.

Table 13 Effect of converter parameter variation on mode shapes of poorly damped modes.

State variable	AC grid #	Mode shapes					
		λ_{120} (0.55 Hz)		**λ_{92} (0.93 Hz)**		**λ_{94} (0.90 Hz)**	
		Case 1 (Δ%)	Case 2 (Δ%)	Case 1 (Δ%)	Case 2 (Δ%)	Case 1 (Δ%)	Case 2 (Δ%)
Gen1: speed	1	0.25	-7.75	**-22.22**	**9.26**	**-23.91**	**13.04**
Gen2: speed	1	0.25	-8.7	**-30.77**	**23.08**	**-25**	**6.25**
Gen3: speed	1	-0.99	-1.85	**-25.42**	**15.25**	**-26.23**	**14.75**
Gen4: speed	1	-0.99	-0.78	**-38.46**	**38.46**	**-23.53**	**23.53**
Gen5: speed	2	**-33.95**	**46.51**	-5.54	9.68	**-25**	**16.18**
Gen6: speed	2	**-33.88**	**43.42**	-0.09	3.65	**-23.27**	**11.88**
Gen7: speed	3	**-33.67**	**45.41**	**-24.74**	**15.46**	-2.59	6.4
Gen8: speed	3	**-33.57**	**42.24**	**-22.32**	**8.93**	0.65	0.99

In general, the observability of the modes in the generators' state variables decreases in Case 1 and increases in Case 2. This means that when the converter response becomes faster, the interaction between the asynchronous

grids is reduced and vice versa. The change in observability of the modes is small for generators in the grid where the eigenvalues are dominant. The largest relative changes occur in observabilities for the generator speeds found in remote MTDC-connected ac systems. Similarly, a slower converter controller leads to higher degree of coupling of the dynamic phenomena in the ac systems and hence increased interactions between asynchronous grids connected through MTDC systems.

Converter control methods

In [Endegnanew, 2015], dynamic interactions between asynchronous ac grids interconnected via MTDC were identified using modal and time domain analyses. Furthermore, the research work showed that the interaction level is lower and higher when the terminal converters' time response was faster and slower, respectively. In this section, a similar approach is used as in [Endegnanew, 2015] to investigate how the level of dynamic interactions between asynchronous ac grids linked through dc grid varies for different types of dc grid terminal converter control methods. The control methods studied are dc voltage droop and master-slave control. For each type of control method implementation, mode shapes of poorly damped eigenvalues in the hybrid ac/dc system are analysed in detail to identify interactions between the asynchronous ac grids.

DC droop control

Table 14 shows mode shapes of poorly damped modes with dc voltage droop control mode implemented in MTDC terminal converters.

Table 14 Magnitude of mode shapes of poorly damped modes with dc voltage droop control mode implemented in MTDC terminals.

State Variable	Grid #	λ_{120}	λ_{104}	λ_{106}
Gen1; speed	1	0.8	0.0007	0.00106
Gen2; speed	1	0.58	0.0002	0.00025
Gen3; speed	1	1	0.00097	0.00129
Gen4; speed	1	0.91	0.0003	0.00029
Gen5; speed	2	0.00057	0.0011	0.51
Gen6; speed	2	0.00079	0.0033	1
Gen7; speed	3	0.00052	0.49	0.00179
Gen8; speed	3	0.00072	1	0.00217

Master-slave control

In the case where master-slave control is implemented for dc grid control, converters at terminals #1, #2, and #3 operate in constant power mode while the converter at terminal #4, which is connected to AC grid #3, operates in constant dc voltage control mode. Table 15 shows mode shapes of poorly damped modes in the test system with master-slave dc grid control mode.

Table 15 Mode shapes of poorly damped modes with master-slave control mode implemented in MTDC terminals.

Name	AC grid #	λ_{120}	λ_{104}	λ_{106}
Gen1; speed	1	0.80	0.000023	0.00000049
Gen2; speed	1	0.59	0.000008	0.00000014
Gen3; speed	1	1	0.000034	0.00000071
Gen4; speed	1	0.91	0.000012	0.00000018
Gen5; speed	2	0.000021	0.000040	0.51
Gen6; speed	2	0.000041	0.000118	1
Gen7; speed	3	0.002	0.48	0.008
Gen8; speed	3	0.003	1	0.010

Comparing the mode shape magnitude of λ_{120} for the two converter control methods evaluated (Table 14 and Table 15), it can be seen that the mode is most observable in state variables of generators found in AC grid #1. However, the observability of the mode in state variables of generators from asynchronous grids is an order of magnitude

apart. Thus, it can be concluded that the interaction between asynchronous ac grids is higher when all converters are operating in dc droop control mode. Otherwise, the interaction is limited to an asynchronous grid behind the master controller terminal of the MTDC grid. A similar conclusion can be drawn from the mode shapes of the other two dominant modes; λ_{104} and λ_{106}.

Similar eigenvalue damped frequency

This section analyses the extent of interaction between generators in asynchronous grid when the dominant modes in different asynchronous grids have similar damped frequency. The converters at the dc grid terminals operate in dc voltage droop control and the power flow at the terminals is not changed. However, the power flow inside AC grid #3 is changed by changing the power settings of Gen7&8 and the loads in the system. In addition, the rated power and the inertia time constant of the generators are also changed. These changes were made to make the modes in AC grid #2 and #3 different from each other. As mentioned in 3.1.2, the two grids have identical system topology, network parameters, controllers, generator types and parameter settings. The only difference between them is the initial steady state power flow. For this reason, the modes in the two grids are almost the same. In order to avoid looking at identical modes found in two different grids, it was necessary to change some system parameters in AC grid #3 so that the grid is dynamically different from grid #2.

Results from the modal analysis show that the least damped modes have damping ratio of 1.7%, 7.8% and 9.7% (see Table 16). State variables of Gen1-4, Gen5&6 and Gen7&8 have strongest participation in $\lambda_{125,126}$, $\lambda_{106,107}$, and $\lambda_{92,93}$ respectively. The dominant modes in AC grid #1 ($\lambda_{125,126}$) and #2 ($\lambda_{106,107}$) are the same as the ones studied in the previous section. This is to be expect as no changes were made in these two grids, the modes will remain the same. However, the dominant mode in AC grid #3 ($\lambda_{92,93}$) has changed its position because of the changes made in the generators' settings and parameters.

Table 16 Poorly damped modes in the modified study system.

Name	Eigenvalue	Damped Frequency	Damping Ratio	Damping Time Const.
	1/s	***Hz***		***s***
$\lambda_{125,126}$	-0.06 ± j3.45	0.55	0.017	17.29
$\lambda_{106,107}$	-0.45 ± j5.79	0.92	0.078	2.22
$\lambda_{92,93}$	-0.79 ± j8.05	1.28	0.097	1.27

The inertia constant parameter of Gen7&8 in AC grid #3 was varied between H=4.25 s and H=8.5 s. Although the large inertia time constants might not be realistic, the change in H parameter was used to move the position of dominant mode in the grid and find a position where the damping frequencies of the dominant modes in AC grid #2 and #3 are similar. Table 17 shows the change in the dominant mode for five values of inertia time constants. For H=7.3 s, the damped frequency of the dominant mode in AC grid #3 matches that of AC grid #2, i.e. 0.92 Hz.

Table 17 Dominant mode in Grid 3 for different values of inertia time constant in Gen 7 and Gen 8.

H	Name	Eigenvalue	Damped Freq	Damping Ratio	Damping Time Const.
s			***Hz***		***s***
4.25	$\lambda_{92,93}$	-0.79 ± j8.05	1.28	0.097	1.27
5.52	$\lambda_{96,97}$	-0.74 ± j6.95	1.11	0.106	1.35
7.3	$\lambda_{106,107}$	-0.52 ± j5.79	0.92	0.089	1.93
7.65	$\lambda_{106,107}$	-0.44 ± j5.68	0.90	0.077	2.29
8.5	$\lambda_{106,107}$	-0.33 ± j5.47	0.87	0.060	3.05

As the inertia time constant increases, the damping ratio of the mode first increases and then decreases, while the damped frequency continuously declines. Figure 70 shows how the damping ratio varies for the different values of inertia time constants evaluated.

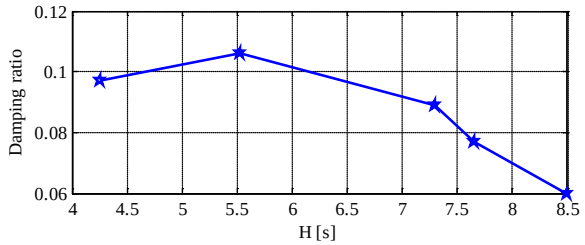

Figure 70 Damping ratio of the dominant mode in Grid 3 for different inertia time constant.

Mode shapes of the dominant eigenvalue in AC grid #3 were calculated for all cases of the inertia time constants considered. The magnitudes of the mode shapes related to the speed state variable of the generators' in the whole system are shown in Table 18. The mode shape magnitudes are presented as percentage.

Table 18 Observability of dominant mode in AC grid #3 for different values of inertia time constant in Gen 7&8.

State variable	AC grid #	H [s]				
		4.25	***5.52***	***7.3***	***7.65***	***8.5***
		(%)	***(%)***	***(%)***	***(%)***	***(%)***
Gen1; speed	1	0.004	0.008	0.086	0.077	0.067
Gen2; speed	1	0.020	0.046	0.021	0.012	0.013
Gen3; speed	1	0.005	0.009	0.119	0.107	0.096
Gen4; speed	1	0.026	0.059	0.024	0.015	0.019
Gen5; speed	2	0.036	0.073	0.867	0.389	0.051
Gen6; speed	2	0.002	0.022	1.612	0.959	0.283
Gen7; speed	3	81.9	73.9	43.5	44.7	54.0
Gen8; speed	3	100	100	100	100	100

Focusing on the observability of the dominant mode in AC grid #3 in the speed state variables of generators in AC grid #2, it can be seen that the level of interaction in highest when the dominant modes both in AC grid #2 and #3 have the same damped frequency, i.e. H=7.3 s. This is clearly shown in the plot of mode shapes for Gen5&6 state variables in Figure 71.

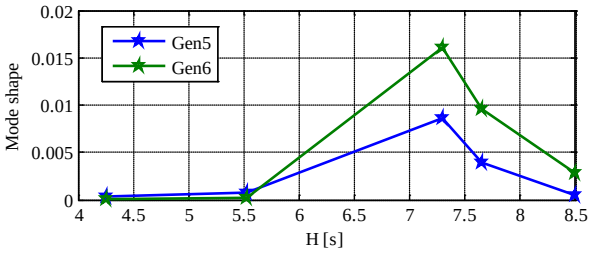

Figure 71 Observability of dominant mode in AC grid #3 in speed state of generators in AC grid #2 for different H values.

The change of inertia constant of generators in AC grid #3 has no effect on the poorly damped mode in AC grid #2. The mode remains at -0.45 ± j5.79 for all H values evaluated. However, the observability of the mode in generators speed state variables in AC grid #3 changes. Table 19 shows the mode shape of the dominant mode in AC grid #2 related to speed state variables. Again, the observability of the mode in speed state variables of the generators in AC grid #3 is highest for H=7.3 s.

Table 19 Mode shape of dominant mode in AC grid #2 for different values of inertia time constant in Gen 7&8.

State variable	AC grid #	H [s]				
		4.25	***5.52***	***7.3***	***7.65***	***8.5***
		(%)	***(%)***	***(%)***	***(%)***	***(%)***
Gen1; speed	1	0.11	0.11	0.11	0.11	0.11
Gen2; speed	1	0.02	0.02	0.02	0.02	0.02
Gen3; speed	1	0.13	0.13	0.13	0.13	0.13

Gen4; speed	1	0.03	0.03	0.03	0.03	0.03
Gen5; speed	2	51	51	51	51	51
Gen6; speed	2	100	100	100	100	100
Gen7; speed	3	0.12	0.06	0.73	0.51	0.19
Gen8; speed	3	0.23	0.25	1.79	0.88	0.17

Figure 72 shows the mode shapes of the dominant mode in AC grid #2 for the Gen7&8 speed state variables. It is clear from the figure that the observability of the mode in the speed state variables is highest when the damped frequency of the dominant modes in the two systems matches. This indicates higher interaction level compared to the other studied cases.

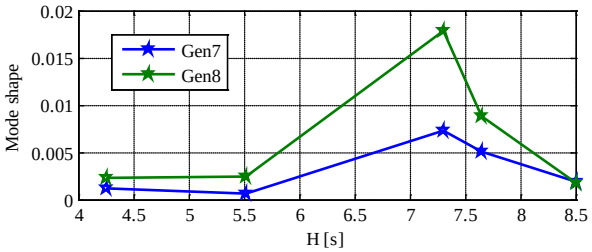

Figure 72: Observability of dominant mode in AC grid #2 in speed state of generators in AC grid #3 or different H values.

Transient study

Using the non-linear dynamic model of the power system in *PowerFactory*, a time domain study was undertaken for a three phase to ground fault in AC grid #1. The fault was applied at bus 8 at t=1s and successfully cleared after 100ms. Since the associated reduction of the ac voltages at the PCC of MTDC converters' causes the internal current limits to be reached, the fault causes a reduction in the power transferred to the dc grid (Figure 73(a)) from terminals #1 and #2, which causes the dc grid voltages to drop (Figure 73(b)). Since all converters are operating in droop control mode, the power flows at terminals #3 and #4 are also reduced during the fault to cope with the power imbalance and to contribute to the dc voltage control. This effect can be seen from Figure 73(a). Consequentially, it means that the transient disturbance in AC grid #1 causes power changes in AC grid #2 and #3 because of the actions of the dc voltage droop controllers in the MTDC converters.

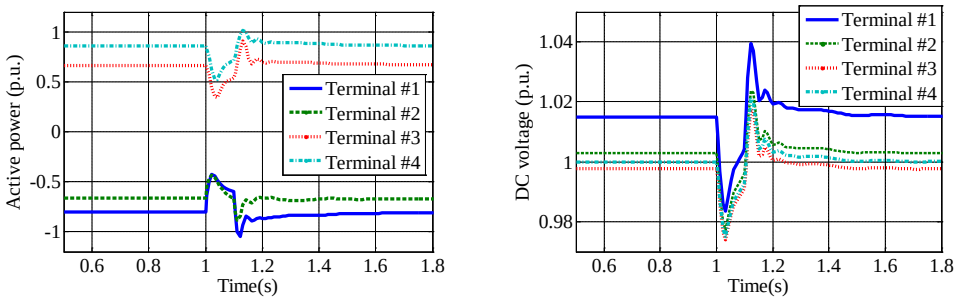

(a) (b)

Figure 73: (a) Active power transfers and (b) DC voltages at all terminals of the MTDC grid.

The abrupt change in power injections in the other ac systems causes an excitation of system modes. Figure 74 shows the generator speeds of all the generators in the studied system. After clearance of the fault, the generator speeds exhibit poorly damped oscillations. Gen 1-4 have the highest amplitude of oscillations. Gen 1&2 oscillate against Gen 3&4; which is the inter-area oscillation that was studied in the previous section (λ_{120}). Similarly, Gen 5 and 6 are oscillating against each other, which also applies to Gen 7 and 8. With the oscillation frequencies of the generator speeds equal to 0.55 Hz for Gen 1- 4, 0.89Hz for Gen 5-6 and 0.91Hz for Gen 7-8, the findings of the transient study are in accordance with the results of the modal analysis.

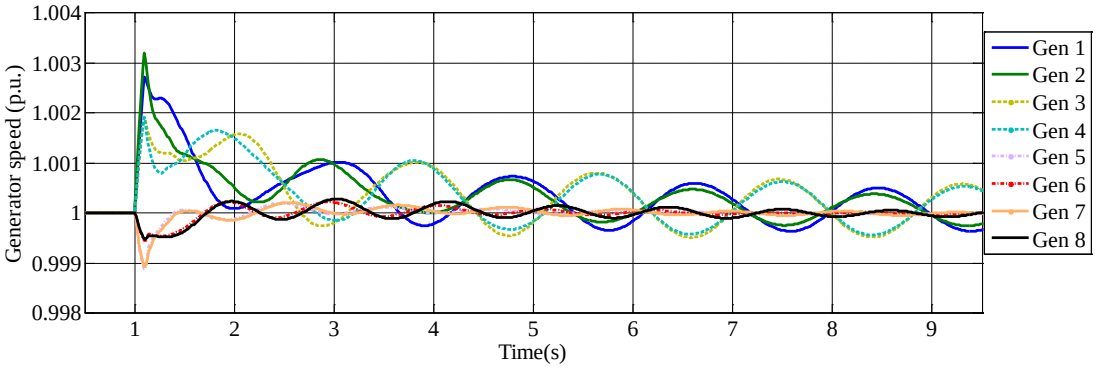

Figure 74 Generator speeds.

Contribution of OWPPs

When small-signal electromechanical oscillations are to be damped by HVDC-connected OWPPs, the latter have to participate in the service when active power modulation is needed for oscillation damping. This topic has been investigated at length in [Zeni, 2015a], [Zeni, 2016a]. The main findings of the work are summarised here.

Importance of AVRs and guidelines for parameter tuning

The above mentioned publications showed the importance of including excitation systems (ESs) and automatic voltage regulators (AVRs) for this kind of investigation was emphasised. Many publications neglect such elements, but they are crucial in determining the electro-mechanical small-signal stability of power systems. As an example, the system depicted in Figure 75 was used, and a simple power oscillation damping (POD) controller was implemented on a VSC-HVDC station connected at Bus 2, but by modulating P and Q. The control gain was increased progressively from 0 to 1 and three values for the AVR's gain were considered, giving rise to the pole movement shown in Figure 76.

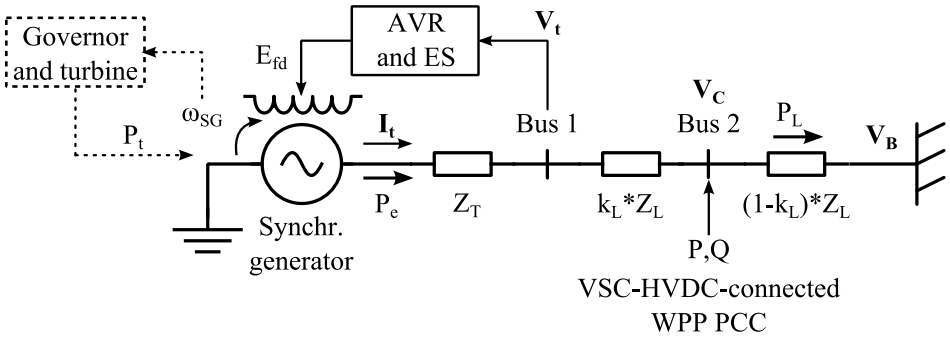

Figure 75 Simple power system model for POD investigation (Zeni, et al., 2016).

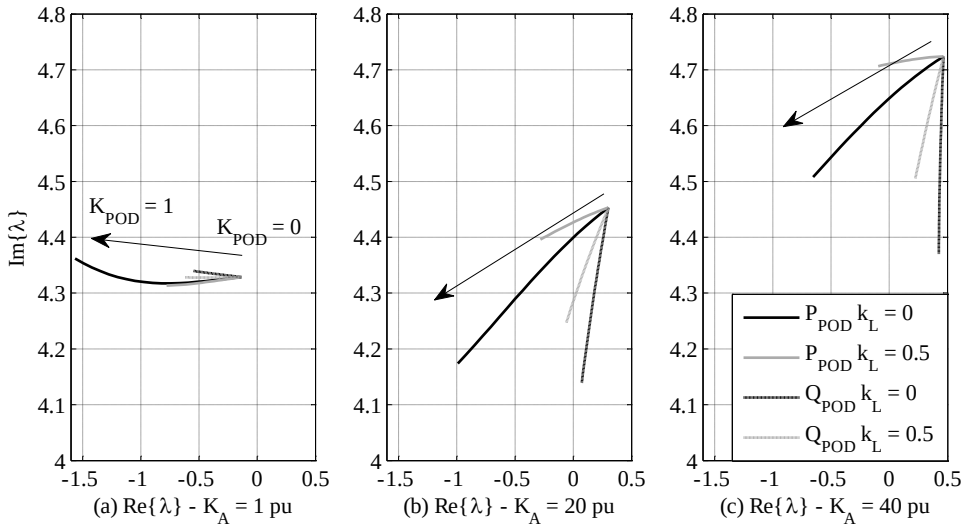

Figure 76 Pole movement for increasing POD gain with three different values of AVR gain (Zeni, et al., 2016).

Clearly, as the AVR gain increases, the pole movement is far from the desired one. The conclusion is that AVRs cannot be neglected when assessing the possible contribution of static sources to POD. In [Zeni, 2015a] and [Zeni, 2016a] the analysis is taken forward and guidelines for parameter tuning in presence of AVRs are given, making use of a phasor-like approach borrowed from [Kundur, 1994].

Implementation of POD service on OWPPs

The POD service through active power modulation requires modification of the WPP controller according to what shown in Figure 51. Feed-forward of the POD signal is necessary in order to minimise control and communication delays and perform an easier parameter tuning.

A more complex system based on IEEE 12-bus power system was used and an HVDC-connected WPP was connected to it. A POD controller was employed and tuned according to the guidelines mentioned in the previous section and the results depicted in Figure 77 were obtained when subjecting the system to a fault cleared after 100 ms.

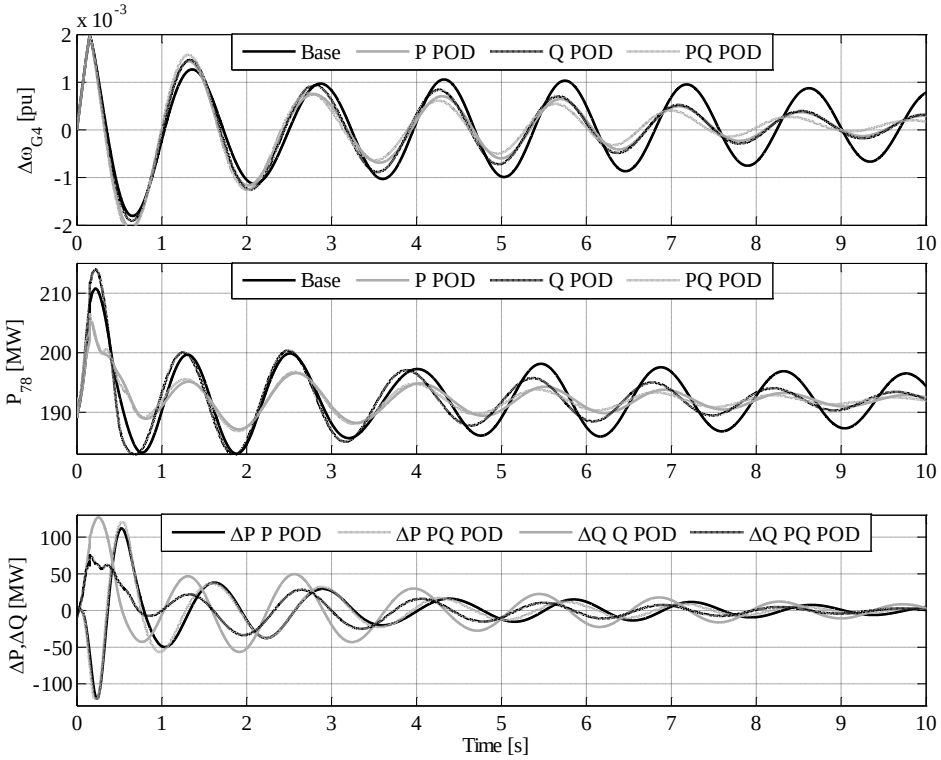

Figure 77 Results of non-linear dynamic simulation on modified IEEE 12-bus system (Zeni, et al., 2016).

The results matched well the linear analysis performed in [Zeni, 2015a] and demonstrated the feasibility of implementing this service. Furthermore, the relevance of ESs and AVRs was also shown in [Zeni, 2015a] and [Zeni, 2016a].

Limitations to POD provision

Further attention was given to other factors which may hinder the deployment of POD service in VSC-HVDC connected OWPPs. Among those are:

- Closed-loop performance limitations exist and were quantified in terms of maximum achievable closed-loop control gain.
- Closed-loop instability can occur due to excessive delays or lack of gain reduction in open-loop control chain. In case of VSC-HVDC connected OWPPs, the problem becomes more serious as the system is more complex and further lags may hence exist as compared to an AC connected OWPP.
- Control/communication delays are detrimental for this service, much more than for e.g. frequency control, and must be minimised and deterministic to ease implementation.

- Ramp-rate limiters also come into play in POD's relevant frequency ranges. Not only can their presence lead to less effective POD, but they can even further deteriorate the performance as compared to the case without POD.
- Available energy and recovery period for WTGs may be an issue when they are required to over-produce, i.e. operate above the available active power, which may be the case with POD. However, the work performed showed that it is very unlikely for this to be a real problem.
- Oscillations on WT's mechanical side may be excited by active power modulations at nearby frequency. For example, shaft and tower oscillations' frequency may be comparable to POD frequency. Possible alternatives to prevent the problem from occurring are discussed in [Zeni, 2015a].

Experiments of POD from WTs

In [Zeni, 2015a] and [Zeni, 2016b] frequency control and POD services were tested on dynamometer-driven and field WTs and the National Renewable Energy Laboratory, USA. A sample result making use of a field WT is shown in Figure 78.

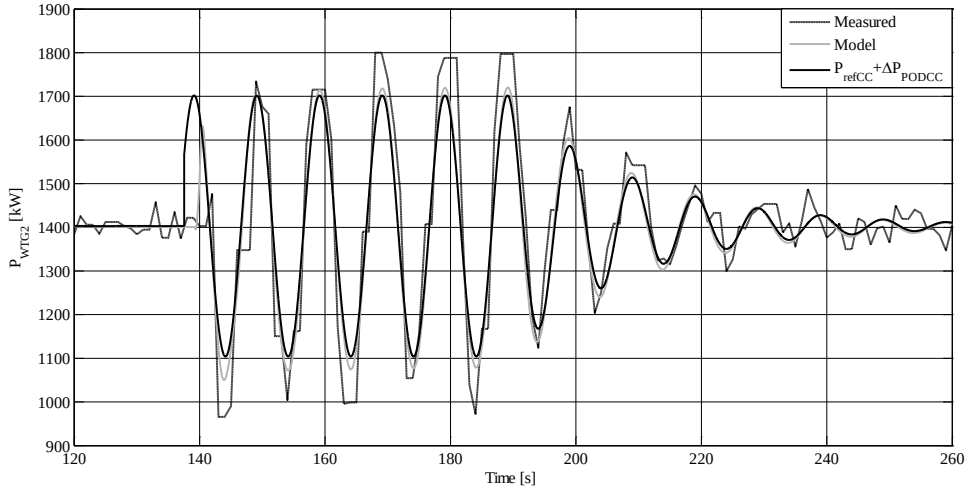

Figure 78 Validation of WT and WPP control model with POD service emulation on field WT [Zeni, 2016b]

Considering the limitations encountered in the field's setup, the results are satisfying and it can be seen that model and measurement match each other to a good extent. Further results and analysis are found in [Zeni, 2016b].

Summary

The small signal stability of a system with three multi-machine ac grids connected through an MTDC grid was analysed. It was shown that the dynamic behaviour of ac grids is not significantly affected with the introduction of dc grids to interconnect ac power systems. In addition, the work identified that synchronous generators in asynchronous grids linked via MTDC interact dynamically through the dc grid. The change in the level of these interactions was studied for different tuning, control mode and damped frequency cases. It was found that faster and slower converter control response lead to lower and higher interactions between the asynchronous ac grids, respectively. This observation is in line with the expectations that a faster control of the power balance within the dc grid will make the connected ac systems more decoupled. The level of this dynamic interaction was studied with dc voltage droop and master-slave control modes implemented in the MTDC terminal converter. The results indicated that when dc voltage droop control is used the level of interaction between generators in asynchronous grid is low but similar in scale. On the other hand, when master-slave control mode is used, the interaction with generators located in grids behind constant power controlled terminal is much lower than generators located in the grid where the constant dc voltage controlled (master) terminal is found. The final analysis showed that the level of dynamic interaction between asynchronous grids is highest when the dominant electro-mechanical modes in the different ac grids have similar damped frequency of oscillations. Results of a time domain simulation of the study system for a fault in one of the ac grids support findings of the modal analysis. The study results show that there exists a

dynamic coupling between ac grids across dc grids and that the level of interaction is influenced by the converter controller settings.

The contribution OWPPs can give to the enhancement of small-signal stability was analysed in [Zeni, 2015a] and the findings were summarised in the second part of this section. Guidelines to tune POD control parameters on static sources were generated in [Zeni, 2015a], after emphasising the need to account for ESs and AVRs in small-signal analysis. The implementation on HVDC-connected WPP was successfully tested on a dynamic simulation tool. Moreover, limiting factors for the delivery of this feature from WPPs were discussed. Finally, the experimental validation work performed at National Renewable Energy Laboratory in the US was summarised.

3.2 Connection of OWPPs to HVDC systems: control of offshore AC network

This section is dedicated to a topic which has not been given much attention to date in the literature, i.e. the control of offshore AC island networks behind HVDC converters. Details about the investigation can be found in [Zeni, 2015a] and [Zeni, 2015b].

3.2.1 Target system

The system under analysis is that depicted in Figure 79. In [Zeni, 2015a] and [Zeni, 2015b] the investigation was expended to a system comprising two offshore HVDC converter and two WPPs. The scope is restricted to the offshore AC part of the network, purely based on power electronic converters, assuming the WPP is based on Type 4 WTs.

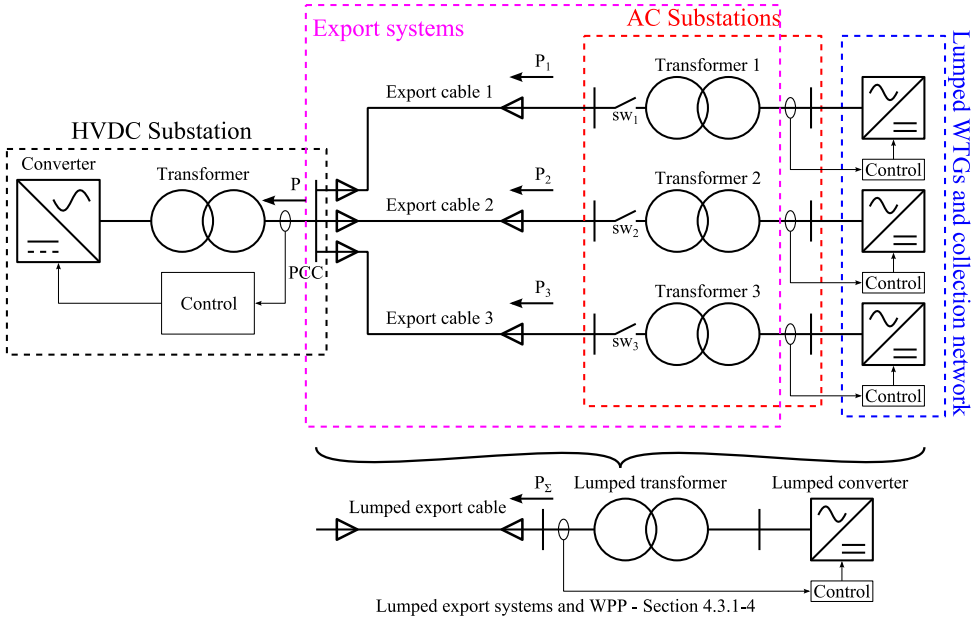

Figure 79 System under analysis for investigations regarding the control of offshore AC networks [Zeni, 2015b].

3.2.2 Control candidates

Two control candidates were considered for the offshore HVDC converter. The current references for the current controller are generated according to the two schemes shown in Figure 80. Option 1 is a nested voltage-current controlled solution, while Option 2 is borrowed from publications for connection of HVDC to weak networks and gives rise to a control law which directly expresses the voltage and the HVDC converter terminals.

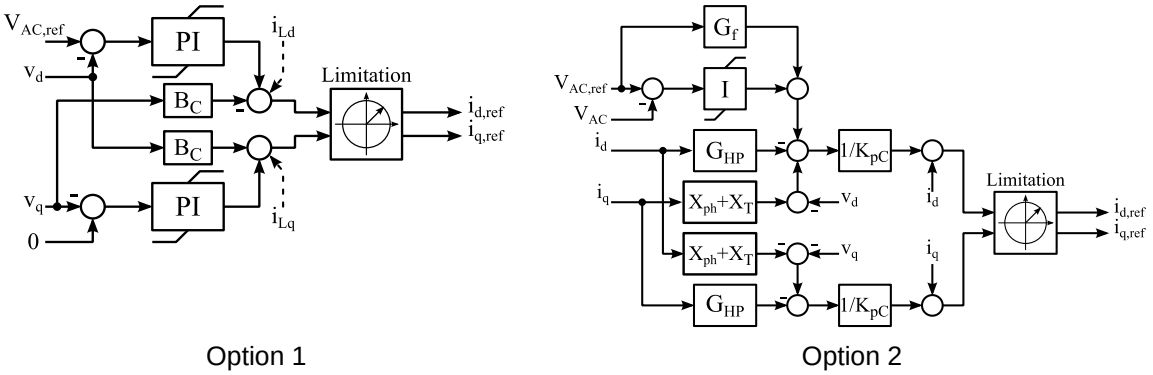

Figure 80 Control candidates for HVDC converter [Zeni, 2015a]

3.2.3 No-load operation and control design

Option 1

The work performed highlighted that the current control (innermost loop) tuning for Option 1 results very hard at no-load, unless a dedicated capacitor is used at the HVDC converter side of the transformer is used, accompanied by a current feed-forward mechanism. Such capacitor would have to be installed on an already large offshore substation and at a voltage level of several hundred kV, making it an expensive solution.

The difficulty of tuning such control loop arises due to the non-ideality of the HVDC converter and its control (delays) and the low-frequency resonance caused by collection network capacitance and converter transformer magnetisation inductance. The undesired shape of the open-loop control transfer function is plotted in black in Figure 81 (T_d = 257 µs) and compared to the ideal case, where the HVDC converter has no delays.

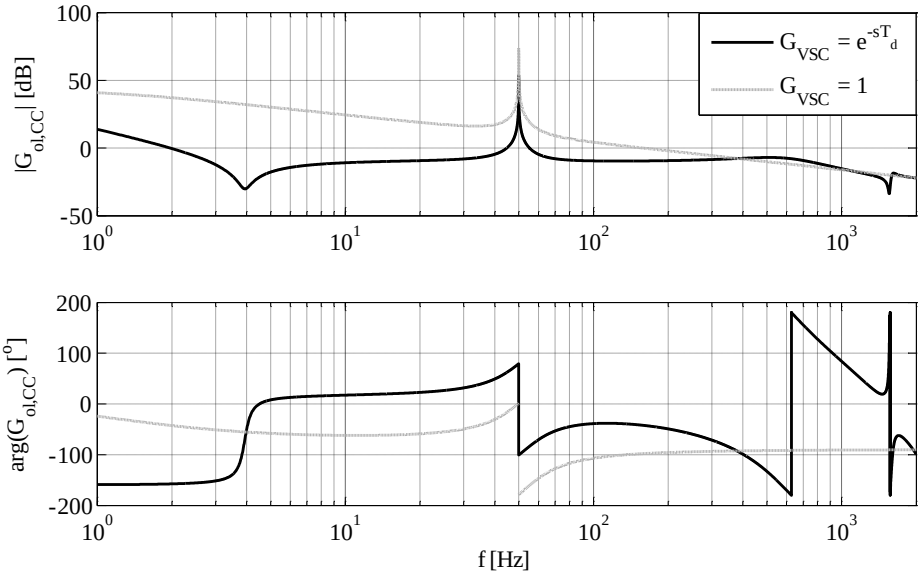

Figure 81 Bode diagram for current control tuning in Option 1 [Zeni, 2015b]

Achieving the same bandwidth as for the ideal case requires significant tuning effort and may actually be impossible without compromising stability. Figure 82 shows a comparison between the ideal case, the real case and the real case with re-design of the controller and clearly shows the issues mentioned in this section. The near-50 Hz oscillations visible for the real cases are the synchronous reference frame mirrored version of the low frequency resonance between collection system and converter transformer. Such oscillation can theoretically even become unstable at negative frequencies as highlighted in [Zeni, 2015a].

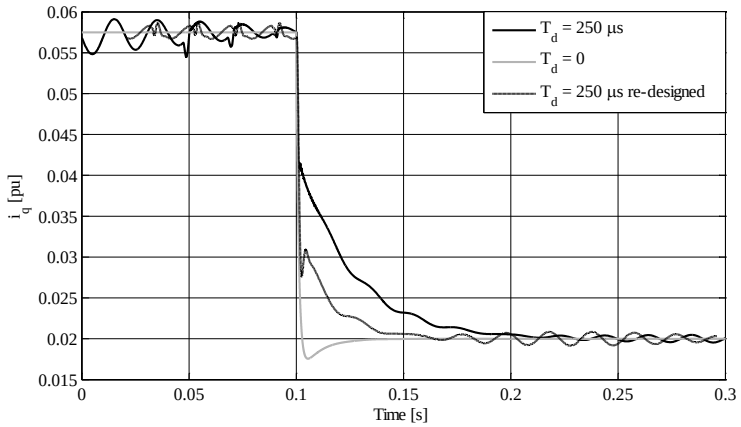

Figure 82 Step response of current controller at no-load [Zeni, 2015b]

Tuning the voltage control (outer control) results easier, assuming that the current control has been tuned properly. However, a dependence of the performance on the connected capacitance appears, unless a dedicated capacitor is used as mentioned above.

Option 2

For Option 2, only the voltage control design is necessary and it was proven in [Zeni, 2015a] and [Zeni, 2015b] that such design is a much easier exercise than for Option 1. The bandwidth can easily be selected by shifting the open-loop transfer function and performance independence of the connected capacitance is guaranteed.

3.2.4 Operation with WPP

The loaded operation with a WPP whose converters are controlled in a standard way (SRF PLL and current controller) was analysed for the two options and led to the following conclusions:

- A major dependence of Option 1's performance on the WPP's active power production. As the active power increases, the system can easily become unstable. Once again, the solution suggested above with dedicated capacitance and feed-forward of load currents is needed to achieve satisfying and robust performance. An alternative is parameter scheduling based on operational point (this is illustrated in Figure 83). On the other hand, Option 2 naturally offers a better independence of the operational point.
- Other than the above, no major differences were noticed between the two schemes.

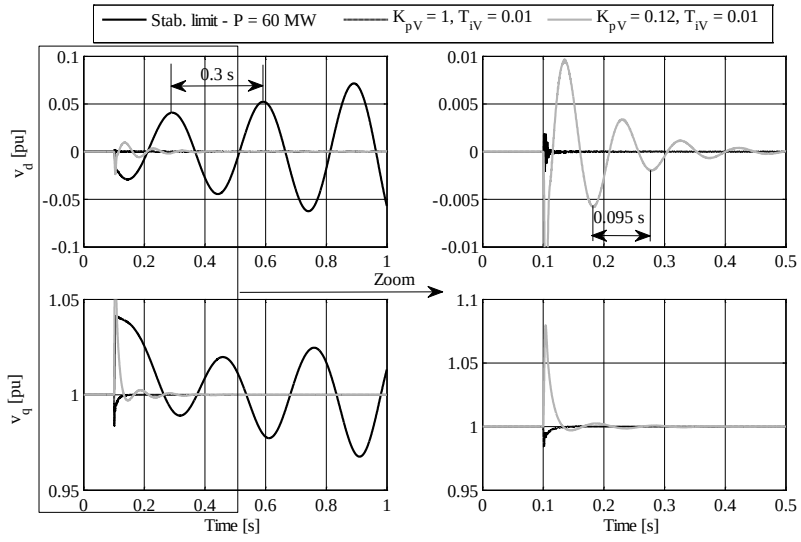

Figure 83 Option 1 time domain performance at limit WPP active power and effect of voltage

3.2.5 Operation with multiple HVDC converters and WPPs

The study has also looked into the operation of offshore AC islanded networks with multiple HVDC converters and WPPs. The need for a coordinated and shared control by the HVDC converters was highlighted, as opposed to a master-slave approach. Results can be found in [Zeni, 2015a].

3.2.6 Summary

Two control candidates for offshore HVDC converters in offshore AC island networks hosting WPPs were analysed (Table 20).

Table 20 Summary of control candidates assessment.

Candidate	Pros	Cons
Option 1 (nested VI control)	Automatic current control capability Slightly better performance in network with multiple HVDC converters and WPPs	Hard tuning at no-load Performance dependence on connected capacitance Performance dependence on active power from WPP Need for dedicated capacitance (space and weight) to solve above two issues
Option 2 (V oriented control)	Straightforward tuning at no-load Simplicity (only one control loop required in normal conditions) Independence of connected capacitance Independence of active power from WPP	No automatic current control capability (need for dedicated protective scheme) Slightly worse performance in networks with multiple HVDC converters and WPPs

The recommendation is that Option 2 should be used. However, a complete assessment requires a more extensive analysis. In particular, short circuit faults and other heavily non-linear events such as energisation and de-energisation must be analysed before a final choice can be made.

4. Feasibility study of offshore grids in the Baltic Sea

The focus in this feasibility study was in the possible offshore grid development paths in the Baltic Sea region. Assuming large amount of offshore wind power in the Baltic Sea, the objective was to find answers to the following questions: Are additional interconnection important? Are multi-terminal offshore grids more beneficial than separate wind power plant cluster connections and interconnectors? What are general power transfers like? Are there significant loop flows in the Nordic countries?

4.1 Scenarios

There are vast wind resources in the Baltic Sea. This study assumed that 27 GW of offshore wind power will be built there. The wind power plant plans taken into account in this study were clustered into 22 wind clusters, which were assumed to operate as nodes in the offshore grid. To connect the offshore grid to the onshore power systems, 17 onshore connection points were selected, mostly from the coastal area. One connection point was selected deeper from the continent because the connection capacity in the coastal area may be insufficient. Figure 84 shows the wind clusters and onshore connection points in the study.

The modelled and simulated system was comprised of the power systems of Denmark, Finland, Norway, Sweden, Estonia, Latvia, Lithuania, Germany and Poland. Some countries were divided into several price regions, whereas other countries were modelled with one price region in each. Figure 85 illustrates the price regions and the grid model in the study. The electricity demand in Germany covered almost half of the total annual electricity demand in the modelled area. Nuclear capacity was assumed to exist in Finland and Sweden but not in other countries. The share of onshore and offshore wind power in the study was approximately 22 % of the annual electricity demand.

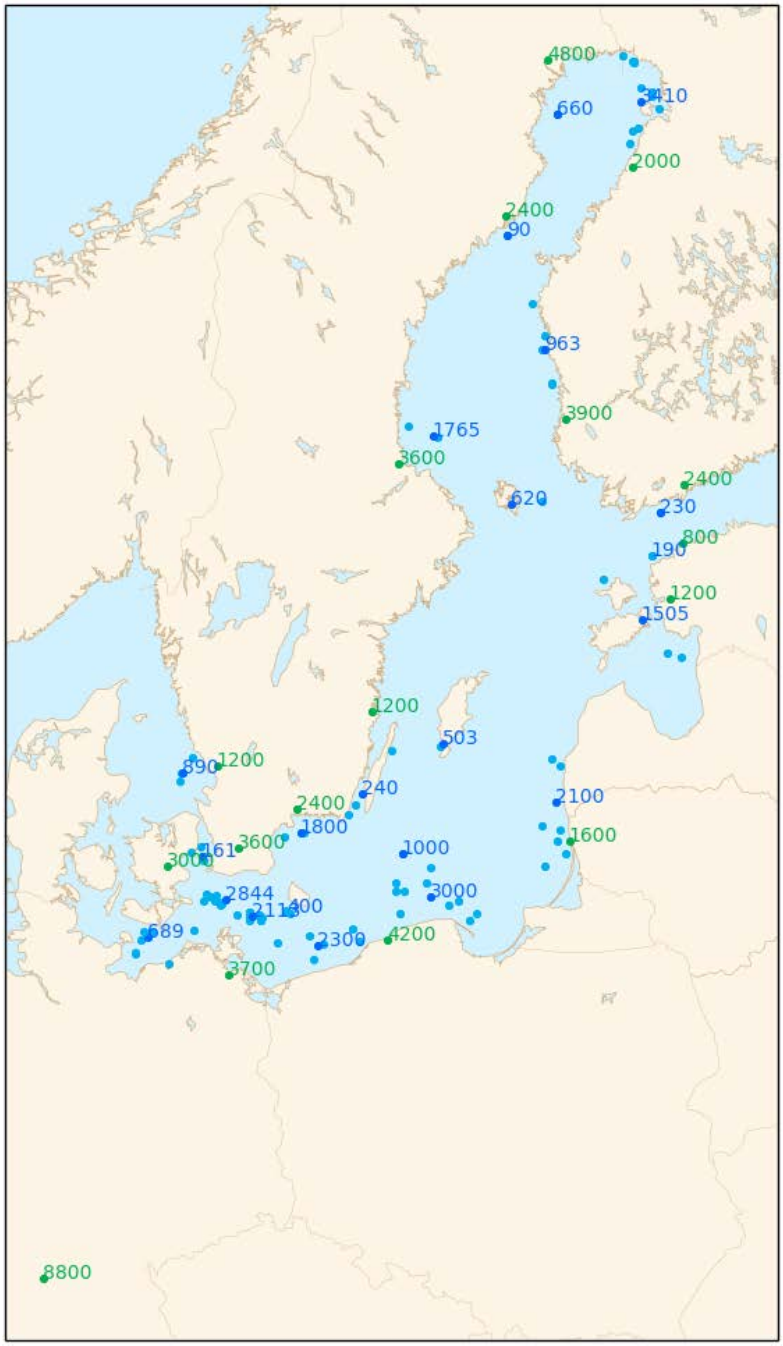

Figure 84 Offshore wind power plants taken into account in the study (light blue), assumed offshore wind clusters including their wind power capacity (dark blue) and onshore connection points including their connection capacity (green).

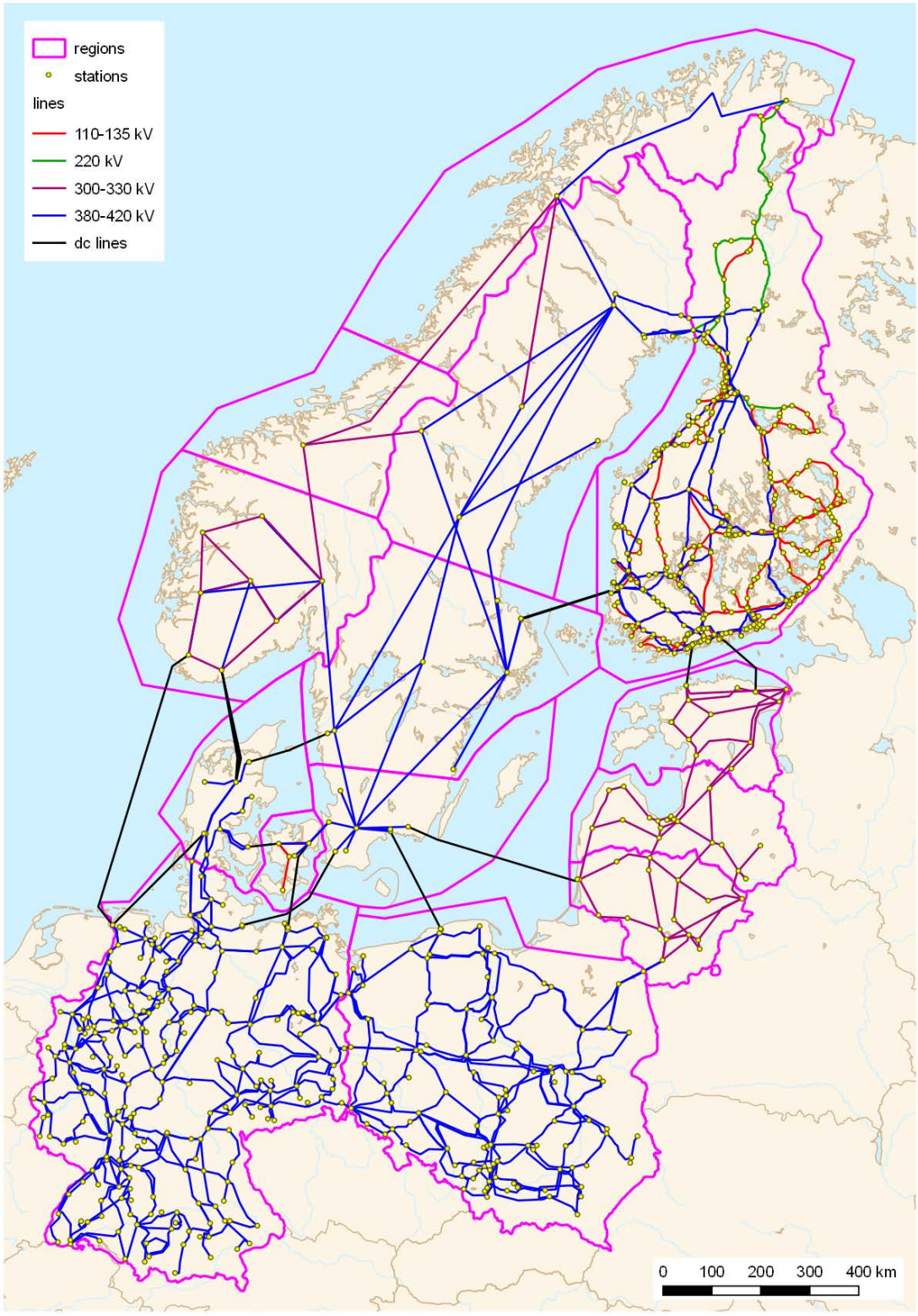

Figure 85 Price regions and grid representation in the modelled system.

The costs of HVDC cables and converter stations were linearized in the study based on data about existing and planned HVDC connections in Europe with capacities between 400 MW and 1400 MW. This means that the economy of scale was not taken into account properly. Table 21 presents the three cost scenarios that were created for the costs: *Low*, *Medium* and *High*. In the *Medium* cost scenario, cables were assumed to cost 1,300 €/MW/km and onshore converter stations were assumed to cost 100,000 €/MW. For offshore converter stations, two assumptions were used: they would be either 50 % or 100 % more expensive than onshore converter stations.

Table 21 HVDC component cost scenarios

Component	Low cost	Medium cost	High cost
Cable/Line (€/MW/km)	1,100	1,300	1,500
Onshore station (€/MW)	70,000	100,000	130,000
Offshore station (50 % [1]) (€/MW)	105,000	150,000	195,000
Offshore station (100 % [1]) (€/MW)	140,000	200,000	260,000

[1] More expensive than onshore station

To downscale the problem of optimizing all possible connections between the 22 wind clusters and 17 onshore connection points and to create differences between the offshore grid scenarios, four topology groups were created: *Limited*, *Onshore*, *Offshore* and *Mix*. Figure 86 illustrates the possible grid investments in each topology group. In *Limited* scenario, only one connection from each wind cluster to shore was allowed. *Onshore* scenario included the same set of possible connection as *Limited*. In addition, it included a few additional offshore-to-shore connections (mainly between Denmark, Sweden and Germany) and interconnections between onshore connection points. *Offshore* scenario included almost the same set of possible connections as *Limited*. As in *Onshore* scenario, it also included a few additional offshore-to-shore connections. However, instead of interconnections between onshore connection points, it was possible to connect wind clusters to each other. *Mix* scenario included a manually defined set of mixed shore-to-shore, offshore-to-shore and offshore-to-offshore connections. *Limited* and *Onshore* scenarios were based on separate wind cluster connections and interconnectors, whereas *Offshore* and *Mix* scenarios utilized also multi-terminal structures.

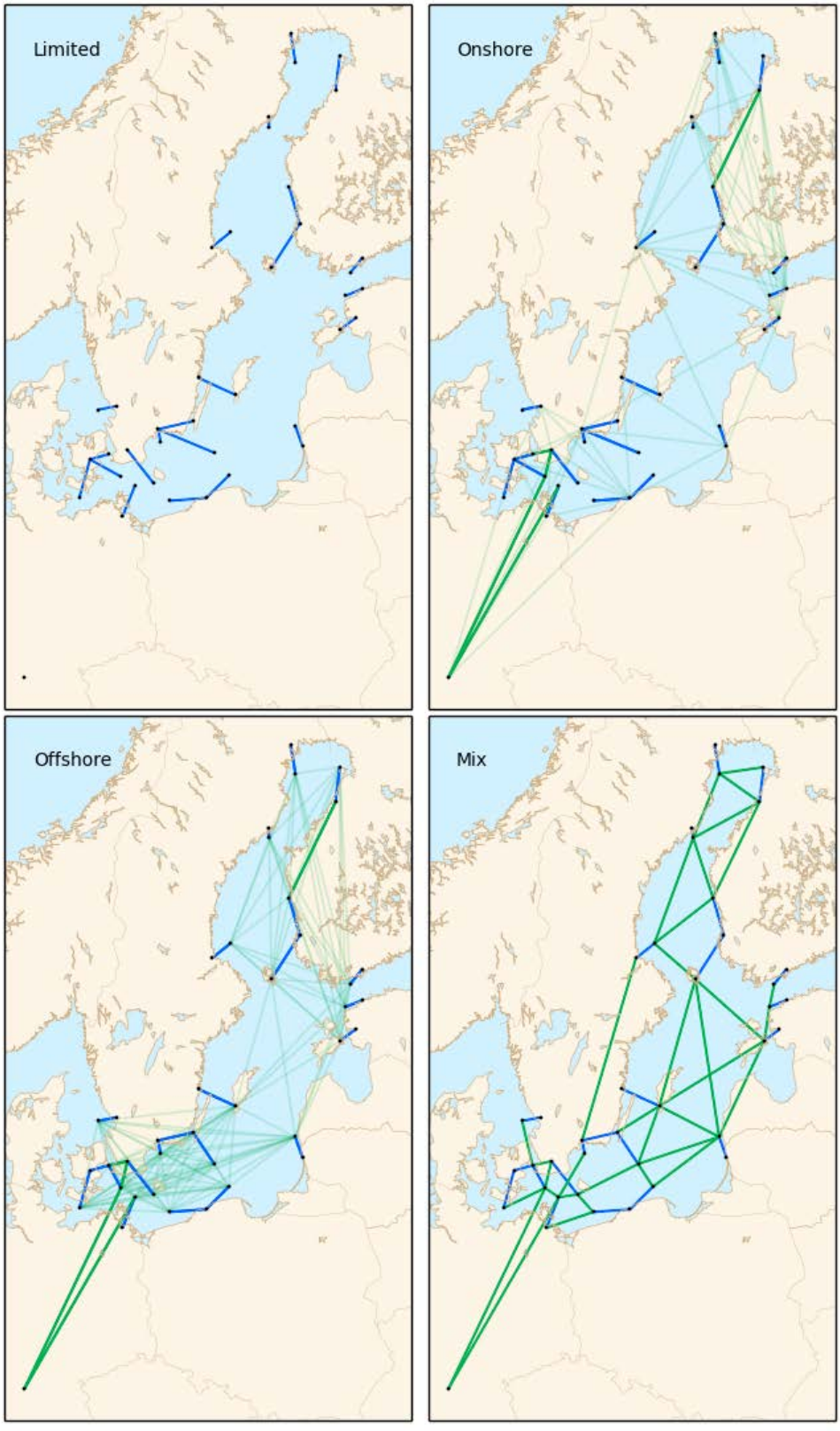

Figure 86 Initial grid investment possibilities in the four offshore HVDC grid topology scenarios. Blue links can have any capacity and green links need to have a capacity over 400 MW.

4.2 Methods

As Figure 87 shows, the methodology in the feasibility study included transmission investment planning, unit commitment and economic dispatch simulation and power flow calculation. First, offshore HVDC grid investments were optimized using an investment optimization model Balmorel. Balmorel optimized the capacities of the possible

transmission links in each topology scenario. Those results were then fed to a unit commitment and economic dispatch model WILMAR JMM, which was used to simulate the market operation in more detail. Both in Balmorel and in WILMAR JMM the transmissions between price regions were modelled using net transfer capacity constraints without modelling the power grid. A few one-hour snapshots from WILMAR JMM were selected for further linearized power flow analysis in PSS®E transmission system analysis tool and a grid model with almost 1000 nodes. Linearized power flow analysis was used instead of the full nonlinear one due to lack of data in some parts of the grid model and also due to lack of knowledge about voltage controlling strategies and good starting values for the iterative solution methods needed for the nonlinear problem.

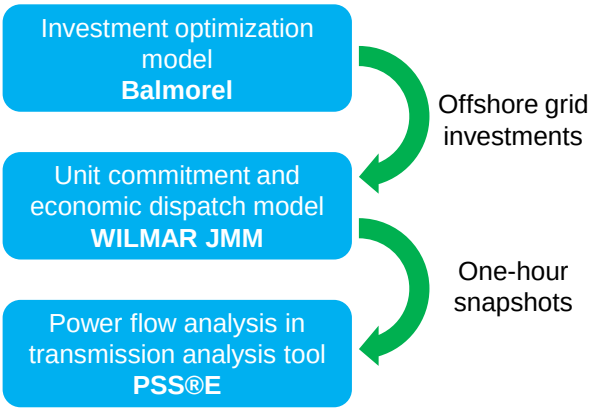

Figure 87 The three-stage methodology in the feasibility study.

4.3 Results

Balmorel showed only few transmission investments in *Limited* scenario, because only few investments were allowed. All other topology scenarios resulted in strong links from the Baltic Sea and southern Sweden to Germany. Links between Sweden, Poland and Germany were also very likely to get invested in. HVDC cost scenario *Low* resulted in more and larger investments than HVDC cost scenario *High*, as expected. The assumption about offshore station costs in comparison to onshore station costs did not seem to have as high impact. Figure 88 shows the grid investment results in *Medium* HVDC cost scenario with the assumption that offshore stations would cost 50 % more than onshore stations. Results from other cost scenarios can be found from [Helistö, 2015].

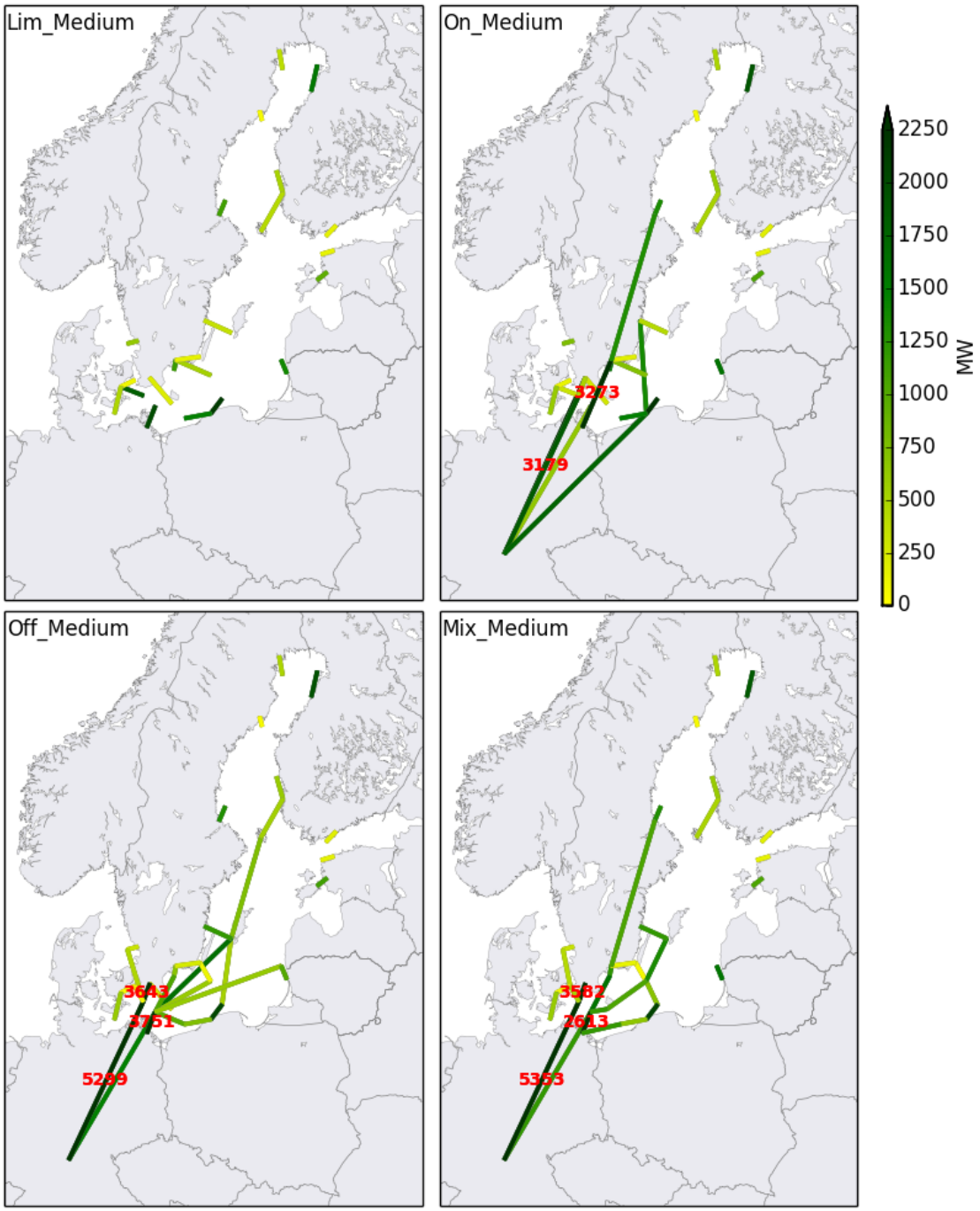

Figure 88 The grid investment results from Balmorel optimization. Values exceeding the scale are shown in the map. (Cost assumptions: HVDC cost scenario Medium, offshore stations 50 % more expensive than onshore stations.)

Figure 89 shows that the annual investment costs in *Limited* scenario were relatively low but the annual operation costs determined by WILMAR JMM were very high compared to other topology scenarios. Thus, *Limited* was clearly the most expensive in total costs. Figure 90 suggests that *Onshore* would be less expensive than *Offshore* topology, which would still be cheaper than the manually defined *Mix* topology. However, these results were achieved with the assumption that HVDC circuit breakers are not available and the multi-terminal structures actually need to be built using two-terminal links. Figure 91 shows that when HVDC circuit breakers and truly multi-terminal structures were taken into account and the cost of HVDC circuit breaker was assumed to be low enough, *Offshore* topology resulted in lower total costs than *Onshore* topology. When the HVDC circuit breaker cost was assumed to be one fourth of converter station costs, the two topologies had about the same total system costs, but when the HVDC circuit breaker cost assumption was decreased to one eighth of converter station costs, *Offshore* topology had already lower costs than *Onshore* topology.

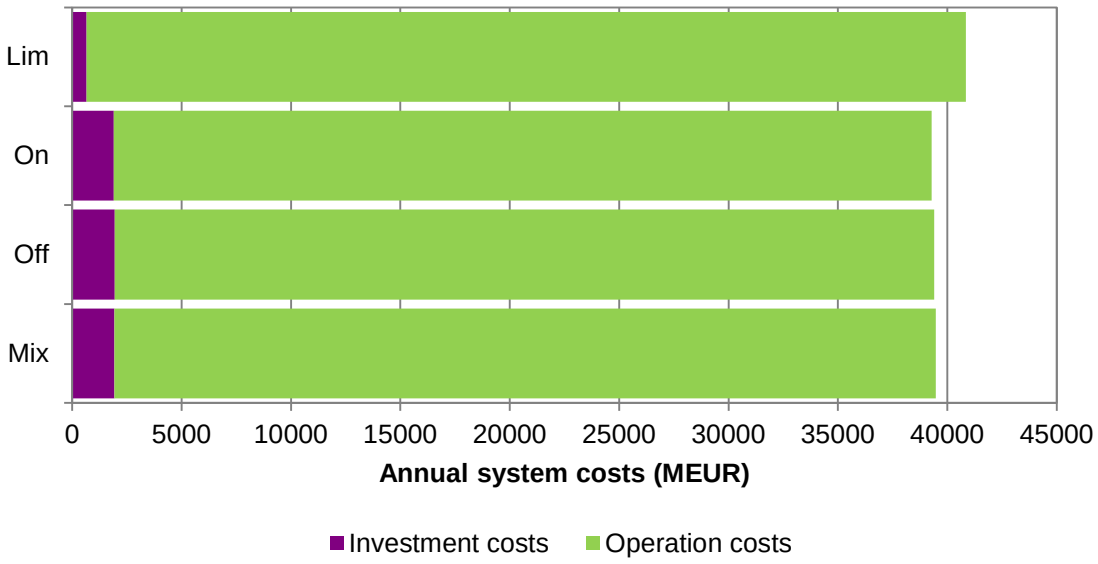

Figure 89 Annual investment costs and operation costs.

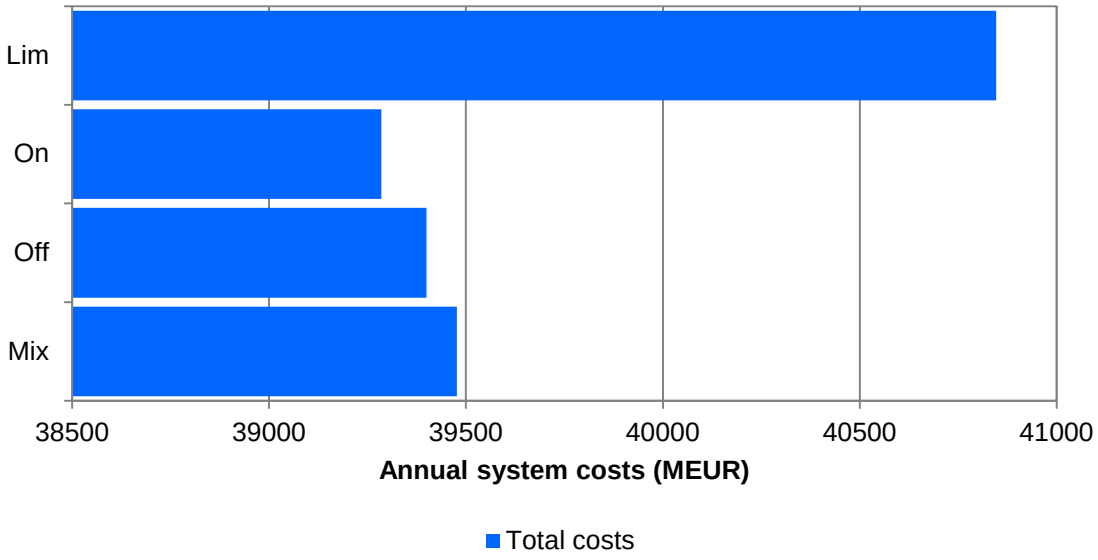

Figure 90 Total annual costs (investment costs + operation costs). Note the starting value of the x-axis.

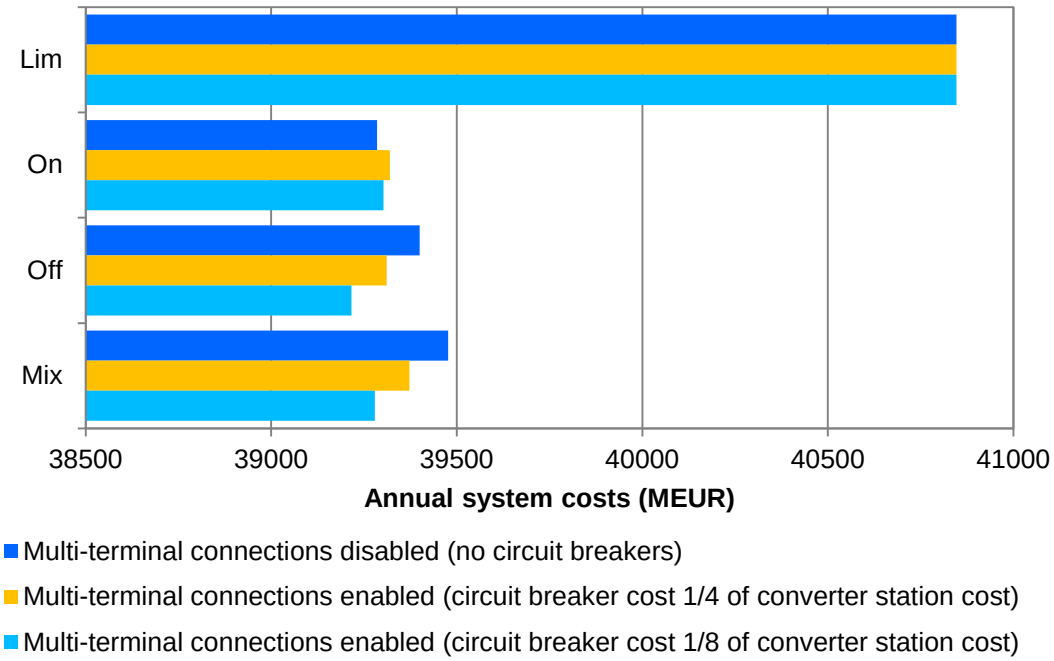

Figure 91 Total annual costs with different assumptions in regard to HVDC circuit breakers and their cost.

As Figure 92 illustrates, the annual electricity transmissions were generally from north to south and from east to west. Germany was importing relatively high amounts of electricity due to the assumed lack of inexpensive generation capacity in Germany. Transmissions from northern Sweden to southern Sweden were higher when further additional connections existed from southern Sweden to Germany. Because of this, the transmissions through Sweden were not as large in *Limited* scenario as in the other scenarios.

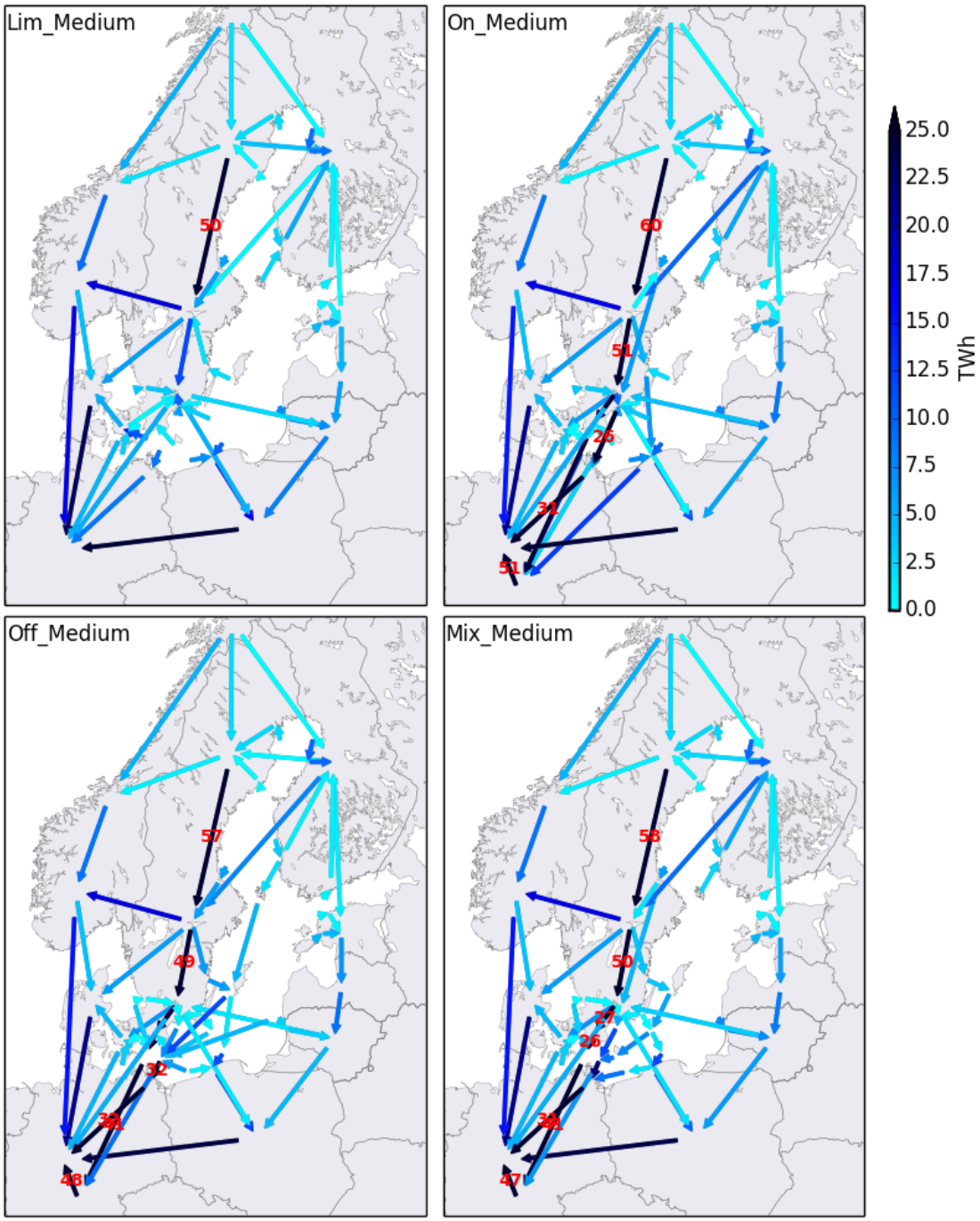

Figure 92 Annual net transmissions between price regions and offshore wind clusters. Values exceeding the scale are shown in the map.

A few WILMAR JMM snapshots were also selected for linearized power flow analysis to check whether the transmissions between price regions change significantly because of loop flows. Table 22 describes the main characteristics of these snapshots.

Table 22 One-hour snapshots selected for power flow studies

	MM-DD-HH	System load (GWh/h)	Offshore wind power available (GWh/h)
Peak load	02-03-10	195	20.3
Minimum load	07-22-04	82	9.0
Peak offshore wind power	10-04-10	155	25.7
Minimum offshore wind power	08-05-08	104	2.5

As Figure 93 illustrates, otherwise no significant loop flows were detected in the snapshots, but inside and between Sweden and Norway the differences between the market transfers and power flow results were quite large. One reason for this is that all other price regions were AC-connected in chain in the grid model and only the price regions in Sweden and Norway were connected through a meshed-like AC-grid. If more countries from Central Europe had been included in the modelling in addition to Germany and Poland, very likely more loop flows would have been detected there as well. The power systems in Sweden and Norway were also modelled with a highly aggregated model compared to other power systems, which may have an influence on the results.

Unscheduled and thus unexpected loop flows increase the risk of overloadings. Figure 94 suggests that according to the linearized power flow analysis with the grid model, some net transfer capacities inside and between Sweden and Norway will be exceeded in the generation and load snapshots determined by WILMAR JMM due to the loop flows which were not possible to capture with WILMAR JMM. This would require redispatch or similar actions, but the impact of these actions was not analysed in this feasibility study.

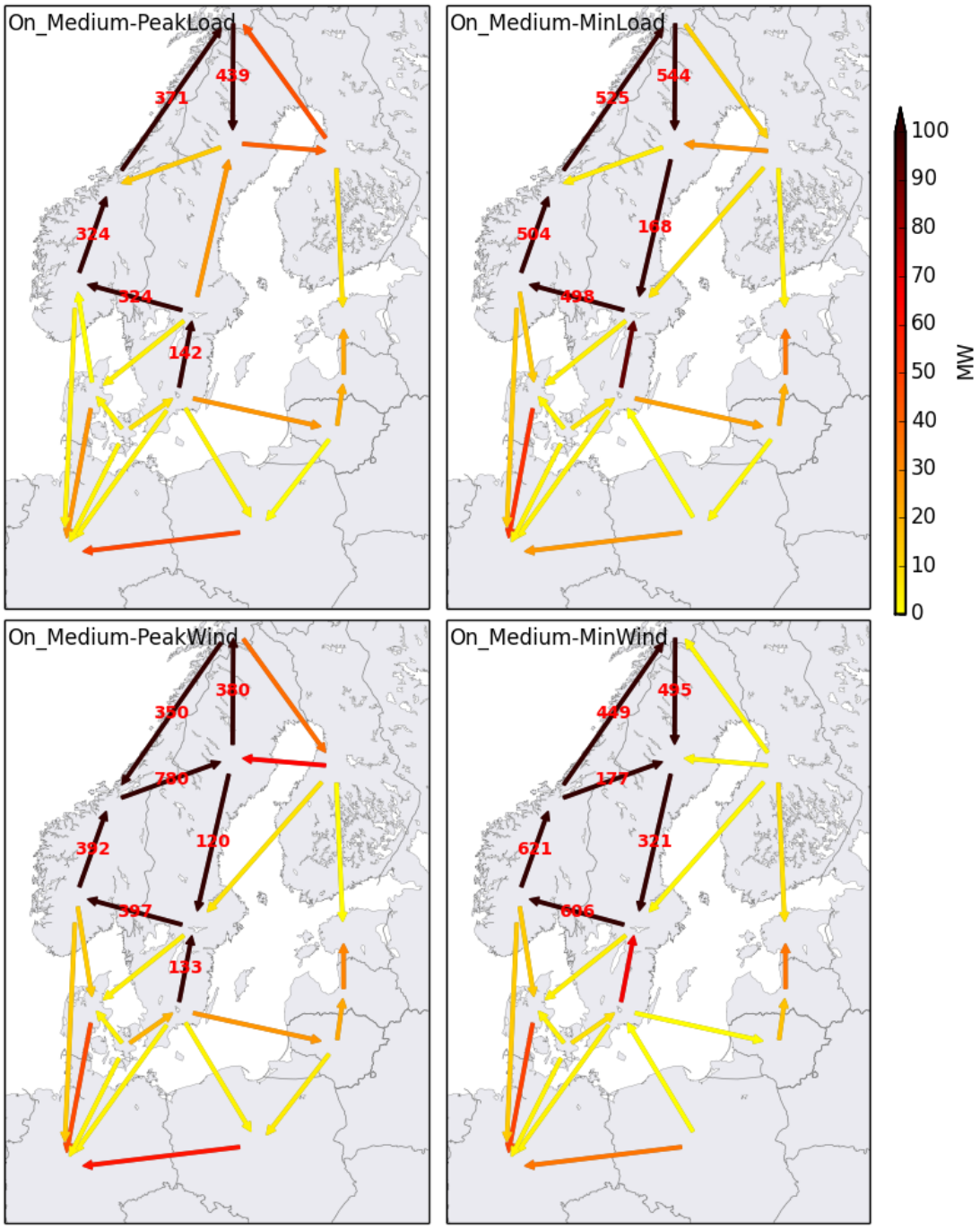

Figure 93 Difference between the transmissions calculated by WILMAR JMM and by linearized power flow equations in four snapshots.

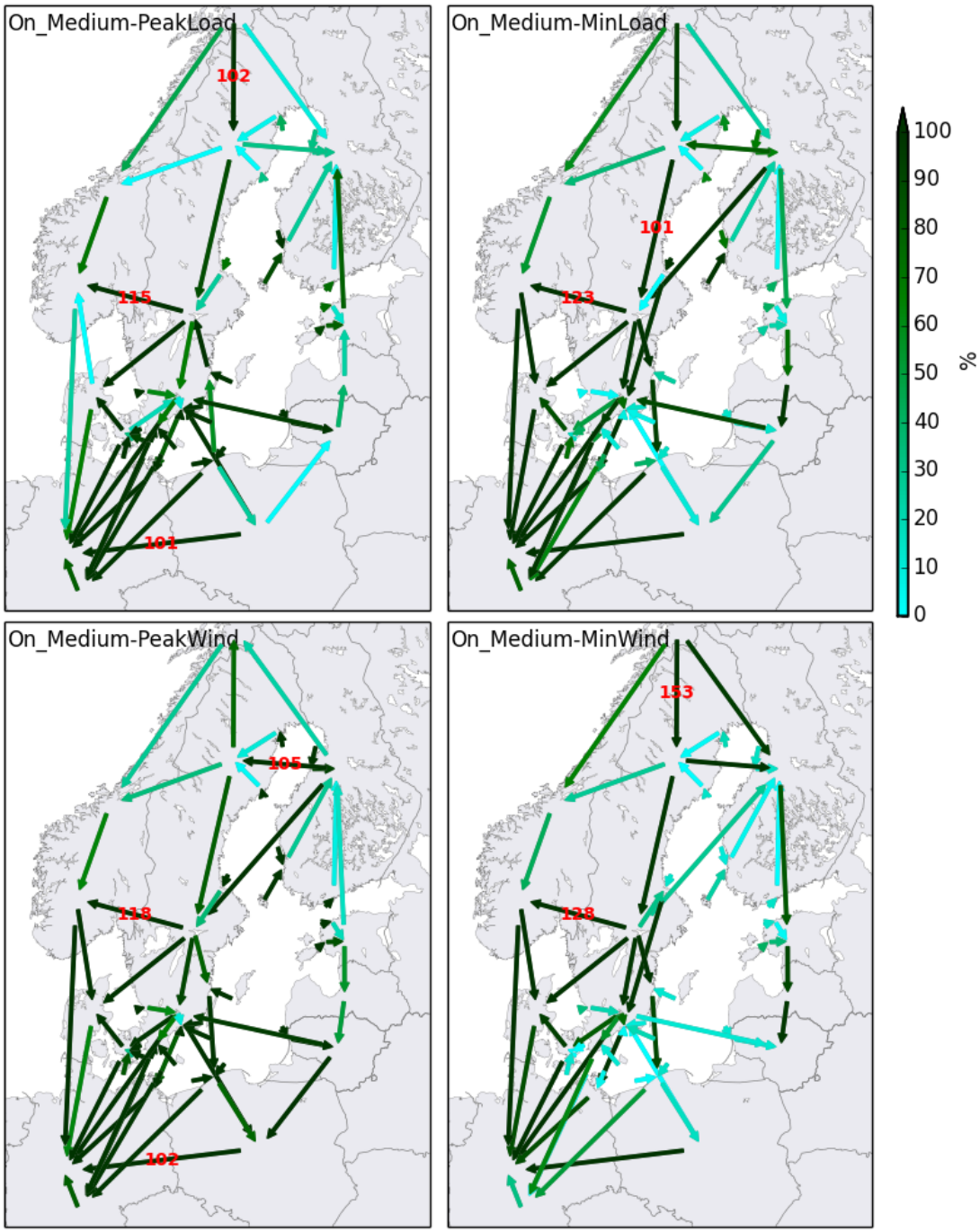

Figure 94 Transmissions calculated by linearized power flow equations compared to net transfer capacities in four snapshots.

N−1 situations or other security-related issues with offshore HVDC grids were not simulated in this study. However, it was concluded that radial structures in general have lower availability compared to meshed structures in N−1 situations. The lack of alternative routes in radial structures can be bypassed to some extent by building large links between two nodes as several smaller links.

4.4 Summary

Costs: The results show that interconnections will decrease the total costs significantly in the Baltic Sea region compared to only two-terminal connections from offshore wind power plant clusters to shore. Building separate offshore interconnectors and wind power plant connections instead of a multi-terminal-like offshore grid based on two-terminal links may result in lower investment and operation costs. According to the results, multi-terminal and meshed offshore grid structures will have lower costs than structures based on separate offshore wind cluster

connections and interconnectors provided that HVDC circuit breakers are available and their price is low enough. The threshold that was found out in the study for the circuit breaker cost is approximately one fourth of converter station cost.

Annual transmissions: In all the studied cases, the annual transmissions were generally from north to south and from east to west. This is a result from the assumed deficit of inexpensive generation infrastructure in Germany. The annual transmissions were also very large from northern Sweden to southern Sweden. However, the initial transmission capacities from northern to central Sweden appear to be large enough since the optimization model did not invest in new connections from the Gulf of Bothnia to central parts of the Baltic Sea in any of the cases.

Hourly transmissions: Hourly power flow analysis results showed similar patterns as the annual transmissions. Loop flows and overloadings were detected inside and between Sweden and Norway in the analysed generation and load snapshots. If the model had included more regions from Central Europe, very likely more loop flows would have been seen there as well.

5. Conclusions

The development of future offshore grids based on VSC-HVDC technology faces many challenges. They cover the whole spectrum, from technical aspects to regulatory/economics. The OffshoreDC project has brought a contribution to the knowledge development that is so stringently needed.

The results briefly presented in this report – with the detailed results in all the published papers, see Appendix – show that, while technically challenging, offshore grids based on VSC-HVDC grids are feasible and have economic benefits.

References

[Barkhordarian, 2001] V. Barkhordarian “IGBT Basics” IXYS Corporation”, IEEE PEDS, Indonesia 2001

[Boonchiam, 2006] P. Boonchiam and N. Mithulananthan, “Diode-clamped multilevel voltage source converter for medium voltage dynamic voltage restorer”, ESD conf, Phuket 2006.

[Budner, 1970]: Alan Budner, "Introduction of Frequency-Dependent Line Parameters into an Electromag-netic Transients Program", IEEE Transactions on Power Apparatus and Systems, Vol. PAS-89, No. 1, January 1970.

[Canay, 1982a]: I. Canay, “A novel approach to the torsional interaction and electrical damping of the synchronous machine part i: Theory,” *IEEE Trans. Power App. Syst.*, vol. PAS-101, no. 10, pp. 3630–3638, Oct. 1982.

[Canay, 1982b]: I. Canay, “A novel approach to the torsional interaction and electrical damping of the synchronous machine part ii: Application to an arbitrary network,” *IEEE Trans. Power App. Syst.*, vol. PAS-101, no. 10, pp. 3639–3647, Oct. 1982.

[Chaudhuri, 2011]: N. R. Chaudhuri, R. Majumder, B. Chaudhuri and P. Jiuping, “Stability Analysis of Vsc Mtdc Grids Connected to Multimachine Ac Systems,” *IEEE Transactions on Power Delivery,* pp. 2774-2784, 2011.

[CIGRE, 1996]: CIGRE Joint Working Group 21/22.01, "Comparison of High Voltage Overhead Lines and Underground Cables”, Report and Guidelines", 1996.

[Duncan, 2010] Duncan A. Grant, John Gowar, “Power mosfets Application and theory”, Wiley p. 41-60, New York 2010.

[Endegnanew, 2015]: A. G. Endegnanew, J. Beerten and K. Uhlen, “Dynamic Interactions between Asynchronous Grids Interconnected through an Mtdc System,” in *Cigré Symposium*, Lund, 2015.

[Gustavsen, 1999] B. Gustavsen, G. Irwin, R. Mangelrod, D. Brandt, and K. Kent, “Transmission line models for the simulation of interaction phenomena between parallel ac and dc overhead lines,” Int. Conf. on Power Sys, 20-24, Jun. 1999.

[Harnefors, 2008]: L. Harnefors, L. Zhang and M. Bongiorno, “Frequency-domain passivity-based current controller design,” *Power Electronics, IET*, vol. 1, no. 4, pp. 455–465, Dec. 2008.

[Harnefors, 2011]: L. Harnefors, “Proof and application of the positive-net-damping stability criterion,” *IEEE Trans. Power Syst.*, vol. 26, no. 1, pp. 481–482, Feb. 2011.

[Harnefors, 2007a]: L. Harnefors, “Analysis of subsynchronous torsional interaction with power electronic converters,” *IEEE Trans. Power Syst.*, vol. 22, no. 1, pp. 305–313, Feb. 2007.

[Harnefors, 2007b]: L. Harnefors,M. Bongiorno and S. Lundberg, “Input-admittance calculation and shaping for controlled voltage-source converters,” *IEEE Trans. Ind. Electron.*, vol. 54, no. 6, pp. 3323–3334, Dec. 2007.

[Helistö, 2015]: N. Helistö and V. C. Tai, “OffshoreDC: Electricity market and power flow impact of wind power and DC grids in the Baltic Sea,” Research report VTT-R-05999-15, Espoo, Finland, 2015.

[Kalcon, 2012]: G. O. Kalcon, G. P. Adam, O. Anaya-Lara, S. Lo and K. Uhlen, “Small-Signal Stability Analysis of Multi-Terminal Vsc-Based Dc Transmission Systems,” *IEEE Transactions on Power Systems,* pp. 1818-1830, 2012.

[Kundur, 1994]: P. Kundur, Power System Stability and Control, New York: McGraw-Hill, 1994.

[Mura, 2010]: F. Mura, C. Meyer and R. D. Doncker, “Stability analysis of high-power dc grids,” *IEEE Trans. Ind. Appl.*, vol. 46, no. 2, pp. 584–592, March 2010.

[Pinares, 2014]: G. Pinares, “On the analysis of dc network dynamics of vsc-based hvdc systems,” Chalmers University of Technology, Gothenburg, Sweden, Licentiate Thesis, Apr. 2014.

[PSCAD] PSCAD/EMTDC online help, version 4.2.1, Manitoba, Canada.

[Rault, 2012]: P. Rault, F. Colas, X. Guillaud and S. Nguefeu, “Method for small signal stability analysis of vsc-mtdc grids,” in *Proc. of IEEE Power and Energy Society General Meeting*, July 2012, pp. 1–7.

[Rault, 2012]: P. Rault, F. Colas, X. Guillaud and S. Nguefu, “Method for Small Signal Stability Ananlysis of Vsc-Mtdc Grids,” in *IEEE Power and Energy Society General Meeting*, San Diego, 2012.

[Rault, 2013]: P. Rault, F. Guillaud, F. Colas and S. Nguefu, “Investigation on Interactions between Ac and Dc Grids,” in *IEEE PowerTech*, Grenoble, 2013.

[Silva, 2010]: H. M. J. De Silva, A. M. Gole, J. E. Nordstrom, L. M. Wedepohl, "Robust Passivity En-forcement Scheme for Time-Domain Simulation of Multi-Conductor Transmission Lines and Cables", IEEE Transactions on Power Delivery, Vol. 25, Issue 2, April 2010.

[Støylen, 2014]: H. Støylen, “Laboratory Demonstration of Provision of Primary Frequency Control Services from Vsc-Hvdc Connected Wind Farms,” Norwegian University of Science and Technology, Trondheim, Master Thesis, 2014.

[Støylen, 2015]: H. Støylen and K. Uhlen, “Laboratory Demonstration of Inertial Response from Vsc-Hvdc Connected Wind Farms,” in *11th Internation Conference on AC and DC Power Transmission*, Birmingham, 2015.

[Tabesh, 2005]: A. Tabesh and R. Iravani, “On the application of the complex torque coefficients method to the analysis of torsional dynamics,” *IEEE Trans. Energy Convers.*, vol. 20, no. 2, pp. 268–275, June 2005.

[Willems, 1972]: J. Willems, “Dissipative dynamical systems part i: General theory,” *Arch. Ration. Mech. Anal.*, vol. 45, no. 5, pp. 321–351, 1972.

[Zadeh, 2014]: M. K. Zadeh, M. Amin, J. A. Suul, M. Molinas and O. B. Fosso, “Small-Signal Stability Study of the Cigre Dc Grid Test System with Analysis of Participation Factors and Parameter Sensitivity of Oscillation Modes,” in *Power Systems Computation Conference*, Wroclaw, 2014.

[Zeni, 2012]: L. Zeni, I. Margaris, A. Hansen, P. Sørensen and P. Kjær, “Generic Models of Wind Turbine Generators for Advanced Applications in a VSC-based Offshore HVDC Network,” in *The 10th IET Conference on AC/DC Transmission*, Birmingham, 2012.

[Zeni, 2013]: L. Zeni, H. Jóhannsson, A. D. Hansen, P. E. Sørensen, B. Hesselbæk and P. C. Kjær, “Influence of Current Limitation on Voltage Stability with Voltage Sourced Converter HVDC,” in *ISGT Conference Europe*, Copenhagen, 2013.

[Zeni, 2014]: L. Zeni, T. Lund, A. Hansen, P. Sørensen, P. Kjær, B. Hesselbæk and J. Glasdam, “Coordinated system services from offshore wind power plants connected through HVDC networks,” in *Cigré session*, Paris, 2014.

[Zeni, 2015a]: L. Zeni, “Power System Integration of VSC-HVDC connected Wind Power Plants,” Ph.D. thesis, Technical University of Denmark, Roskilde, 2015.

[Zeni, 2015b]: L. Zeni, B. Hesselbæk, P. E. Sørensen, A. D. Hansen and P. C. Kjær, “Control of VSC-HVDC in offshore AC islands with wind power plants: comparison of two alternatives,” in *PowerTech 2015*, Eindhoven, 2015.

[Zeni, 2016a]: L. Zeni, S. Goumalatsos, R. Eriksson, M. Altin, P. Sørensen, A. Hansen, P. Kjær and B. Hesselbæk, “Power Oscillation Damping from VSC-HVDC connected Offshore Wind Power Plants,” *IEEE Transactions on Power Delivery,* 2016.

[Zeni, 2016b]: L. Zeni, V. Gevorgian, R. Wallen, J. Bech, P. E. Sørensen and B. Hesselbæk, “Utilisation of Real-Scale Renewable Energy Test Facility for Validation of Generic Wind Turbine and Wind Power Plant Controller Models,” *Accepted for publication on IET Renewable Power Generation,* 2016.

[Zhang, 2007]: L. Zhang, L. Harnefors and H.-P. Nee, “Interconnection of two very weak ac systems by vsc-hvdc links using power-synchronization control,” *IEEE Trans. Power Syst.*, vol. 26, no. 1, pp. 344–355, Feb. 2007.

Appendix A Publications from OffshoreDC project

Journals:

G. Stamatiou and M. Bongiorno, "Stability Analysis of Two-Terminal VSC-HVDC Systems Using the Net-Damping Criterion," in IEEE Trans. Power Del., vol. 31, no. 4, pp. 1748-1756, Aug. 2016.

L. Zeni, S. Goumalatsos, R. Eriksson, M. Altin, P. Sørensen, A. Hansen, P. Kjær and B. Hesselbæk, “Power Oscillation Damping from VSC-HVDC connected Offshore Wind Power Plants,” IEEE Transactions on Power Delivery, 2016.

L. Zeni, V. Gevorgian, R. Wallen, J. Bech, P. E. Sørensen and B. Hesselbæk, “Utilisation of Real-Scale Renewable Energy Test Facility for Validation of Generic Wind Turbine and Wind Power Plant Controller Models,” IET Renewable Power Generation, 2016.

V. C. Tai, K. Uhlen, “Design and Optimisation of Offshore Grids in Baltic Sea for Scenario Year 2030”. Energy Procedia, Volume 53, Pages 124 - 134.

Conferences:

A.G. Endegnanew, J. Beerten, and K. Uhlen, "Dynamic Interactions between Asynchronous Grids Interconnected through an MTDC System" in Cigré symposium Across borders HVDC systems and market integration, Lund, Sweden, 2015.

A.G. Laukhamar, L. Zeni, and P.E. Sørensen. “Alternatives for Primary Frequency Control Contribution from Wind Power Plants Connected to VSC-HVDC Intertie”. In European Wind Energy Conference, March 2014.

G. Stamatiou and M. Bongiorno. “A novel decentralized control strategy for MultiTerminal HVDC transmission grids”, IEEE Energy Conversion Congress and Exposition, ECCE 2015, Montreal, Canada, September 2015.

G. Stamatiou and M. Bongiorno. “Investigation of poorly-damped conditions in VSC-HVDC systems”, 14th International Workshop on Large-Scale Integration of Wind Power into Power Systems as well as on Transmission Networks for Offshore Wind Power Plants, Brussels, Belgium, October 2015.

G. Stamatiou, M. Bongiorno - Decentralized Converter Controller for Multi-terminal HVDC Grids, EPE'13 ECCE Europe, 15th European Conference on Power Electronics and Applications, 3-5 September 2013, Lille, France

J. Glasdam, L. Zeni, J. Hjerrild, L. Kocewiak, B. Hesselbæk, P.E. Sørensen, A.D. Hansen, C.L. Bak, P.C. Kjær “An Assessment of Converter Modelling Needs for Offshore Wind Power Plants Connected via VSC-HVDC Networks” , 12th Wind Integration Workshop, London, October 2013.

J. Glasdam, L. Zeni, M. Gryning, J. Hjerllid, L. Kocewiak, B. Hesselbæk, K. Andersen, T. Sørensen, M. Blanke, P.E. Sørensen, A.D. Hansen, C.L. Bak, P.C. Kjær “HVDC Connected Offshore Wind Power Plants: Review and Outlook of Current Research”, 12th Wind Integration Workshop, London, October 2013.

J. Glasdam, L.H. Kocewiak, J. Hjerrild, C.L. Bak, and L. Zeni. “Comparison of Field Measurements and EMT Simulation Results on a Multi-Level STATCOM for Grid Integration of London Array Wind Power Plant”. In 45th Cigré session, August 2014.

L. Zeni, B. Hesselbæk, P.E. Sørensen, A.D. Hansen, C. Kjær, Philip, “Control of VSC-HVDC in offshore AC islands with wind power plants: Comparison of two alternatives”, Proceedings of 2015 IEEE PowerTech. IEEE, 2015

L. Zeni, H. Jóhanssonn, A.D. Hansen, P.E. Sørensen, B. Hesselbæk, P.C. Kjær “Influence of Current Limitation on Voltage Stability with Voltage Sourced Converter HVDC”, IEEE ISGT Conference Europe 2013, Lyngby, Denmark, October 2013.

L. Zeni, I. Margaris, A. D. Hansen, P. Sørensen, P. C. Kjær, ”Generic Models of Wind Turbine Generators for Advanced Applications in a VSC-based Offshore HVDC Network”. IET ACDC Conference 2012, Birmingham, December 2012.

L. Zeni, T. Haileselassie, G. Stamatiou, A. G. Eriksen, J. Holbøll, O. Carlsson, K. Uhlen, P. Sørensen, N. A. Cutululis, “DC grids for integration of large scale wind power ”. In EWEA Offshore 2011, Amsterdam, December 2011.

L. Zeni, T. Lund, B. Hesselbæk, P.E. Sørensen, A.D. Hansen, and P.C. Kjær. ”Coordinated system services from offshore wind power plants connected through HVDC networks”. In 45th Cigré session, August 2014.

M. Sztykiel, R. da Silva, R. Teodorescu, L. Zeni, L. Helle, P. C. Kjær, “Modular Multilevel Converter Modelling Control and Analysis under Grid Frequency Deviations”. In EPE Joint Wind and T&D Seminar 2012, Aalborg, June 2012.

N. Helistö, S. Uski, ”Electricity Market and Power Flow Impact of Offshore Grids in the Baltic Sea Region”. 14th International Workshop on Large-Scale Integration of Wind Power into Power Systems as well as on Transmission Networks for Offshore Wind Power Plants, Brussels, October 2015.

N. Helistö, S. Uski-Joutsenvuo, ”Initializing Network Simulations for Case Studies of Offshore Wind Power and Offshore DC Grid Integration in the Power System of Northern Europe”. 12th International Workshop on Large-Scale Integration of Wind Power into Power Systems as well as on Transmission Networks for Offshore Wind Power Plants, London, October 2013.

N.A. Cutululis, L. Zeni, W.Z. El-Khatib, J, Holbøll, P.E. Sørensen, G. Stamatiou, O. Carlson, V.C. Tai, K. Uhlen, J. Kiviluoma, T., Lund, “Challenges Towards the Deployment of Offshore Grids: the OffshoreDC Project”. Proceedings of 13th International Workshop on Large-Scale Integration of Wind Power into Power Systems as well as on Transmission Networks for Offshore Wind Power (WIW 2014). Energynautics GmbH, 2014.

R. Ghiga, Q. Wu, K. Martin, W.Z. El-Khatib, L. Cheng A.H. Nielsen, “Dynamic PMU Compliance Test under C37.118.1aTM-2014”. Proceedings of 2015 IEEE PES General Meeting. IEEE, 2015.

R. Teodorescu, E.P. Eni, L. Mathe, P. Rodríguez, “Modular Multilevel Converter Control Strategy with Fault Tolerance”, Proceedings of ICREPQ 2013.

S. Vogel, T.W. Rasmussen, W.Z. El-Khatib, J. Holbøll, “DC Collection Network Simulation for Offshore Wind Farms”. Poster session presented at EWEA Offshore 2015 Conference, Copenhagen, Denmark.

T. K. Vrana, L. Zeni, O. B. Fosso, “Active Power Control with Undead-Band Voltage & Frequency Droop for HVDC Converters in Large Meshed DC Grids”. In European Wind Energy Conference 2012, Copenhagen, April 2012.

T. K. Vrana, L. Zeni, O. B. Fosso, “Active Power Control with Undead-Band Voltage & Frequency Droop Applied to a Meshed DC Grid Test System”. In EnergyCon 2012, Firenze, September 2012.

T. K. Vrana, L. Zeni, O. B. Fosso, “Dynamic Active Power Control with Improved Undead-Band Droop for HVDC Grids”. IET ACDC Conference 2012, Birmingham, December 2012.

T.K. Vrana, H.G. Svendsen, A.G. Endegnanew, ”Wind Power Grid Codes: Historic Development, Present State and Future Outlook”. 14th Wind Integration Workshop 14th Workshop on Large-Scale Integration of Wind Power into Power Systems as well as on Transmission Networks for Offshore Wind Power Plants.

T.M. Haileselassie, A.G. Endegnanew, K. Uhlen, ”Secondary control in multi-terminal VSC-HVDC transmission system”. Power & Energy Society General Meeting, 2015 IEEE.

W. Z. El-Khatib, J. Hollboel, T. W. Rasmussen, “Capacitor performance limitation in in high power converter application” The 23th Nordic insulation symposium (NORD-IS), June 2013, Trondheim, Norway.

W. Z. El-Khatib, J. Hollboel, T. W. Rasmussen, “Efficient modelling of a modular multilevel converter High frequent” 48th international universities power engineering conference (IUPEC), September 2013, Dublin, Ireland.

W. Z. El-Khatib, J. Hollboel, T. W. Rasmussen, “High frequent modelling of a modular multilevel converter using passive component” International conference on power systems transients (IPST), July 2013, Vancouver, Canada.

W.Z. El-Khatib, D. Schwartzberg, I. Arana Aristi, J. Holbøll, L. Zeni, “Transients in VSC-HVDC connected offshore wind power plant”. 11th IET International Conference on AC and DC Power Transmission. IEEE, 2015

Deliverables/Thesis:

N. Sisu, K. Juha, S. Uski-Joutsenvuo, Survey of plans for the development of offshore wind power in the Nordic region, D1, OffshoreDC project, October 2012. Online http://www.offshoredc.dtu.dk/-/media/Sites/OffshoreDC/Publications/D1-Survey-of-plans-for-development-of-offshore-wind-powerin-the-Nordic-region.ashx?la=da

V. C. Tai, K. Uhlen, J. Kiviluoma, Offshore Grid Design and Market Impact – Preliminary Results, D2, OffshoreDC project, November 2013. Online http://www.offshoredc.dtu.dk/-/media/Sites/OffshoreDC/Publications/D2-ToolForOptimalDesignOffshoreGrids.ashx?la=da

N. Helistö, V. C. Tai, “OffshoreDC: Electricity market and power flow impact of wind power and DC grids in the Baltic Sea,” Research report VTT-R-05999-15, Espoo, Finland, 2015. Online http://www.vtt.fi/inf/julkaisut/muut/2015/VTT-R-05999-15.pdf

L. Zeni, “Power system integration of VSC-HVDC connected offshore wind power plants”; DTU Wind Energy, 2015. 242 p. (DTU Wind Energy PhD; No. 0053(EN)). Online http://orbit.dtu.dk/files/116284450/Power_system_integration.pdf

S. Georgios, “Converter interactions in VSC-based HVDC systems”, Licentiate thesis, Chalmers University, 2015. Online http://publications.lib.chalmers.se/records/fulltext/217445/217445.pdf

DTU Wind Energy is a department of the Technical University of Denmark with a unique integration of research, education, innovation and public/private sector consulting in the field of wind energy. Our activities develop new opportunities and technology for the global and Danish exploitation of wind energy. Research focuses on key technical-scientific fields, which are central for the development, innovation and use of wind energy and provides the basis for advanced education at the education.

We have more than 240 staff members of which approximately 60 are PhD students. Research is conducted within nine research programmes organized into three main topics: Wind energy systems, Wind turbine technology and Basics for wind energy.

Technical University of Denmark
Department of Wind Energy
Frederiksborgvej 399
Building 118
4000 Roskilde
Denmark
Telephone 46 77 50 85

info@vindenergi.dtu.dk
www.vindenergi.dtu.dk